Excitons in Semiconductor Quantum Wells Studied Using Two-Dimensional Coherent Spectroscopy

by

Rohan Singh

B.Sc., Indian Institute of Technology Kharagpur, 2010

M.Sc., Indian Institute of Technology Kharagpur, 2010

M.Sc., University of Colorado Boulder, 2013

A thesis submitted to the

Faculty of the Graduate School of the

University of Colorado in partial fulfillment

of the requirements for the degree of

Doctor of Philosophy

Department of Physics

2015

This thesis entitled:
Excitons in Semiconductor Quantum Wells Studied Using Two-Dimensional Coherent Spectroscopy
written by Rohan Singh
has been approved for the Department of Physics

_____

Steven T. Cundiff

_____

Markus B. Raschke

Date _____

The final copy of this thesis has been examined by the signatories, and we find that both the content and the form meet acceptable presentation standards of scholarly work in the above mentioned discipline.

Singh, Rohan (Ph.D., Physics)

Excitons in Semiconductor Quantum Wells Studied Using Two-Dimensional Coherent Spectroscopy

Thesis directed by Prof. Steven T. Cundiff

Correlated electron-hole pairs, or excitons, in semiconductor nanostructures have been studied extensively over the past few decades. The optical response of excitons is complicated due to inhomogeneous broadening, presence of multiple states, and exciton-exciton interactions. In this work we bring new perspectives to exciton physics in semiconductor quantum wells (QWs) through two-dimensional coherent spectroscopy (2DCS).

The effect of QW growth direction on the optical properties of excitons is explored by studying (110)-oriented GaAs QWs. The homogeneous and inhomogeneous linewidths of the heavy-hole exciton resonance are measured. By probing the optical nonlinear response for polarization along the in-plane crystal axes $[1\bar{1}0]$ and [001], we measure different homogeneous linewidths for the two orthogonal directions. This difference is found to be due to anisotropic excitation-induced dephasing, caused by a crystal-axis-dependent absorption coefficient. The extrapolated zero-excitation density homogeneous linewidth exhibits an activation-like temperature dependence.

Spectral diffusion of excitons in (001)-oriented QWs has been studied. We show that the spectral diffusion characteristics depend strongly on the sample temperature. Spectral diffusion is generally assumed to follow the strong-redistribution approximation, partly because of lack of any evidence to the contrary. We find that this assumption is violated at low sample temperatures for excitons in QWs; high-energy excitons preferentially relax due to a negligible phonon population at low temperatures. The frequency-frequency correlation function is measured through a numerical fitting procedure to quantify spectral diffusion for sample temperatures > 20 K.

Exciton-exciton interactions affect the light-matter interactions in QWs significantly. We present an intuitive and simple model for these interactions by treating excitons as interacting bosons. We show that the polarization-dependent exciton dephasing rate in GaAs quantum wells is due to the bosonic character of excitons. We fit slices from simulated spectra to those from the experimentally measured spectra and show that interference between two different quantum mechanical pathways results in a slower dephasing rate for co-circular and co-linear polarization of optical excitation pulses. This interference does not exist for cross-linearly polarized excitation pulses resulting in a faster dephasing rate. Additionally, we were able to separately quantify inter- and intra-mode interactions between excitons through exciton-density-dependent measurements.

Dedication

This thesis is dedicated to my parents.

Acknowledgements

First and foremost I would like to thank Steve Cundiff for giving me the opportunity to work under his guidance. He has been an excellent advisor and a constant source of inspiration.

I would also like to thank all the members of the Cundiff lab for being excellent labmates and making my life as a graduate student a lot of fun. I have learned a lot through stimulating interactions with all of them. The members of the 2D team – Galan Moody, Hebin Li, Takeshi Suzuki, Bo Sun, Gaël Nardin, Travis Autry, Bachana Lomsadze, Chris Smallwood, and Diogo Almeida have been especially helpful. Soobong Choi, Andy Funk, and Martina Carsjens, along with Galan and Hebin, helped me immensely with the SEA TADPOLE project. I am also grateful to have the opportunity to interact with and learn from Eric Martin, Andy Almand-Hunter, Marc Aβmann, George Roumpos, Kai Wang, Matt Day, Nick Finnigan, and Connor Awe.

I was fortunate to have had the opportunity to collaborate with many other research groups. I am thankful to Rich Mirin, Klaus Pierz and Mark Bieler for high quality quantum well samples. Working and interacting with Mark Siemens, Marten Richter, Lazaro Pradilha, Ilya Akimov, and Mack Kira has been a rewarding experience.

I would also like to acknowledge the amazing support staff at JILA especially Kim Hagen and Hans Green in the machine shop, Carl Sauer in the electronics shop, J. R. Raith and Corey Keasling for computing help, and Agnieszka Lynch for administrative help.

Finally, I would like to thank my family and friends for their continued support and encouragement over the years.

Contents

Chapter

Tables

Table

Figures

Figure

Chapter 1

Introduction

Several semiconductor nanostructures such as quantum wells (QWs), nanowires and quantum dots have been developed and studies over the last few decades. QWs are perhaps the most widely studied of these nanostructures. The optical properties of these structures has been the focus of many of these studies. The near-bandgap optical properties of QWs is dominated by excitons, which are correlated electron-hole pairs, for direct bandgap materials at low temperatures. The interaction of exciton with light is complicated due to several factors. The presence of multiple transitions, inhomogeneous broadening, exciton-exciton interaction, etc. provide a plethora of interesting physics problems, which motivate continued research in this field.

The optical excitation in QWs typically last for tens of picoseconds. Thus, ultrafast spectroscopy techniques are ideal for probing the optical properties of excitons. One of the most common techniques is transient four-wave mixing (TFWM) [1]. The exciton coherence lifetime was revealed through the decay of photon echo even in the presence of inhomogeneous broadening [2]. Coupling between exciton states was indicated by the presence of quantum beats in the TFWM signal [3]. Exciton-exciton interactions in the form of excitation-induced dephasing (EID) [4], excitation-induced shift (EIS) [5], and local field effects [6] were studied. Although TFWM experiments have been instrumental in studying exciton physics, it has a few shortcomings. Interpreting the correct behavior from oscillatory signal in the time-domain can be challenging [3]. Furthermore, any spectral dependence of the aforementioned

properties is averaged for an ensemble of oscillators.

Two-dimensional coherent spectroscopy (2DCS), which is an extension of the TFWM technique, overcomes these shortcomings. 2DCS is motivated by a similar technique used in nuclear magnetic resonance studies [7] and was developed in the visible [8] and infrared [9] regimes to study electronic and vibrational properties of molecules. Since then, this technique has also been used to study excitons in semiconductor nanostructures [10]. The spectrally-resolved homogeneous response can be measured in the presence of inhomogeneity [11]. Coupling between multiple states appear as isolated peaks in a 2D spectrum [12]. The measurement of the signal phase has revealed many-body effects such as EIS [13]. The existence of multiple-exciton states have also been studied through 2DCS experiments.

This thesis brings new perspectives to exciton physics in semiconductor QWs using 2DCS. Although many exciton properties have been discussed qualitatively in previous 2DCS experiments, few studies have focused on quantifying these effects, in part due to complicated simulation procedure [14]. A major focus of this work is on developing numerical fitting methods that can be used to quantify these properties.

In Chapter 2, we will present a brief review of some of the basic concepts in semiconductor optics. We will introduce the concept of excitons and discuss some of its properties such as dephasing rate, inhomogeneous broadening, etc. Specific properties of excitons, relevant to this work, will be discussed. The general principles of 2DCS will be explained in Chapter 3. We will discuss modeling the excitonic system through the optical Bloch equations (OBEs). A simple theoretical framework, based on the double-sided Feynman diagrams, which can be used to write down the TFWM signal will be presented. We will highlight the advantages of the 2DCS technique through simulated 2D spectra for various model systems. We will describe the experimental considerations and features of our implementation of 2DCS. The polarization-dependent measurements of the exciton resonance in (110)-oriented GaAs QWs will be presented in Chapter 4. The thermal broadening due to phonons will be discussed. Our studies of the spectral diffusion of excitons will be presented in Chapter 5. The limita-

tions of the previous methods of analyzing spectral diffusion for low sample temperatures will be highlighted. We will quantify spectral diffusion for high sample temperatures through a numerical fitting procedure. Chapter 6 will discuss modeling excitons as interacting bosons. This model will be used to explain the polarization-dependent dephasing rate of excitons. We will separate the exciton-exciton interactions into inter- and intra-mode components. A numerical fitting procedure will be demonstrated to quantify these interaction terms.

The derivation of the OBEs for a two-level system will be discussed in Appendix A. Appendix B will discuss the numerical solution of the OBEs. Some preliminary measurements indicating the contribution of nominally disallowed transition to 2D signal will be presented in Appendix C. The observation of non-monotonic exciton population decay rates will be demonstrated in Appendix D.

Chapter 2

Excitons in Semiconductor Quantum Wells

The optical response of direct-gap semiconductors is dominated by excitons near the fundamental band gap at low temperatures. The interaction of exciton with photons, phonons, other excitons and free carriers affects the optical response of excitons significantly resulting in very rich physics, which has been studied over the past several decades. In this work, we focus on the non-linear light-matter interactions in semiconductor heterostructures, specifically direct band gap GaAs QWs. Before we can discuss the findings of this work, it is imperative to provide a brief summary of the relevant exciton properties.

In this chapter, we will review the properties of excitons in semiconductor QWs that are relevant to the work presented in this thesis. The band structure of direct band gap semiconductors will be discussed in Section 2.1 followed by an introduction to excitons in Section 2.2. In Section 2.3, we will discuss the processes that result in decay of excitations in a semiconductor. Inhomogeneous broadening of the exciton resonance due to fluctuations in QW width will be discussed in Section 2.4. After giving a general description of excitons, we will discuss the specific properties of excitons that will be explored later on in this work. We will also provide an overview of the previous works that have studied these properties. Inhomogeneous broadening of the exciton resonance results in spectral diffusion of the exciton resonance energy, which will be discussed in Section 2.5. The effect of crystal symmetry on excitons will be discussed in Section 2.6. Exciton-exciton interactions significantly affect the light-matter interaction in semiconductors. Some of these interactions will be discussed in

Section 2.7. Finally, we will introduce the concept of thinking of excitons as interacting bosons in Section 2.8.

2.1 Semiconductor quantum well

2.1.1 Bulk Semiconductor

Semiconductors are a class of materials that have electronic properties intermediate between those of an insulator and a metal. The electronic properties of a crystalline material are generally determined by the electronic band structure of the material. Valence band is the highest energy band, which is completely occupied by electrons. The next higher-lying energy band is the conduction band. The electrical conductivity of a material is determined by the distribution of electrons in the conduction and valence bands. In a metal, the conduction band is partially occupied. These high-energy electrons can be easily scattered into unoccupied states on application of an external electric field resulting in the good electrical conductivity of metals. In an insulator, the highest energy electron is in the valence band, which is completely filled. As a result, there is no scope for the intra-band scattering of electrons on the application of an external electric field and insulators do not conduct electricity. The conduction and valence bands in an insulator are separated by an energy gap, known as the band gap energy. The situation for a semiconductor is very similar to that in an insulator. However, the band gap in case of a semiconductor (~ 1 eV) is much less than that in insulators. As a result, electrons can be excited from the valence band to the conduction band by absorption of light in the visible and near infra-red region of the electromagnetic spectrum, which results in many interesting properties of semiconductors.

The repeating pattern of the crystal structure in a semiconductor results in a periodic potential

$$V_0(\mathbf{r}) = V_0(\mathbf{r} + \mathbf{R}_n) \tag{2.1}$$

where $\mathbf{R}_n = n_i \mathbf{a}_i$ is a lattice vector, $\mathbf{a}_i$ is a basis vector, and n_i is an integer. As a result, an

electron in a crystalline lattice must satisfy the Bloch theorem [15]

$$e^{i\mathbf{k}\cdot\mathbf{R}_n}\psi_\lambda(\mathbf{k},\mathbf{r}) = \psi_\lambda(\mathbf{k},\mathbf{r}+\mathbf{R}_n) \tag{2.2}$$

where $\mathbf{k}$ is the crystal momentum, and ψ_λ is the electron wave function. For a one-dimensional lattice with periodicity a, the first Brillouin zone is defined as the range $\left[-\frac{a}{2},\frac{a}{2}\right]$. We will only discuss the range of k in the first Brillouin zone. The Bloch theorem is satisfied by the Bloch wave function

$$\psi_\lambda(\mathbf{k},\mathbf{r}) = \frac{1}{\sqrt{L^3}}e^{i\mathbf{k}\cdot\mathbf{r}}u_\lambda(\mathbf{k},\mathbf{r}) \tag{2.3}$$

where L is the length of each side of a cubic crystal, and u_λ is the Bloch function, which has the same periodicity as the periodic potential in Eq. (2.1). The plane wave part of the Bloch wave function implies that the electronic states are delocalized. The electronic states defined by the aforementioned equations include interactions of electrons with the periodic lattice of nuclei. As a result, these states describe pseudo-particles, which are also called electrons [16].

The band structure for GaAs is shown in Fig. 2.1, which shows a few electronic states around wavevector $k = 0$. A parabolic band dispersion is assumed, in the effective mass approximation limit, around the band extrema at $k = 0$. The energy of the conduction band and two valence sub-bands – heavy hole (HH) and light hole (LH) are shown as a function of the crystal wave-vector k. The minimum of the conduction band and the maxima of the valence sub-bands lie at $k = 0$, which makes GaAs a direct-gap semiconductor. The difference in energy of the conduction band minimum and the valence band maxima is the band gap energy E_g. A photon with energy $\hbar\omega \geq E_g$ can excite an electron from one of the valence bands to the conduction band leaving behind a hole, which is a positively charged pseudo-particle, in the valence band as shown in Fig. 2.1. The linear momentum of a photon is negligible, compared to the crystal momentum at the edge of the first Brillouin zone, and is ignored. In other words, the excited electron and hole are assumed to have equal wave-vectors.

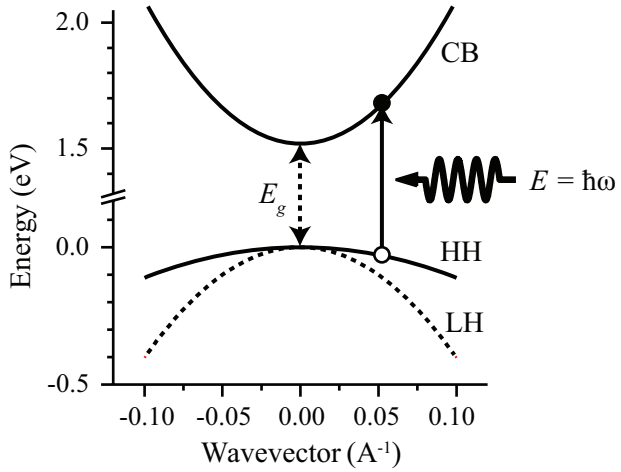

Figure 2.1: Band structure of bulk GaAs showing the conduction (CB) and valence sub-bands – heavy hole (HH), and light hole (LH). The direct band-gap E_g is indicated. A photon with energy $E = \hbar\omega$ can excite an electron, indicated by the solid circle, from a valence band to the conduction band leaving behind a hole, indicated by the empty circle, in the valence band. Note that the HH and LH bands are degenerate at $k = 0$. This figure has been adapted from Ref. [17].

The conduction and valence bands have s- and p-orbital like wave functions, respectively, and, thus, an orbital angular momentum $L = 0$ and 1, respectively. We can define the total angular momentum $J = L + S$ for both the bands. The electron and hole have a spin angular momentum $S = \frac{1}{2}$. Thus, $J = S = \frac{1}{2}$ in the conduction band. The conduction band in Fig. 2.1 shows the degenerate electron states with $J_z = S_z = \pm\frac{1}{2}$, where S_z is the projection of S along the Z direction. We obtain $J = \frac{1}{2}, \frac{3}{2}$ for the valence bands. The $J = \frac{3}{2}$ valence sub-bands are shown in Fig. 2.1. The HH and LH bands are also doubly degenerate states with total angular momentum projections $J_z = \pm\frac{3}{2}$ and $\pm\frac{1}{2}$, respectively. The states with $J = \frac{1}{2}$ constitute the split-off band; this band is separated from the HH and LH sub-bands by a large energy difference and is not shown in Fig. 2.1.

The electron or hole effective mass at $k = 0$ is proportional to the radius of curvature of the respective band, and is given by the relation [15]

$$m_i^* = \hbar^2 \left(\frac{\partial^2 E_i}{\partial k^2} \right)^{-1} \Bigg|_{k=0} \tag{2.4}$$

where the index i indicates either an electron (e) in the conduction band, or a heavy hole (hh), or light hole (lh) in the valence sub-bands. E_i indicates the energy in the same band. The different curvatures of the conduction and valence bands results in different effective masses for electron and holes; $m_e^* = 0.067m_0$, $m_{hh}^* = 0.51m_0$, and $m_{lh}^* = 0.082m_0$ in GaAs for temperatures < 100 K [18]. m_0 is the free electron rest mass. The group velocity of the electron or hole at a particular k is proportional to the slope of the band, and is given by [19]

$$v_i = \frac{1}{\hbar}\frac{\partial E_i}{\partial k} \ . \tag{2.5}$$

Thus, $v_i = 0$ at $k = 0$. This property is relevant for formation of excitons, as we will discuss in Section 2.2.

2.1.2 Quantum well

A QW is formed when a thin layer of a low band gap semiconductor is sandwiched between a higher band gap material, which acts as the barrier. These structures can be grown through molecular beam epitaxy or metal-organic chemical vapor deposition. Multiple layers of QW and barriers are grown to increase the effective light-matter interaction length.

A commonly used QW for studying fundamental many-particle physics in the solid state is GaAs QW with aluminum gallium arsenide $Al_xGa_{1-x}As$ barriers; x is the fraction of Al. Figure 2.2(a) shows the relevant band gaps, at 0 K, for a GaAs QW with $Al_xGa_{1-x}As$ barriers, for $x = 0.3$. The confinement potentials for the conduction and valence bands are also indicated. The QW thickness is usually around 10 nm, which results in confinement of the electron and hole wave functions between the barriers. This confinement results in discrete energy levels indicated by the labels CB, HH and LH for electron, heavy hole and light hole states, respectively, in Fig. 2.2(a).

The electrons and holes, however, are free to move around in the plane of the QW, resulting in the quasi-2D structure of QWs. The band structure for a GaAs QW is shown in

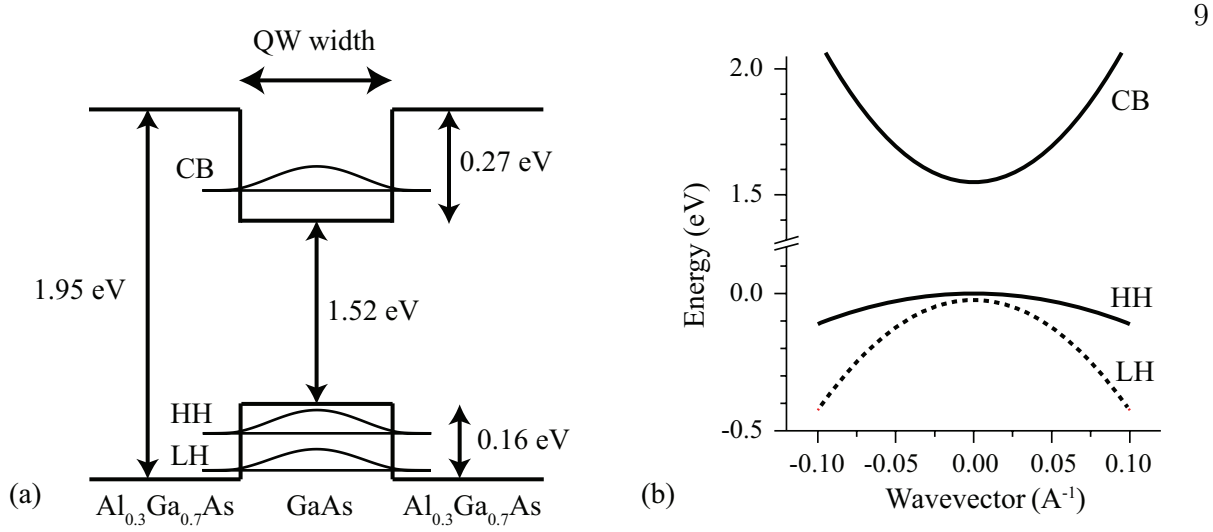

Figure 2.2: (a) Sample structure of GaAs quantum well with $Al_{0.3}Ga_{0.7}As$ barriers. GaAs and $Al_{0.3}Ga_{0.7}As$ have band gaps of 1.52 and 1.95 eV, respectively. The confinement potentials for the conduction and valence bands are 0.27 and 0.16 eV, respectively. The ground state energies of the conduction band electron (CB), heavy hole (HH), and light hole (LH) are indicated along with their wave functions. This figure has been adapted from [20]. (b) Modified band structure for GaAs quantum well showing the conduction (CB) and valence sub-bands - heavy hole (HH) and light hole (LH). Notice the broken degeneracy for HH and LH bands at peak of the valence sub-bands. This figure has be adapted from [17].

Fig. 2.2(b), where the wavevector is defined in the QW-plane. The usual labels are used for the different states. Although this band structure looks very similar to the one for bulk GaAs in Fig. 2.1, quantum confinement affects the electronic band structure in two major ways – (1) the band gap is increased compared to bulk GaAs, and (2) the degeneracy between HH and LH bands at $k = 0$ is lifted. In addition to these effects, lattice mismatch between the QW and barrier materials introduces strain in the QW structure, which also affects the electronic band structure. However, the lattice mismatch between GaAs and $Al_{0.3}Ga_{0.7}As$ is negligible and can be ignored.

In the next section, we will describe the exciton states in semiconductors, which is the focus of this work.

2.2 Exciton states

2.2.1 Bulk excitons

We have discussed the creation of electron-hole pairs in a semiconductor by the absorption of light. A Coulomb attraction potential exists between the excited electrons and holes. This electron-hole pair interaction results in new eigenstates, which are the exciton states. The exciton wave function can be separated into the relative and center-of-mass coordinates. The exciton comprises a positively charged hole and a negatively charged electron. This situation is analogous to that in the hydrogen atom and the relative wave functions of an exciton are similar to the wave functions of the hydrogen atom. One can also define an exciton Bohr radius a_B, which gives the mean distance between an electron-hole pair. However, the center-of-mass wave functions of an exciton are delocalized, similar to the delocalized electron and hole states given by Eq. (2.3).

An essential condition for the creation of an exciton is that the electron and hole should have the same group velocity, which is given by Eq. (2.5). Otherwise, the electrons and holes move apart and cannot form a bound state. For example, the electronic excitation shown in Fig. 2.1 creates electron and hole with opposite group velocities, and will not form an exciton. As a result, optical creation of excitons only occurs $\sim k = 0$ for band structures similar to that shown in Fig. 2.1.

Instead of dealing with electrons and holes separately, it is possible, and convenient, to define exciton states. Figure 2.3(a) shows the dispersion relation for different exciton states. The $E(n, 0) = 0$ point indicates the unexcited semiconductor, i.e. the valence band is completely filled and the conduction band is completely unoccupied. This state can be thought of as the vacuum state in the exciton basis. The shaded electron-hole continuum region starts at the band gap energy E_g at $k = 0$. The $n = 1$ exciton state is red-shifted with respect to the continuum state by the exciton binding energy E_R, which is analogous to the Rydberg energy for the hydrogen atom. A photon with energy $\hbar\omega = E_1$ can create

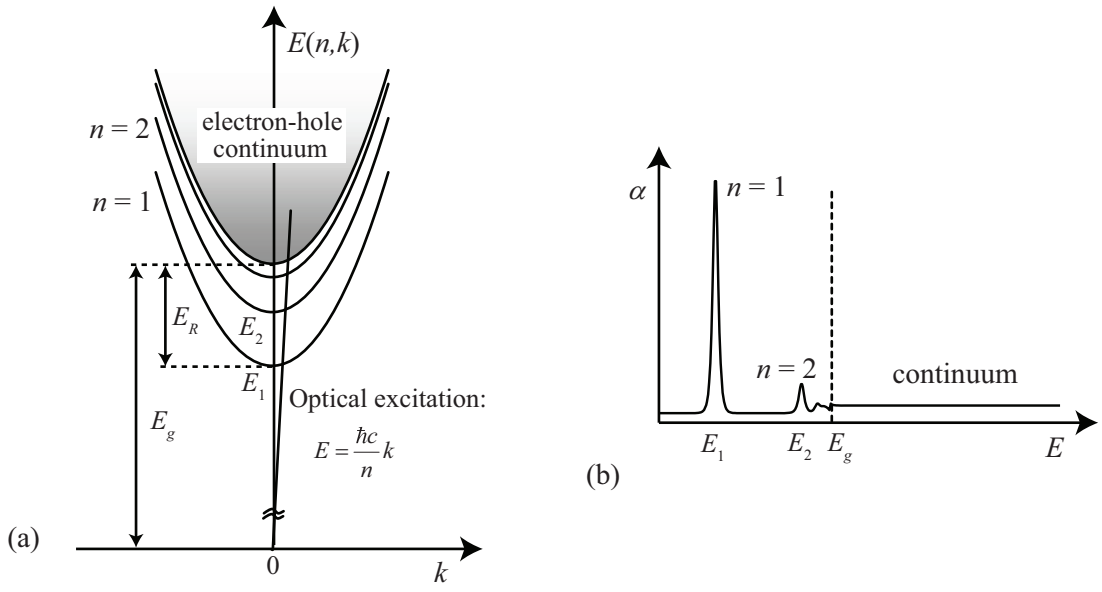

Figure 2.3: (a) Dispersion of the exciton states. The $n = 1$ and $n = 2$ states have energies E_1 and E_2, respectively, at $k = 0$. The exciton ground state energy E_1 is less than the band-gap energy E_g by the exciton ground state binding energy E_R. The gray region indicates the exciton continuum states. (b) The absorption spectrum for bulk GaAs. The sharp peaks are due to the quantized exciton states, while the broad-band absorption is due the continuum states of the exciton. These figures have been adapted from [21].

an exciton in the $n = 1$ state. A small linear momentum is transferred by the photon to the exciton.

For bulk semiconductors, the energy of the n^{th} exciton state is given by

$$E_n = E_g - \frac{E_R}{n^2} \ . \tag{2.6}$$

Similar to the hydrogen atom case, E_R and a_B are related as

$$E_R = \frac{\hbar^2}{2\mu a_B^2} \tag{2.7}$$

where $\mu = \frac{m_e^* m_h^*}{m_e^* + m_h^*}$ is the reduced mass of the exciton and $a_B = \frac{\epsilon \hbar^2}{\mu e^2}$ with dielectric constant ϵ. m_e^* and m_h^* are the electron and hole effective masses, respectively. For the HH exciton in bulk GaAs, $a_B = 14nm$ and $E_R = 4.2$ meV [22].

The discrete exciton states can be readily identified as the sharp resonances in the absorption spectrum shown in Fig. 2.3(b). The broad band absorption feature is due to

absorption in the continuum states. The overlap integral between the electron and hole wave functions determines the inter-band transition dipole moment and oscillator strength. This overlap integral is significantly greater for the exciton states compared to the continuum states, which results in a higher absorption coefficient for the exciton states. The oscillator strength for the various exciton state $f_n \propto n^{-3}$ [15] and results in a fast decrease in absorption coefficient for higher energy exciton states.

2.2.2 Quantum well excitons

Quantum confinement, in a QW, modifies the density of states in the continuum. The general exciton properties discussed in Section 2.2.1 are still valid in QWs. However, there are a few quantitative differences. The energy of the n^{th} exciton state in a QW is given by [15]

$$E_{n,QW} = E_{g,QW} - \frac{E_{R,QW}}{\left(n - \frac{1}{2}\right)^2} \tag{2.8}$$

where the same definition is used as earlier and subscript QW is used to denote that the quantities are for a QW. For infinite potential barriers, $a_{B,QW} = \frac{1}{2}a_B$ and $E_{R,QW} = 4E_R$, which is not the case in reality. For example, $E_{R,QW} \approx 8.5$ meV for the HH exciton in GaAs QWs with $Al_{0.3}Ga_{0.7}As$ barriers [23, 24]. Finally, the change in the oscillator strength for different exciton states follows the relation $f_n \propto \left(n - \frac{1}{2}\right)^{-3}$ [15].

Figure 2.4 shows the experimentally measured absorption spectrum for a four-period 10-nm-wide GaAs QW with 10-nm wide $Al_{0.3}Ga_{0.7}As$ barriers. The absorption spectrum comprises two peaks corresponding to absorption in the $n = 1$ state of the HH and LH excitons. The two peaks are separated because the degeneracy between the HH and LH bands is lifted due to quantum confinement as shown in Fig. 2.2(b).

2.2.3 Polarization selection rules

The angular momentum values for the electron and hole states were discussed in Section 2.1.1. Electrons are excited from the valence band to the conduction band by the absorption

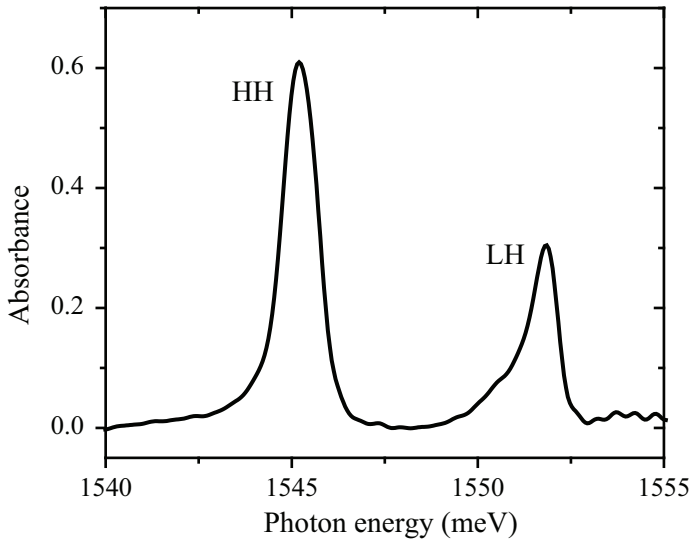

Figure 2.4: Measured absorption spectrum for a four-period 10-nm-wide GaAs quantum well with 10-nm-wide $Al_{0.3}Ga_{0.7}As$ barriers showing the heavy hole (HH) and light hole (LH) peaks.

of photons. As the photon is absorbed, its momenta – angular and linear – are transfered to the electron. The linear momentum of a photon is negligible and can be ignored for all practical purposes. A photon also has unit spin angular momentum – +1 and -1, respectively, for σ_+ and σ_- polarized light. The total angular momentum should be conserved during inter-band transitions. This conservation involves the spin angular momentum of light, and results in the polarization selection rules shown in Fig. 2.5.

Figure 2.5(a) shows all the optically allowed transitions of electrons from the valence band to the conduction band. σ_+ polarized light can excite electron with $J_z = -\frac{3}{2}$ $\left(J_z = -\frac{1}{2}\right)$ from the HH (LH) band to the conduction band with $S_z = -\frac{1}{2}$ $\left(S_z = +\frac{1}{2}\right)$. Alternatively, σ_- polarized light can excite electron with $J_z = +\frac{3}{2}$ $\left(J_z = +\frac{1}{2}\right)$ from the HH (LH) band to the conduction band with $S_z = +\frac{1}{2}$ $\left(S_z = -\frac{1}{2}\right)$. The HH and LH states are coupled through the electron states. The $S_z = -\frac{1}{2}$ electron state couples the $J_z = -\frac{3}{2}$ HH state to the $J_z = +\frac{1}{2}$ LH state. Similarly, the other HH and LH states are coupled through the $S_z = +\frac{1}{2}$ electron state.

Another, more convenient, way to understand the polarizations selection rules is in the

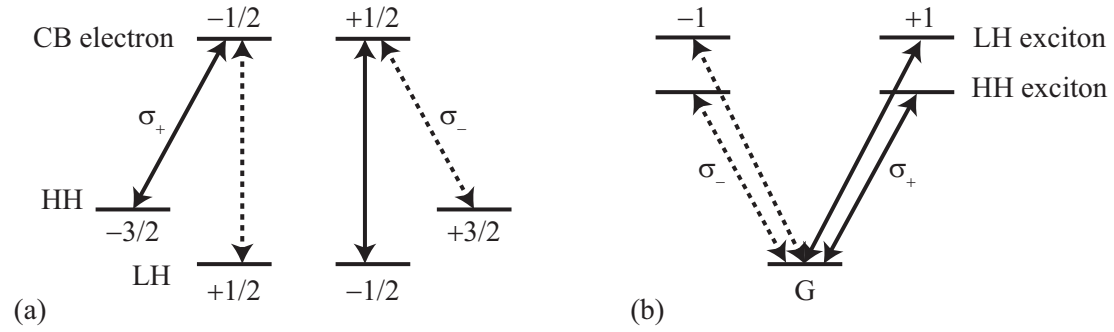

Figure 2.5: (a) Polarization selection rules for excitons in the electron-hole basis. The labels indicate the projection of the total angular momentum J_z along the growth direction for the different electron and hole states. The spin of the photon (± 1) is transfered to the electron as it is excited from the conduction band to the valence band by circularly polarized light. σ_+ and σ_- polarized light is indicated by solid and dashed arrows, respectively. (b) The same transitions are shown in the exciton basis. The exciton states are labeled with spin ± 1 indicating the circular polarization of light that was used to create the exciton.

exciton picture, as shown in Fig. 2.5(b). In the exciton picture, both HH and LH exciton states are considered to be doubly degenerate state with ± 1 spin and the exciton is created with a spin, which is equal to the photon spin. σ_+ and σ_- polarized light creates HH and LH excitons with $+1$ and -1 spins, respectively.

Now that we have discussed excitons in QWs and how they are created through optical excitation, we would like to discuss the processes that lead to a decay of these excitations. We will only discuss the decay processes relevant for excitons.

2.3 Decay processes

We will use the density matrix formalism to describe excitations of the excitonic system. Such a formalism is especially useful for an ensemble of particles, as is the case for excitons. A two-level system with ground and excited states, respectively, can be described using the following density matrix

$$\rho = \begin{pmatrix} \rho_{gg} & \rho_{ge} \\ \rho_{eg} & \rho_{ee} \end{pmatrix} \tag{2.9}$$

where the indices e and g are used for the ground and excited states, respectively. Thus, the diagonal terms of the density matrix (ρ_{gg} and ρ_{ee}) denote the population in the ground and excited states, respectively; $\mathrm{tr}(\rho) = 1$ for a closed system. The two off-diagonal elements of the density matrix (ρ_{ge} and ρ_{eg}) are complex conjugates of each other and denote a coherent superposition, or coherence, between the two states. The coherence has an associated phase, which evolves with the frequency given by the energy difference between the two states. In the case of excitons, we can assume the excited state to be one of the exciton states.

If the excited state has a lifetime T_1, the following equation describes the evolution of the excited state population with time t

$$\rho_{ee}(t) = \rho_{ee}(0)\mathrm{e}^{-\frac{t}{T_1}} \ . \tag{2.10}$$

In the frequency domain, we obtain a Lorentzian line shape with width quantified by $\frac{1}{T_1}$. A similar relation is generally used to describe evolution of the coherence between the ground and exciton states

$$\rho_{eg}(t) = \rho_{eg}(0)\mathrm{e}^{-i\omega t}\mathrm{e}^{-\frac{t}{T_2}} \tag{2.11}$$

where T_2 is the dephasing time and the energy between the states is $\hbar\omega$. The term $\mathrm{e}^{-i\omega t}$ accounts for the phase evolution of the coherence. A decrease in population of the excited state also results in decay of the coherence. In the absence of other coherence decay mechanisms, the population and dephasing times are related as

$$T_2 = 2T_1 \tag{2.12}$$

in a closed system. If the decay of population results in the emission of photons, due to electron-hole recombination in the case of excitons, the lifetime and dephasing times are said to be radiatively limited. Bulk exciton population lifetime in GaAs is ~ 1 ns [25]. The exciton lifetime in QWs depends on the growth and sample quality. Radiatively limited lifetimes of 10-30 ps have been reported for GaAs QWs [2, 26].

In addition to radiative decay, non-radiative decay is also possible in semiconductors. For instance, trap sites due impurities or imperfections in crystal lattice can result in population decay in addition to that due to electron-hole recombination. Another important non-radiative decay process is "pure dephasing", which is a decay in coherence without any corresponding population decay. Pure dephasing can also be understood as a loss of phase-memory during the evolution of the coherence. Exciton-exciton scattering is an important source of pure dephasing in QWs. This effect is same as the phenomenological many-body effect – excitation-induced dephasing (EID), which is described in Section 2.7. In general, the combined effect of all the pure dephasing mechanisms is taken into account through the relation

$$\frac{1}{T_2} = \frac{1}{2T_1} + \frac{1}{T_2^*} \tag{2.13}$$

where T_2^* is the effective pure-dephasing lifetime.

In order to obtain Eq. (2.13), an exponential coherence decay, similar to Eq. (2.11), is assumed for the pure-dephasing processes. This assumption is known as the Markovian approximation, which assumes that the phase-memory loss occurs instantaneously. As the discussion on spectral diffusion in Section 2.5 will highlight, the Markovian approximation is not valid for QW excitons. Spectral diffusion occurs due the presence of inhomogeneous broadening in the exciton resonances, which will be discussed in the next section.

2.4 Inhomogeneous broadening

In our treatment of excitons, we have assumed a single energy for each state. This condition would be true for perfectly smooth layers of the barrier and QW materials, which cannot be realized in practice. Spatial variations in QW widths are introduced in the growth process as indicated in Fig. 2.6. These variations result in different exciton resonance frequency at different spatial locations. Thus, instead of a single, well-defined resonance energy, all the exciton states have an inhomogeneous distribution of resonance energies.

This distribution of exciton energies results in different phase evolution of distinct frequency components. The collective coherence is called the macroscopic polarization P, which is defined by the relation

$$P = N \,\mathrm{tr}(\mu\rho) \tag{2.14}$$

where N is the total number of oscillators and μ is the transition dipole moment matrix

$$\mu = \begin{pmatrix} 0 & \mu_{ge} \\ \mu_{ge} & 0 \end{pmatrix} \tag{2.15}$$

where the non-zero elements are complex conjugates of each other. Since an optical transition involves two states, the diagonal elements of the dipole matrix are zero. In the presence of inhomogeneity, the macroscopic polarization can decay much faster than the dephasing time discussed in Section 2.3.

Due to the variations in the QW-width, areas of larger width can be surrounded by smaller width regions. Such a situation results in a small in-plane confinement potential for excitons in the areas with larger QW width since the exciton energy increases with decreasing QW width. These areas are known as localization sites and can be as big as 10s of nanometers in size [27, 28]. A low energy exciton can be trapped in a localization site, as shown in Fig. 2.6, resulting in a localized exciton. An extreme limit of such a localization results in the formation of natural quantum dots [29]. Thus, the treatment of excitons as perfectly delocalized states is not strictly valid in the presence of inhomogeneous broadening. The

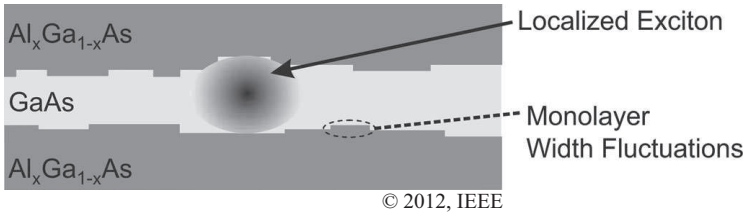

Figure 2.6: Illustration of well width fluctuations in a quantum well sample. These fluctuations result in an inhomogeneous distribution of the resonance energies of the exciton state. A localized exciton, which is trapped due to the width fluctuations is indicated. This figure has been reproduced from Ref. [10].

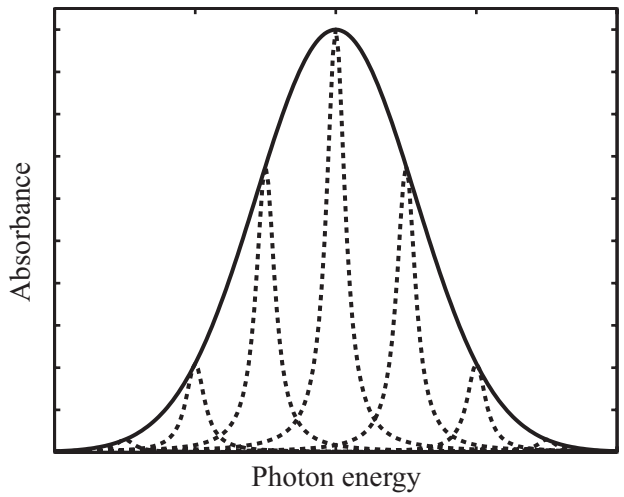

Figure 2.7: A broad absorption peak shown by the solid line can be be composed of several narrower peaks such as shown by the dotted lines.

excitons with high resonance energy, however, are still delocalized. Localized and delocalized excitons have distinct properties, such as exciton decay times [30]. Interface roughness also introduces non-radiative decay channels.

As a result of the inhomogeneous broadening, the peaks in the absorption spectrum shown in Fig. 2.4 result from several narrower peaks. This situation is depicted in Fig. 2.7. The peaks indicated by the dotted lines are the narrower resonances. We have used a Lorentzian distribution for these peaks, which is consistent with the exponential decay of excitations discussed in Section 2.3. The linewidth of the narrow peaks is the homogeneous linewidth. A collection of these spectrally separated narrow peaks results in the inhomogeneously broadened exciton resonance indicated by the solid line in Fig. 2.7. The inhomogeneous distribution is usually a Gaussian function, as we have assumed here. The linewidth of the Gaussian distribution gives the inhomogeneous linewidth of the system. The width fluctuations, and, consequently, the inhomogeneous linewidth of excitons in QWs depends significantly on growth conditions. Improved growth techniques have resulted in a reduction in the inhomogeneous linewidth from a few meVs [27] to less than a meV [31].

Figure 2.7 depicts all the Lorentzian resonances with the same width, which is not

necessarily true for excitons in QWs. The localized excitons have a lower linewidth than delocalized excitons. The linewidth of the localized excitons is nominally independent of the resonance energy. The linewidth of the delocalized excitons, however, increases with an increase in the resonance energy. The lowest resonant energy of a delocalized exciton is the mobility edge, which usually lies at the center of the inhomogeneous distribution of exciton resonance energies [32, 33].

We have provided a general overview of excitons in semiconductor QWs. In the following sections, we will introduce specific properties of QW excitons – spectral diffusion, effect of crystal symmetry on excitonic properties, exciton-exciton interactions, and treating excitons as interacting bosons, which will be explored in detail in rest of this work.

2.5 Spectral Diffusion

Due to the inhomogeneity in the exciton resonance energy, spatial migration of an exciton, in the QW plane, results in a change in the resonance energy of the exciton. This phenomenon is spectral diffusion [34]. The migration of excitons involves interactions with phonons – the exciton energy increases and decreases on absorption and emission of phonons, respectively. This effect is similar to the time-dependent frequency fluctuations seen in atomic [35] and molecular [36, 37] systems. The time-dependent transition energy ω can be defined as $\omega(T) = \langle\omega\rangle + \delta\omega(T)$, where T is the time, $\langle\omega\rangle$ is the time-averaged value of the transition energy and $\delta\omega$ is the difference between the instantaneous and mean values of the transition energy. Additionally, one can define a normalized frequency-frequency correlation function

$$C(T) = \frac{\langle\delta\omega(T)\delta\omega(0)\rangle}{\langle\delta\omega^2\rangle} \tag{2.16}$$

where the average is an ensemble average, and $\langle\delta\omega^2\rangle$ is the inhomogeneous width. The Markovian approximation for pure dephasing, discussed in Section 2.3, assumes δ-function correlated frequencies [38]. Spectral diffusion essentially violates this assumption and, thus,

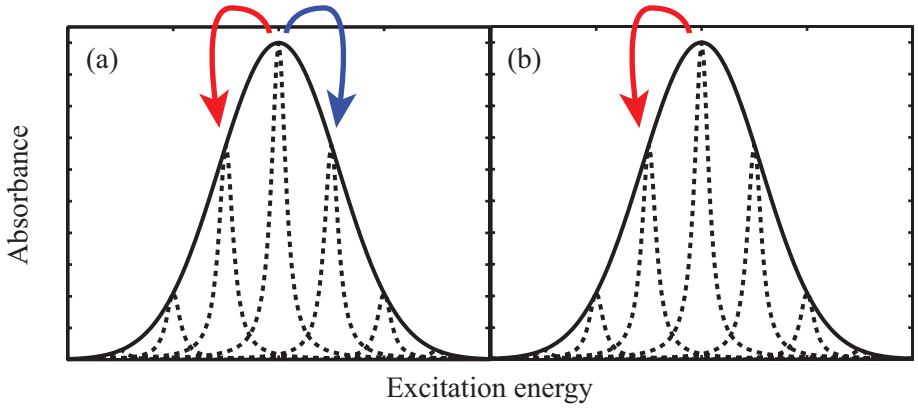

Figure 2.8: Illustration of spectral diffusion. (a) Spectral diffusion in the strong redistribution approximation. Red and blue arrows indicate a decrease and increase in the energy of the excitations. (b) Preferential relaxation results in violation of the strong redistribution approximation.

is quantified through the decay in $C(T)$ as T increases in several systems, including QW excitons [39, 40, 41].

The description of spectral diffusion presented above is valid only in the strong redistribution approximation, which assumes that spectral diffusion results in an equal redistribution of the transition energy of an excitation to higher and lower energies as indicated in Fig. 2.8(a). While this approximation is valid for atomic and molecular systems, which lack static inhomogeneity, we will show in Chapter 5 that this assumption is not valid for spectral diffusion of excitons in QWs, especially for low (< 25 K) sample temperatures. This situation is similar to the one shown in Fig. 2.8(b). Furthermore, we will also show that even for high sample temperatures, when the strong-redistribution approximation is valid, $C(T)$ does not decay exponentially, which is generally assumed in the Gauss-Markov approximation [38, 40].

2.6 Crystal symmetry

Different semiconductor materials belong to different crystal structure categories and, thus, have different structural symmetry. A material's structural symmetry affects its electronic properties significantly. The same holds true in the case of QWs. In addition to

changing material composition, it is possible to change the symmetry of a QW structure depending on the growth direction. While the most commonly used GaAs QWs are grown along the (001) crystal axis, GaAs QWs in other growth directions such as (110), (111), and (113) are also possible. All these QWs have different symmetries and their distinct optical properties.

In addition to (001)-oriented GaAs, in this work, we will discuss excitons in (110)-oriented GaAs QWs, which have garnered significant interest recently for optical generation of spin currents [42] and terahertz radiation [43]. For a (110)-oriented GaAs QW, where the QW itself is symmetric, the in-plane symmetry is reduced to C_{2v} point group compared to T_d for bulk GaAs and D_{2d} for an undoped (001)-oriented GaAs QW. The reduced symmetry results in the different spin (angular momentum) states of the conduction (valence) bands being split in k-space along the $[1\bar{1}0]$ crystal axis while no splitting exists along the [001] crystal axis [44, 45], and, along with the k-linear terms of the transition dipole moment, contributes to the generation of spin currents. The schematic band structures for the first conduction ($S_z = \pm 1/2$) and HH valence ($J_z = \pm 3/2$) bands along the X and Y directions are shown in Figs. 2.9(a) and 2.9(b), respectively. S_z and J_z are the projections, on the Z-axis, of the spin of an electron and the total angular momentum of a HH, respectively. We use a co-ordinate system with the X, Y and Z axes aligned along the [001], $[1\bar{1}0]$ and [110] crystal axes, respectively, of the sample.

Very long spin relaxation times [47, 48] and generation of spin currents by optical excitation [42] in these nanostructures find applications in terahertz generation [43] and spintronics. In coherent control experiments, carrier dephasing rates influence the optically generated currents in bulk GaAs [49] and (001)-oriented QWs [50]. A recent coherent control study on (110)-oriented GaAs QWs revealed novel photocurrents that directly depend on exciton polarization dephasing [51]. The contribution of excitons to spin currents [52] and the electron spin relaxation time [53] were also inferred. However, not many works have studied excitonic effects in these QWs. We will present measurements of the exciton dephasing times

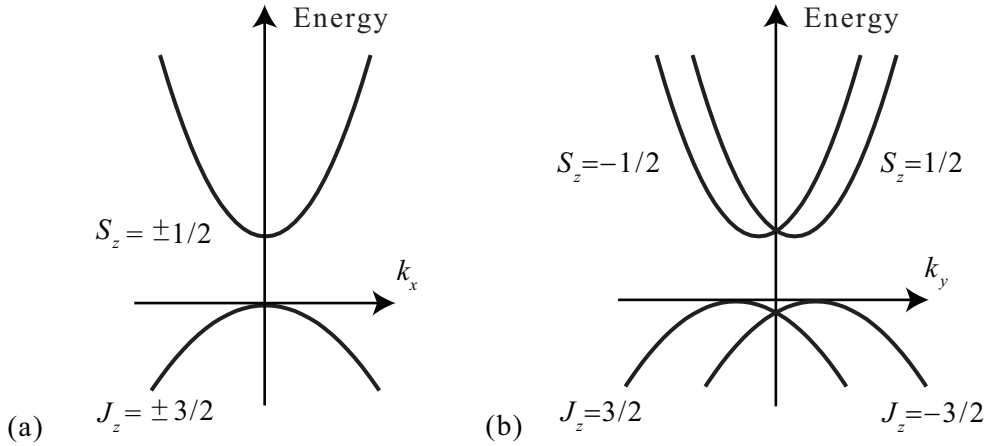

Figure 2.9: An illustration of the energy levels for the conduction and HH valence bands in (110)-oriented GaAs QWs, as a function of wave vector along [001] (k_x) and [1$\bar{1}$0] (k_y) directions are shown in (a) and (b), respectively. The energy is shown for the conduction (HH valence) bands with spin and angular momentum states $S_z = \pm 1/2$ and $J_z = \pm 3/2$, respectively. The figure has been adapted from Ref. [46].

for (110)-oriented GaAs QWs in Chapter 4 [46].

2.7 Exciton-Exciton Interactions

Our discussion on excitations in a semiconductors is only strictly valid for an unexcited sample. Excitations in a semiconductor affect its electronic properties significantly due to several effects such as phase-space filling, screening, band gap renormalization, etc [16]. The semiconductor Bloch equations (SBEs), which are a modification of the more widely used optical Bloch equations (OBEs), are used for a rigorous description of these effects [54]. However, a phenomenological treatment of these effects in terms of exciton-exciton interactions, dubbed many-body effects, is usually sufficient to gain a physical understanding of these effects [5]. These effects are especially relevant for non-linear light-matter interactions, which is the central theme of this work. Some of the prominent many-body effects are excitation-induced dephasing (EID), excitation-induced shift (EIS), local field corrections, and higher order correlations such as biexcitons.

EID refers to an increase in the dephasing rate of the excitonic coherence with increase

in the exciton density [55, 4]. This effect is analogous to the thermal collisional broadening in case of atoms [56].

EIS is a complimentary effect due to which the exciton resonance energy changes with the exciton density. Two competing effects contribute to EIS – (1) screening of the Coulomb interaction between electrons and holes results in a blue-shift in the exciton resonance due to a decrease in the exciton binding energy, and (2) band gap renormalization results in a red-shift. These two effects almost exactly cancel each other out for excitons in bulk semiconductors, resulting in no measurable EIS [57]. In case of excitons in QWs, however, the screening effect dominates and results in a blue-shift of the exciton resonance with an increase in the exciton density [58, 59].

Local-field correction for excitons [60, 6] accounts for the fact that in addition to the external electric fields, the macroscopic polarization inside the sample also interacts with the system. The effect of local-field correction has been shown to be very similar to EIS [5].

Higher order correlations between two or more electron-hole pairs have significant effect on the non-linear optical response of QWs. Biexciton, which is a bound state of two excitons with opposite spins, is an example of such a higher-order correlation [61]. Many other correlated states of electron-hole pairs have been identified in QWs recently [62, 63, 64, 65]. Presently, we will limit our discussion to that of biexcitons.

Effect of biexcitons can be included phenomenologically by adding a bound two-exciton state to the energy level scheme, as shown in Fig. 2.10 [66, 67]. The biexciton state has a energy that is less than twice the exciton state energy by the biexciton binding energy Δ_B. Two excitons with opposite spins form a biexciton, which is analogous to a hydrogen molecule. As a result, biexciton is a spin 0 pseudo-particle. The polarization selection rules for the exciton-biexciton system, in the basis of circularly polarized light, is shown in Fig. 2.10(a). Opposite circularly polarized photons are needed to create a biexciton. An equivalent polarization selection rule, in the linear polarization basis, is shown in Fig. 2.10(b) [67].

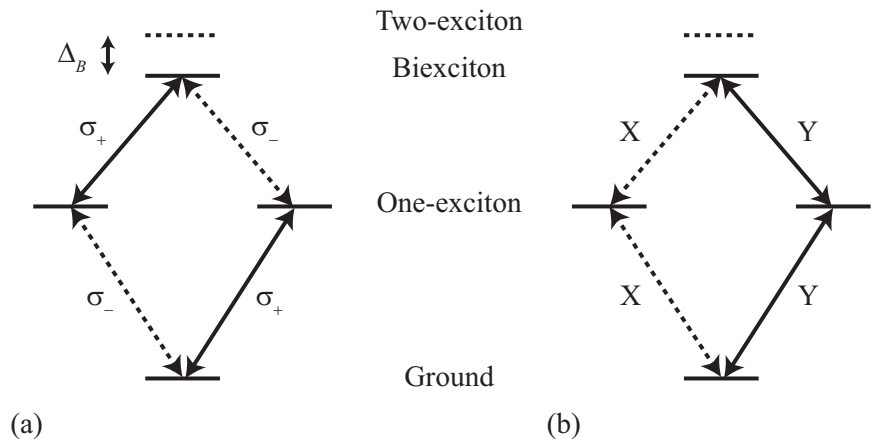

Figure 2.10: The ground, one-exciton, two-exciton and biexciton states are shown with polarization selection rules in the (a) circular and (b) linear bases. The energy of the biexciton state is less than that of the two-exciton state by the the biexciton binding energy Δ_B. σ_+ and σ_- polarized light is indicated by solid and dashed arrows, respectively, in (a). Orthogonal linear polarizations – Y and X are indicated by solid and dashed arrows, respectively, in (b).

2.8 Exciton as a boson

Excitons are spin 1 pseudo-particles. Although excitons are composed of two fermions – electrons and holes, it has been shown that excitons can be considered as bosons at low excitation densities, where phase-space filling effects are minimal [68, 69, 70]. The bosonic character of excitons is invoked to describe excitons in microcavities [71] and macroscopic condensed phases of excitons [72]. Also, some effects of the bosonic character of excitons on FWM signal has been discussed [73, 74].

Nevertheless the validity of modeling excitons as bosons has been under debate [75]. It has been argued that the fermionic nature of electrons and holes masks the bosonic nature of excitons. Also, it has been claimed that the bosonic model of excitons does not take into account the higher-order correlations, even at low excitation densities [76].

In Chapter 6 we will discuss the origin of FWM signal when excitons are modeled as interacting bosons. We will show that such a model is consistent with FWM and 2DCS experiments performed in the $\chi^{(3)}$-regime as argued by Shirane et al. [74]. Additionally,

modeling excitons as interacting bosons has several advantages. Firstly, we find that the polarization dependent exciton dephasing rate [77, 78, 79] is a direct consequence of the bosonic nature of excitons. Secondly, exciton-exciton interactions are included in a physically intuitive and straightforward way, which is significantly simpler than using either semiconductor Bloch equations [54] or the phenomenological many-body effects [5]. The simplified modeling enables **quantifying** the exciton-exciton interactions. Finally, we will see that multiple exciton modes are excited optically in a FWM experiment, and the exciton-exciton interactions can be separated into inter- and intra-mode interaction. Power dependent experiments are used to separately quantify these interactions.

2.9 Samples

In this work, we will discuss experimental findings obtained from a couple of different QW samples. We will discuss the samples that we have used here.

2.9.1 (001)-Oriented GaAs quantum well

The (001)-oriented GaAs QW has been used to study spectral diffusion and the bosonic model of excitons. Since similar samples have been studied extensively, we have used this sample to demonstrate new perspectives that we have obtained through 2DCS experiments.

This sample comprises a series of four uncoupled 10-nm-wide QWs with 10-nm-wide $Al_{0.3}Ga_{0.7}As$ barriers. The absorption spectrum in Fig. 2.4 is obtained from this sample. This sample was grown and provided to us by Richard Mirin at National Institute of Standards and Technology, Boulder, USA.

2.9.2 (110)-Oriented GaAs quantum well

As mentioned in Section 2.6, we have also studied excitons in (110)-oriented GaAs QWs. These QWs were grown by Klaus Pierz's group at Physikalisch-Technische Bundesanstalt, Braunschweig, Germany.

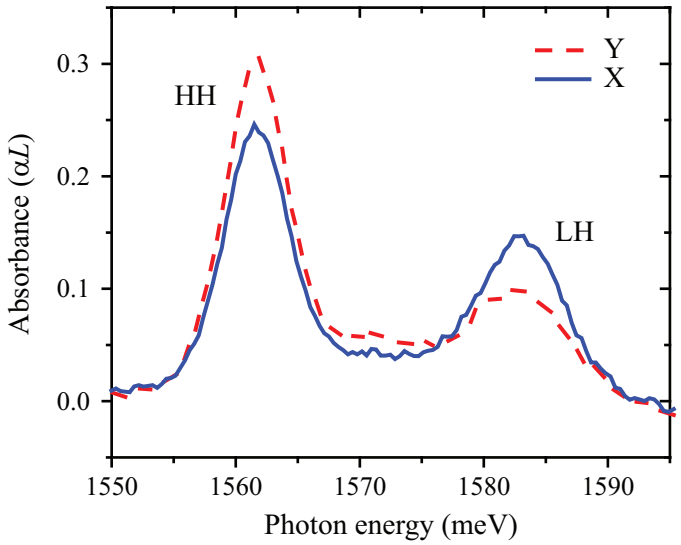

Figure 2.11: Measured absorption spectrum for a 10 period 8-nm-wide (110)-oriented GaAs quantum well with 8-nm-wide $Al_{0.3}Ga_{0.7}As$ barriers. The HH and LH resonances are marked. Note the different absorption coefficients for orthogonal linear polarizations – X and Y.

We have studied 10 period samples with 5 and 8 nm wide QWs separated by 8-nm-wide $Al_{0.3}Ga_{0.7}As$ barriers. Figure 2.11 shows the absorption spectra for the 8-nm-wide QW for X and Y polarized light, which are aligned with the [001] and $[1\bar{1}0]$ crystal axes, respectively. The polarization dependent absorption arises from the broken symmetry in the QW plane discussed in Section 2.6, and has been reported earlier [80]. Absorption at the HH exciton resonance is higher for light polarized along the $[1\bar{1}0]$ crystal axis. In case of the LH exciton resonance, higher absorption coefficient is measured for light polarized along the [001] crystal axis.

Now we are ready to discuss studies of excitons in QWs using 2DCS, which will be presented in the next chapter following an overview of the experimental and theoretical methods.

Chapter 3

Two-Dimensional Coherent Spectroscopy

Various spectroscopic techniques are used to investigate a material's properties through light-matter interaction. Electronic and structural properties can be probed by using light fields of different wavelengths. The most simple techniques, such as linear absorption and photoluminescence reveal information about the various transitions in a system. However, this information is not sufficient to describe more complicated systems with multiple resonances and/or inhomogeneity. This is especially true for semiconductor heterostructures.

Strong many-body interactions in semiconductors complicate things even further. Non-linear spectroscopy is sensitive to many-body interactions because of higher excitation densities than linear techniques, and can be broadly classified into coherent and non-coherent techniques. The difference between the two class of experiments is in the sensitivity, or lack thereof, to phase fluctuations of quantum mechanical superpositions between states that is excited in the sample. Coherent spectroscopy techniques are sensitive to these fluctuations and, thus, are more sensitive to many-body interactions. Furthermore, knowledge about the coherent response of a system can be utilized for coherent control. For instance, chemical reactions can be controlled through optical pulses [81, 82]. Coherent control of excitons and photocurrents in QWs has also been studied [83, 84, 49].

Perhaps the most commonly used non-linear coherent spectroscopy technique is the transient four-wave mixing (TFWM) experiment. Although, a variety of experimental implementations exist, a common characteristic of this class of experiments is that the signal

is measured as a function of delay(s) between multiple ultrafast laser pulses. A TFWM experiment is ideal to study excitons in semiconductors, which have dynamics in the range of a few to tens of picoseconds.

Two-dimensional coherent spectroscopy (2DCS) is a relatively new spectroscopic technique, which is inspired from two-dimensional Fourier transform nuclear magnetic resonance spectroscopy [7]. Since the first demonstration of 2DCS in the optical domain [8], the technique has been extended to the terahertz [85], infra-red [9, 86] and ultra-violet [87, 88] frequency regimes. Recently, the technique has been extended to three frequency dimensions [89, 90]. 2DCS has been used extensively to study a variety of materials such as atomic vapors [91, 92, 93, 94], molecules [9, 86], colloidal nanocrystals [95], energy transfer in light-harvesting complexes [96], semiconductor heterostructures [17, 62, 97], and Nitrogen vacancy centers in diamond [98]. 2DCS is an extension of the TWFM experiment, with the addition of phase-sensitive detection and precise scanning of time delay(s). The detection of signal phase has numerous advantages. 2DCS studies of excitons in QWs have been instrumental in understanding many-body interactions – the effect of many-body interactions on the signal phase [13], existence of multiple exciton correlation states [62, 63, 64], limitations of mean-field theories through comparison with experiments [99] have been some of the important discoveries.

In this chapter, we will discuss the principles of optical 2DCS. We will start off with a discussion on the TFWM technique, since it is essentially a precursor to 2DCS experiments. Next, we will provide an overview of the relevant experimental and theoretical details of 2DCS. Finally, we will review previous studies of QW excitons using 2DCS.

3.1 Transient four-wave mixing

TFWM is one of the most commonly used non-linear spectroscopy techniques. Strictly speaking, the signal field is proportional to the cube of the incident optical electric field in a TFWM experiment. Although, some TFWM signal would be radiated by a single incident

optical pulse, the non-linear signal would be buried in the much stronger linear signal. As a result, two or three pulses are used so that the non-linear response can be isolated using frequency modulations for collinear and phase-matching for non-collinear geometries. Furthermore, the delay between multiple pulses can be scanned to probe excitation dynamics.

3.1.1 Three-pulse realization

The two- and three- pulse implementations of TFWM are very similar; we will only discuss the three-pulse experiments since that discussion can be easily extended to discuss 2DCS experiments. Additionally, we would limit our discussion to degenerate TFWM, in which all the excitation pulses have identical spectrum. One realization of three excitation pulses, A, B and C, in a typical TFWM experiment is shown in Fig. 3.1(a). The delay between consecutive excitation pulses are τ and T. The signal is radiated during time t after pulse C is incident on the sample.

The electric field for each pulse is

$$\mathscr{E} = \frac{1}{2}|E_i|[\mathrm{e}^{i(\mathbf{k}_i\cdot\mathbf{r}-\omega_i t')} + c.c.] \tag{3.1}$$

where $|E_i|$ is the electric-field envelope, $\mathbf{k}_i$ is the wavevector, and ω_i is the center frequency of pulse i. Time is indicated by t' to distinguish it from the delay t in Fig. 3.1(a). Each incident pulse acts once (either the conjugated or the non-conjugated part) and the radiated signal field is proportional to $|E_\mathrm{A}||E_\mathrm{B}||E_\mathrm{C}|$. One of the pulses is conjugated so that the signal frequency is close to the frequency of the incident pulses. For instance, pulse A is the conjugated pulse in Fig. 3.1(a), and is labeled A*. Thus, the radiated signal has a frequency

$$\omega_\mathrm{S} = -\omega_\mathrm{A} + \omega_\mathrm{B} + \omega_\mathrm{C} \tag{3.2}$$

where ω_A, ω_B, and ω_C are the center frequencies of the incident pulses. The negative sign for ω_A is used since A is the conjugated pulse. Since the conjugate pulse is the first pulse that is incident on the sample, this pulse sequence is referred to as the S_I time ordering.

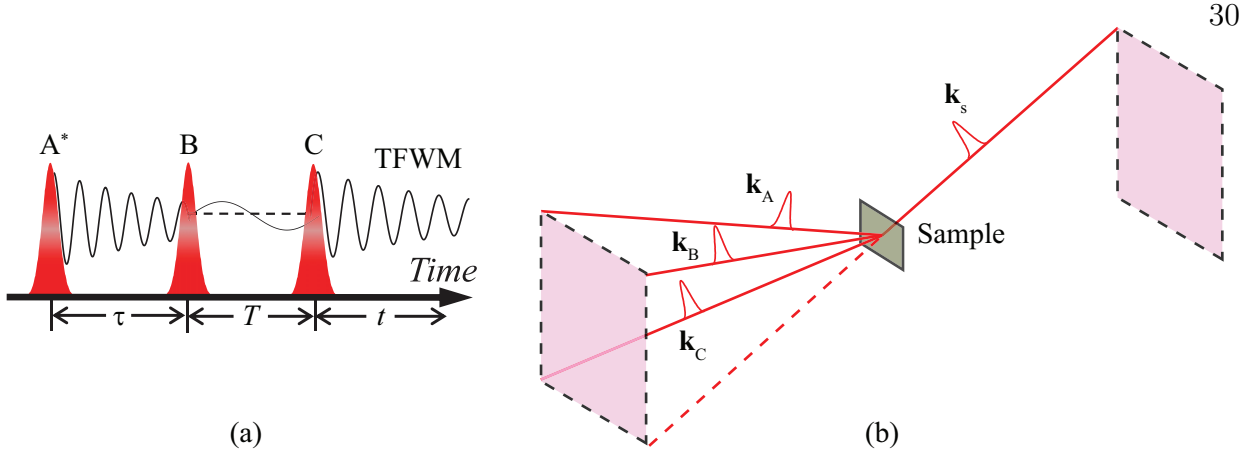

Figure 3.1: (a) Three excitation pulses, A, B, and C, in the S_I time ordering in a transient four-wave mixing (TFWM) experiment. (b) A typical three-pulse non-collinear geometry. The excitation pulses are incident on the sample along the directions indicated by $\mathbf{k}_{A,B,C}$. The TFWM signal is emitted along direction $\mathbf{k}_S$.

Several TFWM signals with different pulses acting as the conjugated pulse are radiated by the sample. Usually one of these signals is isolated experimentally, which sets the pulse that acts as the conjugated pulse. A non-collinear geometry of incident pulses and detected signal is shown in Fig. 3.1(b) for a three-pulse TFWM experiment. The excitation pulses are incident along the directions given by $\mathbf{k}_A$, $\mathbf{k}_B$, and $\mathbf{k}_C$. The signal is detected in the phase-matching direction

$$\mathbf{k}_S = -\mathbf{k}_A + \mathbf{k}_B + \mathbf{k}_C. \tag{3.3}$$

The direction in which the TFWM signal is detected determines which pulse acts as the conjugated pulse. The $-$ sign for $\mathbf{k}_A$ means that pulse A is conjugated.

3.1.2 Theoretical description

We will now discuss the origin of TFWM signal, from a physical perspective, for a two-level system shown in Fig. 3.2(a) with the ground and excited states denoted as $|0\rangle$ and $|1\rangle$, respectively. The generation of TFWM signal is usually understood through the perturbative interactions of three light pulses with the sample. In such a description, Pulse A creates a coherence between the $|0\rangle$ and $|1\rangle$ states. This coherence evolves with the frequency

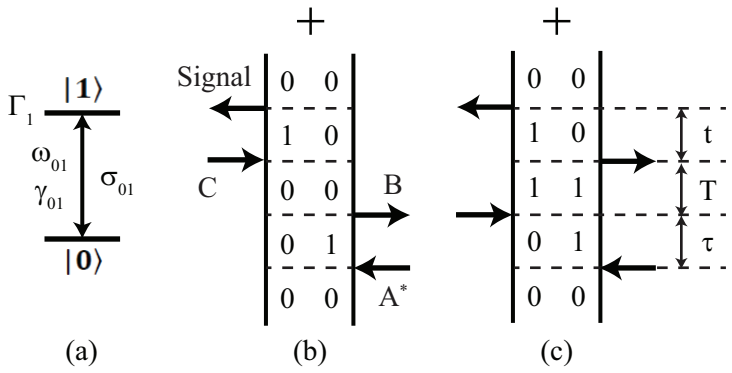

Figure 3.2: (a) A two-level system with ground $|0\rangle$ and excited $|1\rangle$ states. The resonance frequency ω_{01}, dephasing rate γ_{01}, and inhomogeneous width σ_{01} of the $|0\rangle \leftrightarrow |1\rangle$ transition is indicated. Γ_1 is the population decay rate of state $|1\rangle$. (b) and (c) show the double-sided Feynman diagrams that contribute to the TFWM signal. The pulse sequence is indicated in (b) and the relevant time delays are shown in (c). The + sign above the Feynman diagrams indicates the signal from the two diagrams are radiated in phase.

ω_{01} and decays with the dephasing rate γ_{01}. The sample interacts with pulse B after delay τ, which creates a spatial population grating depending on the relative phase between pulses A and B. Since the system is in a population state, there is no phase evolution during delay T. However, the grating decays due to population decay rate Γ_1 during this time delay. Pulse C is incident on the sample next; it puts the system in a coherent state again, which radiates the TFWM signal during time t. Because pulse A is conjugated, the phase evolution during τ is opposite to the phase evolution during t for the S_I time ordering. As a result, the decay of macroscopic polarization due to inhomogeneous broadening during τ is undone during t and signal is emitted as a photon echo at $t = \tau$. As a result, the S_I time ordering is also referred to as the rephasing or photon-echo time ordering. Since the effect of inhomogeneity is essentially eliminated, such an experiment can be used to measure the homogeneous dephasing rate even in the presence of inhomogeneous broadening.

The TFWM signal can be quantitatively calculated by solving the optical Bloch equations (OBEs). These are a set of coupled differential equations that relate the time evolution

of the density matrix elements

$$\rho = \begin{pmatrix} \rho_{00} & \rho_{01} \\ \rho_{10} & \rho_{11} \end{pmatrix} . \tag{3.4}$$

It is convenient to work in the rotating frame of the laser center-frequency and define the coherence ρ_{01} in terms of a slowly varying component $\widetilde{\rho}_{01}$ such that

$$\rho_{01} = \widetilde{\rho}_{01} \mathrm{e}^{i\omega t} \ . \tag{3.5}$$

ω is the center-frequency of the light. $\widetilde{\rho}_{10}$ and ρ_{10} are related through the complex conjugate of Eq. (3.5).

The OBEs for a two level system in the rotating wave-approximation are:

$$\begin{aligned} \dot{\widetilde{\rho}}_{01} &= (-\gamma_{01} + i\Delta_{01})\widetilde{\rho}_{01} + \frac{i}{2\hbar}\mu_{01}\mathcal{E}^*(2\rho_{11} - 1) \\ \dot{\rho}_{11} &= -\Gamma_1\rho_{11} + \frac{i}{2\hbar}\mu_{01}(\mathcal{E}\widetilde{\rho}_{01} - \mathcal{E}^*\widetilde{\rho}_{10}) \end{aligned} \tag{3.6}$$

where μ_{01} is the transition dipole moment of $|0\rangle \leftrightarrow |1\rangle$ transition, $\mathcal{E} = |E|\mathrm{e}^{i(\mathbf{k}\cdot\mathbf{r}-\omega t)}$ is the complex electric field of light, and $\Delta_{01} = \omega_{01} - \omega$ is the detuning of the transition energy with the light frequency. In case of pulsed light, ω is the center frequency of the laser spectrum. Only two equations are sufficient to completely define the density matrix evolution because $\rho_{10} = \rho_{01}^*$ and $\rho_{00} + \rho_{11} = 1$. These equations incorporate the light-matter interaction in the dipole approximation and excitation decays are included phenomenologically. An outline of the derivation from OBEs starting from the dipole approximation of the light-matter interaction is presented in Appendix A. The OBEs can be extended, in a straightforward manner, to more complicated energy level schemes following a similar procedure.

In general, the OBEs need to be solved numerically. However, an analytical solution can be obtained in the perturbative regime assuming δ-function pulses in time. This simplification implicitly assumes infinitely broad laser spectrum, which is not possible to realize experimentally. Nevertheless, this assumption is reasonable if the resonance is significantly

narrower than the laser spectrum. If that is not the case, the spectral dependence of amplitude will not be correctly reproduced through the simplified simulations, and will need ad-hoc adjustments. The detailed procedure for solving the OBEs using the aforementioned assumptions has been discussed previously [100], and will not be discussed in this work.

We will take an alternate, shorthand approach to calculate the TFWM signal using double-sided Feynman diagrams [38, 100]. In this method, the TFWM signal is separated into several quantum pathways, each represented by a Feynman diagram. Figures 3.2(b) and 3.2(c) show the Feynman diagrams that contribute to the TFWM signal for the S_I time ordering in the two-level system shown in Fig. 3.2(a). Interaction with each pulse and the radiation of TFWM signal is indicated by an arrow. The excitation pulses and the signal are labeled in Fig. 3.2(b). The relevant time delays are shown in Fig. 3.2(c). Without going into specific details, which are discussed elsewhere [100], the TFWM signal can be calculated by following the rules/properties of the Feynman diagrams:

- The numbers on each line indicate a specific density matrix element. For instant, the second row from the bottom in Fig. 3.2(b) indicates the density matrix element $|0\rangle\langle 1|$ or ρ_{01}.

- The interaction with each pulse takes the system from one density matrix element to another through optical transitions. For instance, pulse A takes the system from ρ_{00} to ρ_{01} through the $|0\rangle \leftrightarrow |1\rangle$ transition.

- For a particular Feynman diagram, it is assumed that, during a particular delay the system is in the state defined by the density matrix element during that delay as indicated in the Feynman diagram.

- Since pulse A is conjugated, the arrow indicating it is opposite to those indicating pulses B and C.

- An arrow pointing inwards creates an excitation in the system whereas an outward

pointing arrow results in relaxation.

- The system should be in a population state after the TFWM signal is radiated.
- The overall signal phase of a particular Feynman diagram is $(-1)^n$ where n is the number of interactions, including signal emission, on either the left or right side of the Feynman diagram.
- All possible Feynman diagrams have to be included to correctly calculate the TFWM signal.

Following these rules and properties, only two diagrams can be drawn for the S_I time ordering as shown in Figs. 3.2(b) and 3.2(c). Both these diagrams give rise to equal TFWM signals; the total radiated signal field can be written, in the rotating frame, as

$$S_{S_I,2level}(\tau,T,t) = 2|E|^3{\mu_{01}}^4 \mathrm{e}^{-i\Delta_{01}(\tau-t)}\mathrm{e}^{-(\gamma_{01}\tau+\Gamma_1 T+\gamma_{01}t)}\mathrm{e}^{-\frac{1}{2}{\sigma_{01}}^2(\tau-t)^2}\Theta(\tau)\Theta(T)\Theta(t) \qquad (3.7)$$

where all the variables have been previously defined and Θ denotes the Heaviside theta function to ensure the correct time ordering.

It is imperative to take a close look at the different factors in Eq. (3.7) in order to understand how it was obtained from the Feynman diagrams in Figs. 3.2(b) and 3.2(c):

- Both the Feynman diagrams comprise two interactions each on the left and right side, and, consequently, have the same phase. The factor of 2 accounts for the constructive interference between these two diagrams.
- The factor $|\mathrm{E}|^3$ is obtained by assuming equal electric field amplitude for all the excitation pulses, which is generally true for our experiment.
- There are four interactions involving the $|0\rangle \leftrightarrow |1\rangle$ transition, which are incorporated in the factor ${\mu_{01}}^4$.

- The first exponential term includes the oscillation of the signal with the resonance frequency, which corresponds to the detuning frequency in the rotating-wave approximation. The opposite sign for delays τ and t is due to the rephasing time ordering.

- The second exponential includes the homogeneous decays. The dephasing rate is relevant for delays τ and t because the system is in a coherent state during those intervals. During delay T the population decay rate is the relevant quantity since the system is in a population state. The population decay with T is included even for the Feynman diagram in Fig. 3.2(b), although the system is in the $|0\rangle$ state, to correctly account for the decay in the population grating, which determines the rate of decay of TFWM signal.

- The last term accounts for the inhomogeneous broadening in the system that results in the signal being emitted as a photon echo at $t = \tau$. A Gaussian lineshape for the inhomogeneous broadening is assumed. Inhomogeneity does not contribute to the decay during T when the system is in a population state, as long as no spectral diffusion occurs.

The above theoretical description of the origin of TFWM signal will be used extensively throughout this work to calculate 2D spectra. Before we get to the details of 2DCS, we will provide an overview of typical variations of TFWM experiments that have been used to study excitons in QWs. This will provide some context to the work presented later on and also highlight the advantages of 2DCS vis-à-vis TFWM experiments.

3.1.3 Experimental studies

In a typical TFWM experiment, one of the time delays, τ or T, is varied and the signal can either be resolved spectrally or temporally, or the time-integrated TFWM (TI-TFWM) signal can be measured by a slow photo-detector. The two-pulse TFWM experiment is more

widely used because of simpler experimental implementation. Theoretically, a two-pulse experiment can be treated similar to the three-pulse experiment discussed in Section 3.1.2, with pulses B and C incident on the sample simultaneously. In this case only delay τ can be scanned. We will now review some of the commonly used variations of the TFWM technique.

Photon echo spectroscopy: This realization uses the S_I or rephasing time-ordering and is most commonly used for its ability to extract the homogeneous response of a system even in the presence of inhomogeneity. Generally, the TI-TFWM is measured as a function of delay τ. As discussed earlier the effect of inhomogeneity on the macroscopic polarization is reversed. As a result, the homogeneous dephasing rate can be extracted, from the decay of TI-TFWM signal with delay τ, even in an inhomogeneously broadened spectrum. This scheme can also reveal coherent coupling between different states through oscillations in the TI-TFWM signal as a function of τ, although care needs to be taken to distinguish such oscillations from polarization interference [3, 101]. An interesting result was the observation of finite and fast-decaying TI-TFWM signal for negative values of τ, which seemed to violate causality and was shown to be due to local field effects [60, 6]. We will briefly discuss the origin of this signal in Section 3.2.5 from the perspective of interactions.

Three-pulse photon echo peak shift (3PEPS) spectroscopy: 3PEPS experiments have been used to study non-Markovian decay dynamics of coherences in various systems [36, 37, 102], including QWs [40]. The photon-echo takes some time to build up, and the TI-TFWM is maximum at some finite $\tau > 0$, say τ_m. In this experiment, τ_m is measured as a function of delay T. In the absence of spectral diffusion, the value of τ_m does not change with T. However, since the transition frequency for each oscillator changes with increasing T due to spectral diffusion, the generation of a photon-echo is not perfect. As a result, the system behaves more and more like a homogeneously broadened system with increasing T, and τ_m decreases, which is used to quantify spectral diffusion under certain approximations [39, 40].

With a brief background of non-linear spectroscopy in general and TFWM in par-

ticular, we will now discuss the principles of 2DCS from the theoretical and experimental perspectives.

3.2 Two-dimensional coherent spectroscopy – theory

2DCS is an extension of the time resolved TFWM technique, and requires phase-sensitive detection of signal and scanning of time delays. This poses several experimental challenges that will be discussed in Section 3.3. However, the theoretical description for 2DCS follows directly from that of TFWM discussed in Section 3.1.2; a numerical Fourier transform of the time-domain TFWM signal along delays τ or T and t results in a 2D spectrum. Nevertheless, this seemingly straightforward extension results in significant advantages of 2DCS compared to TFWM techniques because the TFWM signal is unfolded on to two frequency dimensions. Different kinds of 2D scans can be performed by changing the time-ordering of excitation pulses and/or the time delay that is scanned. These variations yield comprehensive information about the system under study. Through detailed analysis, one can quantify several physical properties of the system. However, the physical properties can easily be understood qualitatively by just looking at different 2D spectra. Presently, we will discuss the interpretation of different kinds of 2D spectra for various model systems that include few energy levels.

3.2.1 Rephasing one-quantum scan

The first kind of 2D scan that we will discuss is the most obvious extension of the photon-echo spectroscopy discussed in Section 3.1.3; the excitation pulses are incident on the sample in the S_I time-ordering [Fig. 3.1(a)] and the delay τ is scanned. The rephasing one-quantum 2D spectrum is obtained by taking a Fourier transform of Eq. (3.7) along delays τ and t. The name one-quantum is used because the system is in a superposition state, which evolves at the frequency of the transition between the ground and excited states during the scanned time delay τ. We will discuss this 2D spectrum for a two-level system

and a three-level V system.

Homogeneous broadening: First, we will consider a two-level system, as shown in Fig. 3.2(a), without any inhomogeneous broadening, i.e. $\sigma_{01} = 0$. The absolute value, real part, and imaginary part of the 2D signal are shown in Figs. 3.3(a), 3.3(b), and 3.3(c), respectively. We use $\Delta_{01} = 5$ meV, and $\gamma_{01} = 0.1$ meV. Γ_1 does not affect these spectra since T is kept constant for this scan.

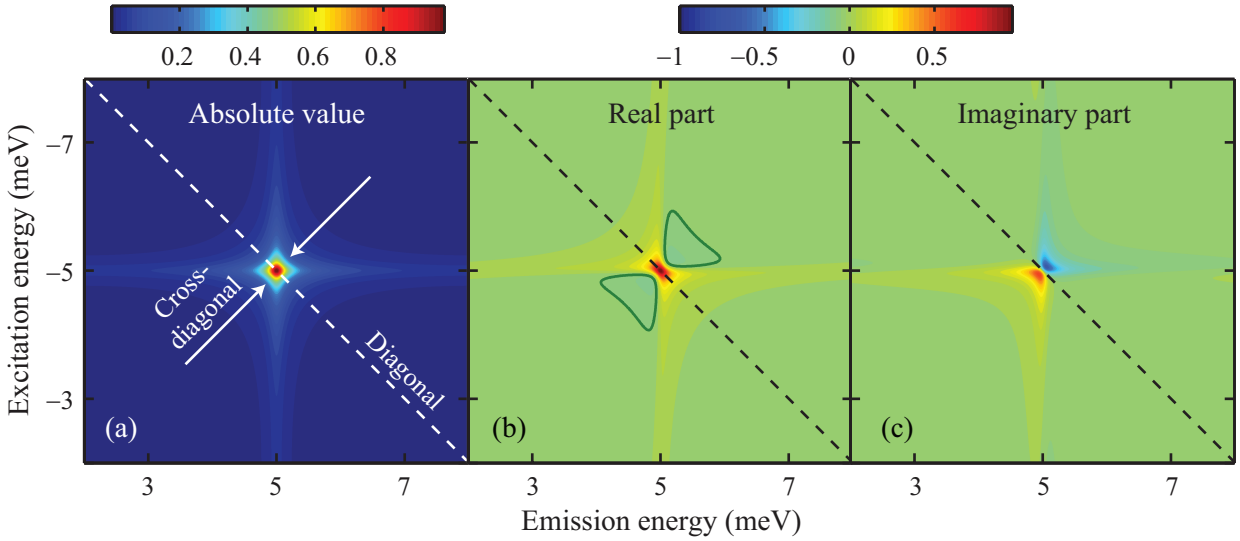

Figure 3.3: (a) Absolute value, (b) real part, and (c) imaginary part rephasing one-quantum 2D spectra for a homogeneously broadened two-level system. The dashed line in each spectrum indicated the diagonal direction. The cross-diagonal direction is indicated by arrows in (a). The negative value region is outlined in (b).

The horizontal energy axis is the $\hbar\omega_t$ axis, denotes the photon emission energy, and corresponds to the emission of the TFWM signal. This axis is labeled "emission energy". The vertical axis is labeled excitation energy and corresponds to $\hbar\omega_\tau$. The excitation energy axis is labeled with negative energies to indicate opposite phase evolution during delays τ and t; it is assumed that the radiated TFWM signal has positive frequency. Equal the emission and excitation energies with equal magnitudes are indicated by the dashed diagonal lines. The direction perpendicular to the diagonal direction is the cross-diagonal direction, as indicated by arrows in Fig. 3.3(a).

The absolute value spectrum in Fig. 3.3(a) shows a star-shaped peak on the diagonal line at the detuning energy used in the simulation. The real part spectrum in Fig. 3.3(b) has a positive peak with slight negative values in the wings, and is outlined. This feature results from the discrete Fourier transform of the Heaviside theta functions, $\Theta(\tau)$ and $\Theta(t)$, in Eq. (3.7), and is referred to as the phase-twist in the spectrum [103]. This phase twist also results in a broadening of the peak in the real part spectrum. Both these issues can be resolved through the correlation spectrum [103], as will be shown in Section 3.2.4.

Effect of inhomogeneous broadening: The 2D spectrum is modified significantly in the presence of inhomogeneity. Figures 3.4(a) and 3.4(b) show rephasing one-quantum absolute value spectra for $\sigma_{01} = 0.2$ and 1 meV, respectively. The other system parameters are kept the same as earlier. The signal from different frequency groups appears along the diagonal line resulting in an elongated peak in the 2D spectrum. This elongation increases with an increase in the inhomogeneity in the sample.

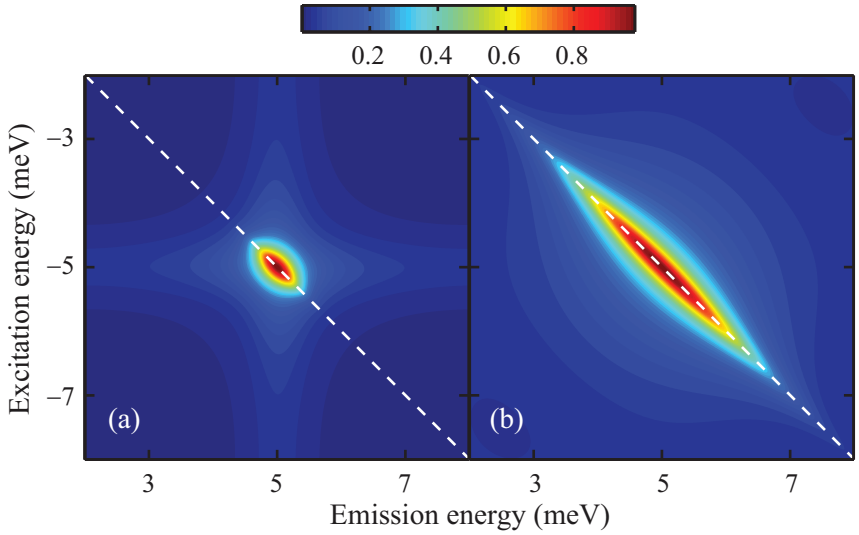

Figure 3.4: Rephasing one-quantum spectrum with (a) $\sigma_{01} = 0.2$ meV and (b) $\sigma_{01} = 1$ meV. Other parameters are the same as those used to simulate the spectra shown in Fig. 3.3. Inhomogeneity results in an elongation of the peak along the diagonal direction.

The width of slices taken along the diagonal and cross-diagonal directions generally correspond to the inhomogeneous and homogeneous linewidths. This situation is strictly

true for extreme inhomogeneity, similar to the case in Fig. 3.4(b). For an intermediate case, as shown in Fig.3.4(a), the diagonal and cross-diagonal slices can be simultaneously fit to complex lineshapes to obtain the homogeneous and inhomogeneous linewidths [104]. We made an assumption that the dephasing rate does not depend on the resonance energy to obtain Eq. (3.7). However, this assumption is not always valid, which results in varying cross-diagonal width across the inhomogeneous distribution. This spectral dependence can be measured using a single 2DCS experiment [11] as opposed to spectrally averaged information that is obtained from TI-TFWM experiments.

Coherent coupling: 2DCS is an ideal technique to study coherent coupling between different eigenstates of a system. We will illustrate the effect of coupling on a rephasing one-quantum 2D spectrum using a three-level V system shown in Fig. 3.5 with ground state $|0\rangle$ and excited states $|1\rangle$ and $|2\rangle$. The transitions $|0\rangle \leftrightarrow |1\rangle$ and $|0\rangle \leftrightarrow |2\rangle$ are the only optically allowed transitions. The excited states are, however, coupled through the ground state. As was done previously, all the parameters for these transitions are indicated.

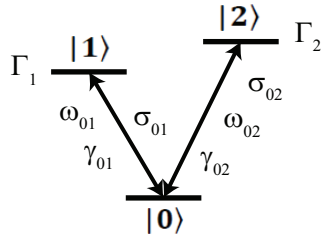

Figure 3.5: Three-level system with the ground state $|0\rangle$ and two excited states $|1\rangle$ and $|2\rangle$. The resonance frequency ω, dephasing rate γ and inhomogeneity σ of the $|0\rangle \leftrightarrow |1\rangle$ and $|0\rangle \leftrightarrow |2\rangle$ transitions are indicated. The population decay rates Γ for the excited states are also indicated.

Feynman diagrams similar to those in Fig. 3.2 can be written down with interactions involving only one of $|0\rangle \leftrightarrow |1\rangle$ and $|0\rangle \leftrightarrow |2\rangle$ transitions. Each of these diagrams includes interactions in both $|0\rangle \leftrightarrow |1\rangle$ and $|0\rangle \leftrightarrow |2\rangle$ transitions. In addition to these diagrams, the Feynman diagrams shown in Fig. 3.6 also contribute to the TFWM signal. All these

diagrams have the same phase and the total TFWM signal can be written as

$$
\begin{aligned}
S_{S_I,3level}(\tau,T,t) =& |E|^3 \Big[2{\mu_{01}}^4 \mathrm{e}^{-i\Delta_{01}(\tau-t)} \mathrm{e}^{-(\gamma_{01}\tau+\Gamma_1 T+\gamma_{01}t)} \mathrm{e}^{-\frac{1}{2}\sigma_{01}^2(\tau-t)^2} + 2{\mu_{02}}^4 \mathrm{e}^{-i\Delta_{02}(\tau-t)} \\
& \mathrm{e}^{-(\gamma_{02}\tau+\Gamma_2 T+\gamma_{02}t)} \mathrm{e}^{-\frac{1}{2}{\sigma_{02}}^2(\tau-t)^2} + {\mu_{01}}^2{\mu_{02}}^2 \mathrm{e}^{-i(\Delta_{01}\tau-\Delta_{02}t)} \mathrm{e}^{-(\gamma_{01}\tau+\gamma_{02}t)} \\
& \mathrm{e}^{-\frac{1}{2}(\sigma_{01}\tau-\sigma_{02}t)^2} \left(\mathrm{e}^{-\Gamma_1 T} + \underline{\mathrm{e}^{i\Delta_{21}T} \mathrm{e}^{-\gamma_{12}T} \mathrm{e}^{-\frac{1}{2}{\sigma_{12}}^2 T^2}} \right) + \\
& {\mu_{01}}^2{\mu_{02}}^2 \mathrm{e}^{-i(\Delta_{02}\tau-\Delta_{01}t)} \mathrm{e}^{-(\gamma_{02}\tau+\gamma_{01}t)} \mathrm{e}^{-\frac{1}{2}(\sigma_{02}\tau-\sigma_{01}t)^2} \\
& \left(\mathrm{e}^{-\Gamma_2 T} + \underline{\mathrm{e}^{i\Delta_{12}T} \mathrm{e}^{-\gamma_{12}T} \mathrm{e}^{-\frac{1}{2}{\sigma_{12}}^2 T^2}} \right) \Big] \Theta(\tau)\Theta(T)\Theta(t).
\end{aligned}
\tag{3.8}
$$

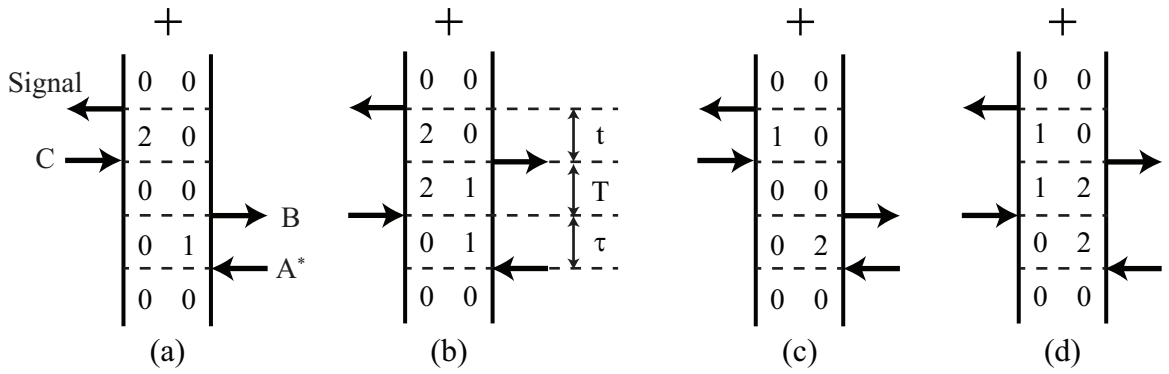

Figure 3.6: Feynman diagrams that contribute to the four-wave mixing signal due to coherent coupling between the $|0\rangle \leftrightarrow |1\rangle$ and $|0\rangle \leftrightarrow |2\rangle$ transitions. The pulse sequence is indicated in (a) and the relevant time delays are shown in (b). The signal due to all the Feynman diagrams have the same phase, as indicated by the + sign above each diagram.

The first and second terms include signals from the Feynman diagrams similar to those in Fig. 3.2 for the $|0\rangle \leftrightarrow |1\rangle$ and $|0\rangle \leftrightarrow |2\rangle$ transitions, respectively. The other two terms include contribution from the Feynman diagrams shown in Fig. 3.6, and involve two interactions each with the two transitions, which is accounted for by the factor ${\mu_{01}}^2{\mu_{02}}^2$. The Feynman diagrams in Fig. 3.6 have different evolution frequencies during delays τ and t. The third term includes contributions from the Feynman diagrams shown in Figs. 3.6(a) and 3.6(b) while the signal due to the Feynman diagrams in Figs. 3.6(c) and 3.6(d) is incorporated in the fourth term. These terms include new parameters to correctly describe the change in the TFWM signal with T. These parameters are defined in Sec. 3.2.2 along with the discussion of change in TFWM signal with T.

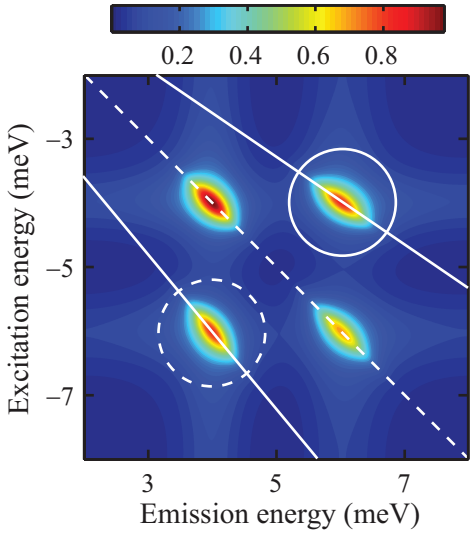

Figure 3.7: Rephasing one-quantum absolute value 2D spectrum for the three-level system in Fig. 3.5. The off-diagonal peaks are circled, and indicate coherent coupling between states $|1\rangle$ and $|2\rangle$. Note the tilt of the off-diagonal peaks with respect to the diagonal line, as indicated by the lines through the peak, due to different inhomogeneity of the $|0\rangle \leftrightarrow |1\rangle$ and $|0\rangle \leftrightarrow |2\rangle$ transitions.

Figure 3.7 shows the simulated rephasing one-quantum absolute value 2D spectrum obtained from Eq. (3.8) using the following parameter values: $\Delta_{01} = 4$ meV, $\Delta_{02} = 6$ meV, $\gamma_{01} = \gamma_{02} = 0.1$ meV, $\sigma_{01} = 0.2$ meV, $\sigma_{02} = 0.25$ meV, and $\mu_{02}/\mu_{01} = 0.95$. There are several key features of this spectrum, which we would like to highlight:

- The diagonal peaks result from the first two terms in Eq. (3.8), and results from all light-matter interactions involving only a single transition.

- Coherent coupling between states $|1\rangle$ and $|2\rangle$ results in the circled off-diagonal peaks. Feynman diagrams in Figs. 3.6(a) and 3.6(b) result in the above-diagonal peak, which is circled by a solid line. The Feynman diagrams in Figs. 3.6(c) and 3.6(d) give rise to the peak below the diagonal line, which is circled by a dashed line.

- The peak strength of the coupling peaks are equal to the geometric mean of the peak strength of the peaks on the diagonal.

- The solid line through the off-diagonal peaks indicate the tilt of these peaks with respect to the diagonal line due to the different, but correlated inhomogeneous linewidths of the $|0\rangle \leftrightarrow |1\rangle$ and $|0\rangle \leftrightarrow |2\rangle$ transitions. Uncorrelated inhomogeneities of the two transitions will result in circular, instead of elongated, peaks.

The appearance of off-diagonal coupling peaks makes 2DCS extremely useful to study such systems. While coherent coupling can be interpreted from beating in TI-TFWM with τ, one needs to be careful to distinguish between quantum and polarization beats [3, 101]. Furthermore, we can identify the correlation between inhomogeneities of different states through the peak shape from such a 2D spectrum. Next we will discuss a 2D scan which also uses the S_I time-ordering, but involves scanning time delay T instead of τ.

3.2.2 Rephasing zero-quantum scan

As mentioned earlier, for a two-level system, a spatial population grating exists during delay T, and there is not phase evolution during this time delay. Thus, information about the population decay times can be obtained by measuring TFWM signal as delay T is scanned. However, a Raman-like non-radiative coherence between two excited states exists during T as shown in the Feynman diagrams in Figs. 3.6(b) and (d) for a three-level system. The TFWM signal phase evolves with T at a frequency that is much smaller compared to the transition frequency and this scan is known as zero-quantum scan. We will look at typical spectra for this scan for both two- and three-level systems.

Population decay rate: A rephasing zero-quantum absolute value 2D spectrum for an inhomogeneously broadened system is shown in Fig. 3.8(a). This spectrum was obtained by taking a numerical Fourier transform of Eq. (3.7) along time delays T and t. The system parameters were the same as those used to obtain the rephasing one-quantum spectrum shown in Fig. 3.4(b). The population decay rate $\Gamma_1 = 0.2$ meV was used, which satisfies Eq. (2.12) and assumes no pure dephasing processes.

The vertical axis is labeled mixing energy and corresponds to ω_T; zero mixing energy is denoted by the dashed line. Since the system is in a population state during T, the single peak appears on the zero mixing energy line. The peak is elongated along the emission energy axis due to the inhomogeneous broadening. The peak-width along the mixing energy axis, as indicated by the vertical line, gives the population decay rate.

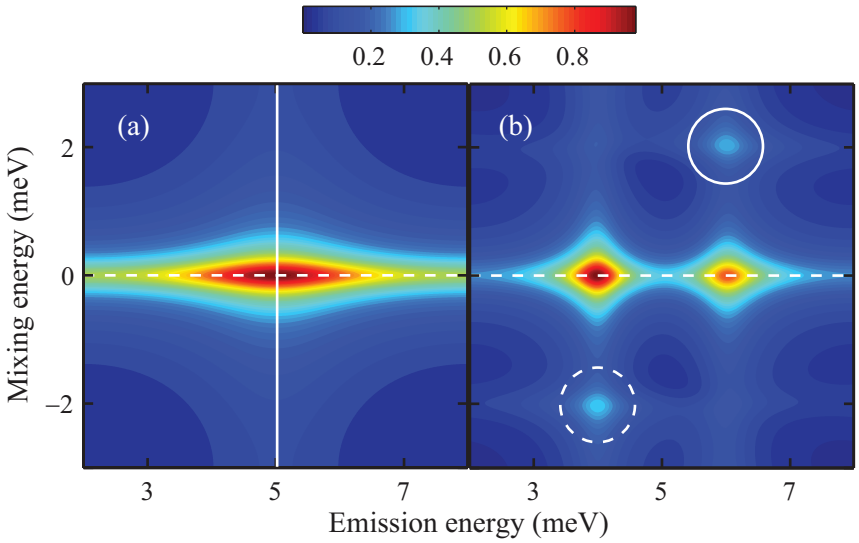

Figure 3.8: Zero-quantum rephasing absolute value 2D spectrum for (a) two-level system shown in Fig. 3.1(b) and (b) three-level V system shown in Fig. 3.5. The elongation of peaks along the emission energy axis is due to inhomogeneity. The width of the vertical slice indicated gives the population decay rate of the exciton. The circled peaks with non-zero mixing energy in (b) result from coherent coupling between states $|1\rangle$ and $|2\rangle$.

Coherent coupling: Similar to the one-quantum spectrum, coherent coupling between states has apparent signature in zero-quantum scan as shown by the spectrum in Fig. 3.8(b). The system parameters are the same as the ones used to obtain the spectrum in Fig. 3.7. The population decay rates $\Gamma_1 = \Gamma_2 = 0.2$ meV were used consistent with no pure dephasing processes.

The most interesting feature in this spectrum is the presence of the circled peaks at non-zero mixing energy obtained due to the coherent coupling between states $|1\rangle$ and $|2\rangle$. The Feynman diagrams in Figs. 3.6(b) and 3.6(d) contribute to the peaks circled with

solid and dashed lines, respectively. In these Feynman diagrams, a non-radiative coherence between states $|1\rangle$ and $|2\rangle$ exists, which results in coupling peaks at mixing energies equal to the difference in the transition energies of $|0\rangle \leftrightarrow |1\rangle$ and $|0\rangle \leftrightarrow |2\rangle$ transitions.

Further insight into the coupling is gained through the terms that are underlined in Eq. (3.8), which result in the coupling peaks. We should first define the new parameters used. $\Delta_{21} = -\Delta_{12} = \omega_{02} - \omega_{01} = 2$ meV give the resonance energies of the non-radiative coherences between states $|1\rangle$ and $|2\rangle$, $\gamma_{12} = \gamma_{01} + \gamma_{02} = 0.2$ meV is the dephasing rate of this coherence, and $\sigma_{12} = |\sigma_{01} - \sigma_{02}| = 0.05$ meV is the corresponding inhomogeneity, assuming correlated inhomogeneity between states $|1\rangle$ and $|2\rangle$. It is worth noting that both γ_{12} and σ_{12} contribute to the signal decay with T resulting in coupling peaks that appear circular, instead of elongated. Furthermore, only a single Feynman diagram contributes to each coupling peak compared to three Feynman diagrams that contribute to the peaks with zero mixing energy, which results in the significant difference in the amplitudes of these peaks. Finally, we would like to note that while the coupling peaks in a one-quantum spectrum might appear due to population transfer, during T, between the different states, the coupling peaks in zero-quantum only show up in the presence of coherent coupling.

All the 2DCS experimental results presented in this work have been obtained for the S_I time ordering. However, for the sake of completeness, we will discuss other time orderings and the corresponding 2D spectra.

3.2.3 Non-rephasing one-quantum scan

The non-rephasing one-quantum scan is similar to its rephasing version. The only difference is that pulse B is incident on the sample first followed by pulse A, as shown in Fig. 3.9(a). Since the conjugate pulse is the second pulse that is incident on the sample, this time ordering is referred as the S_{II} time ordering. The phase evolution during τ and t are the same, which prevents the formation of a photon-echo even in the presence of inhomogeneity.

The Feynman diagrams that contribute to the TFWM signal in the two-level system

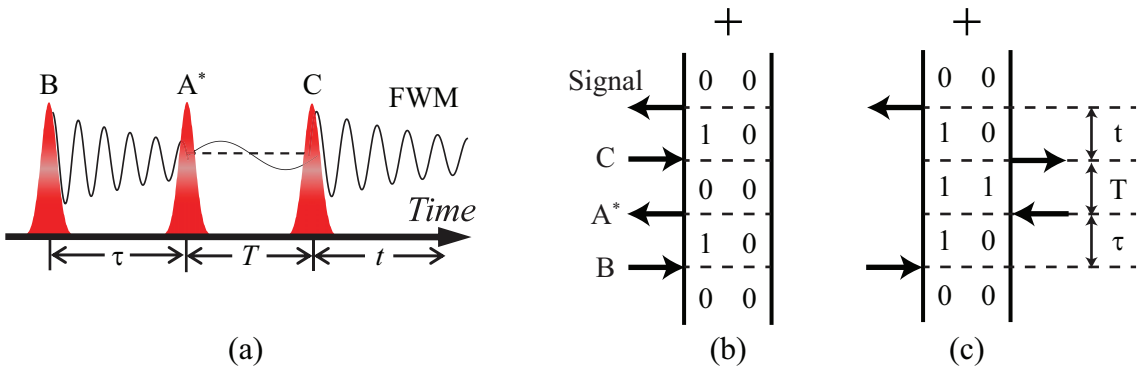

Figure 3.9: (a) The non-rephasing one-quantum time ordering. (b) The Feynman diagrams that contribute to the four-wave mixing signal for this time-ordering. The pulse sequence is indicated in (b) and the relevant time delays are shown in (c).

shown in Fig. 3.2(a) for this time ordering are shown in Figs. 3.9(b) and 3.9(c). The corresponding TFWM signal can be written as

$$S_{S_{II},2level}(\tau,T,t) = 2|E|^3{\mu_{01}}^4 e^{i\Delta_{01}(\tau+t)} e^{-(\gamma_{01}\tau+\Gamma_1 T+\gamma_{01}t)} e^{-\frac{1}{2}{\sigma_{01}}^2(\tau+t)^2}\Theta(\tau)\Theta(T)\Theta(t) \qquad (3.9)$$

where all the variables have their usual meaning. Equations (3.9) and (3.7) are almost identical with a couple of differences – (1) the first exponential denotes similar phase evolution during delays τ and t, and (2) $(\tau+t)^2$ in the last exponential accounts for the fact the signal is not emitted as a photon-echo even in the presence of inhomogeneity.

Figures 3.10(a), 3.10(b), and 3.10(c) show the absolute value, real part and imaginary part non-rephasing one-quantum 2D spectrum, respectively for a two-level system in the absence of inhomogeneous broadening. The system parameters are the same as used for the spectra in Fig. 3.3. Equations (3.9) and (3.7) are essentially identical for $\sigma_{01} = 0$; the only difference is that positive frequency during both delays τ and t. This is reflected in the identical peak shapes in 2D spectra in Figs. 3.3 and 3.10. An important distinction, however, is that the excitation energy axis has positive values for the non-rephasing spectra.

The one-quantum 2D spectra for S_I and S_{II} time orderings differ significantly in the presence of inhomogeneity. Due to the lack of rephasing, the peaks are uniformly broadened along the diagonal and cross-diagonal directions as a result of inhomogeneous broadening.

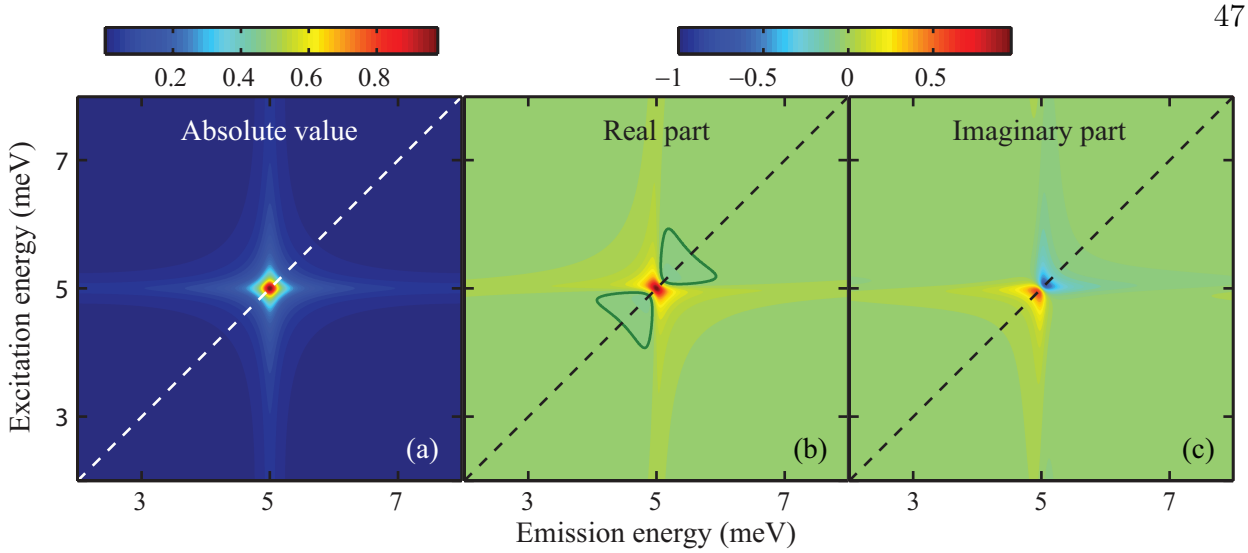

Figure 3.10: (a) Absolute value, (b) real part, and (c) imaginary part one-quantum non-rephasing 2D spectra for a homogeneously broadened two-level system. The negative value region is outlined in (b).

Coupling peaks, for the three-level system in Fig. 3.5, appear in a non-rephasing spectrum too, similar to those for the rephasing spectrum in Fig. 3.7. Since, both rephasing and non-rephasing one-quantum spectra give similar information, the non-rephasing spectra are generally used to measure correlation spectrum, which we will discuss next.

3.2.4 Correlation spectrum

Both the rephasing and non-rephasing one-quantum spectrum show effects of phase-twist due to the Heaviside theta functions in Eqs. (3.7) and (3.9). This phase-twist results in the broadening of the peak in the real part spectrum. It also results in the negative values in the real part spectrum, although the time domain signal is strictly positive if $\Delta_{01} = 0$. These anomalies can be resolved by adding the rephasing and non-rephasing spectra to obtain the correlation spectrum. Mathematically a one-quantum correlation spectrum is related to the rephasing and non-rephasing spectra as

$$S_{Cor,2level}(\omega_\tau, T, \omega_t) = S_{S_I,2level}(|\omega_\tau|, T, \omega_t) + S_{S_{II},2level}(\omega_\tau, T, \omega_t) \tag{3.10}$$

where all the signals are written in the 2D frequency domain.

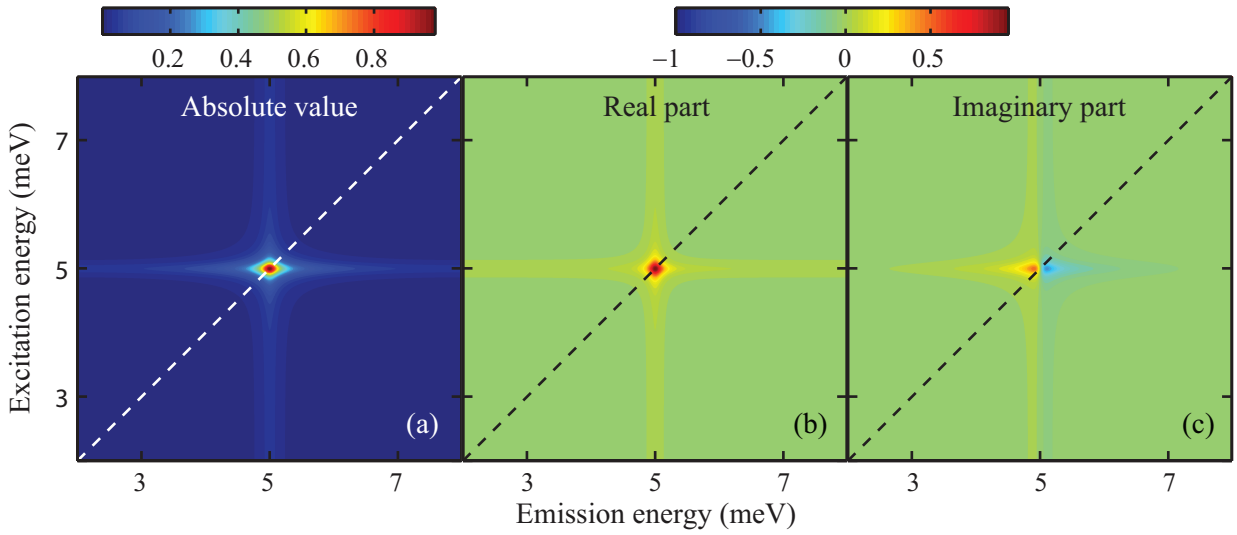

Figure 3.11: (a) Absolute value, (b) real part, and (c) imaginary part one-quantum correlation 2D spectra for a homogeneously broadened two-level system. Note that the peak in (b) has only positive values and is narrower compared to the one-quantum rephasing and non-rephasing spectra shown in Figs. 3.3(b) and 3.10(b), respectively.

The correlation spectra obtained from the 2D spectra in Figs. 3.3 and 3.10 are shown in Fig. 3.11. The real part spectrum in Fig. 3.11(b) does not have any negative value and is also much narrower than the peak in Figs. 3.3(b) and 3.10(b). As a result, measuring a correlation spectrum is especially useful in molecular systems where several partially overlapping resonances can be more easily identified due to the narrow peaks [103].

3.2.5 Two-quantum scan

Finally, we will discuss TFWM signal originating when the excitation pulses are incident on the sample in the S_{III} time-ordering, shown in Fig. 3.12, in which the conjugate pulse A is the last pulse that is incident on the sample. These scans are equivalent to the negative τ scans in two-pulse TFWM experiments mentioned in Section 3.1.3. While it was initially explained using the local field effects [60, 6], we will describe the origin of TFWM signal for this time ordering from the perspective of coherent interactions between multiple

excitations.

Single resonance: We need a three-level ladder system, as shown in Fig. 3.13(a), to obtain signal for this time ordering. This level scheme is different than the V system in Fig. 3.5 in that the transition $|1\rangle \leftrightarrow |2\rangle$ is optically allowed while $|0\rangle \leftrightarrow |2\rangle$ is not. Also, this transition has a resonance energy that is close to that of $|0\rangle \leftrightarrow |1\rangle$ transition. The Feynman diagrams that contribute to the TFWM signal are shown in Fig. 3.13(b) and (c). Both these diagrams indicate that the system is in the non-radiative $|0\rangle \leftrightarrow |2\rangle$ coherence during T. This coherence cannot be created in a two-level system, thus resulting in the absence of TFWM signal for such a system.

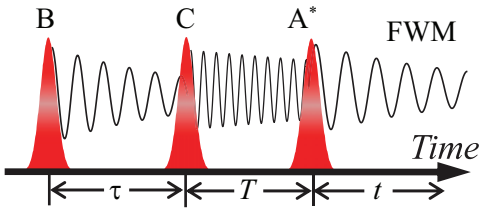

Figure 3.12: The S_{III} or double-quantum time ordering with the conjugate pulse A* incident last on the sample. Note that the phase evolution during T is twice as fast as that during τ and t.

The $|0\rangle \leftrightarrow |2\rangle$ coherence during delay T evolves at a rate that is faster and close to twice the rate of evolution of the $|0\rangle \leftrightarrow |1\rangle$ coherence during delay τ, as indicated in Fig. 3.12. Since the delay T is scanned, this scan is called a two-quantum scan. The two Feynman diagrams in Fig. 3.13 have opposite signs, which results in destructive interference between the TFWM signal from these diagrams. As a result, the total TFWM signal would be zero if the transitions $|0\rangle \leftrightarrow |1\rangle$ and $|1\rangle \leftrightarrow |2\rangle$ are identical. This symmetry can be broken if the resonance energy, the dephasing rate, and/or the dipole moment of $|1\rangle \leftrightarrow |2\rangle$ transition is different from those for the $|0\rangle \leftrightarrow |1\rangle$ transition, which gives rise to finite TFWM signal. In the energy-level scheme in Fig. 3.13(a), the resonance energy and dephasing rate of the $|1\rangle \leftrightarrow |2\rangle$ transition is greater than those of the $|0\rangle \leftrightarrow |1\rangle$ transition by ω' and γ', respectively. It is important to realize that state here $|2\rangle$ may indicate correlation between two excitations

in state $|1\rangle$. The correlation exists due to interactions between multiple excitations. Thus, including state $|2\rangle$ models the interactions between multiple excitations [63, 94].

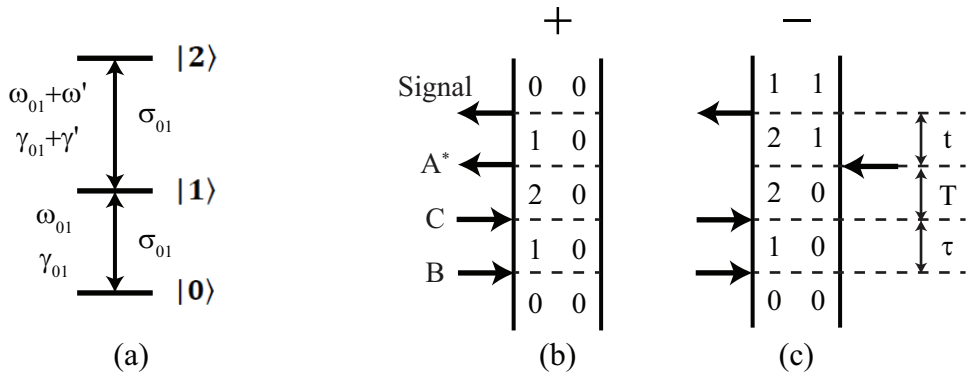

Figure 3.13: (a) Three level ladder system. (b) and (c) shown the Feynman diagrams that contribute to the signal in the S_{III} time-ordering. The pulse sequence is indicated in (b) and the relevant time delays are shown in (c). The two diagrams destructively interfere indicated by the + and − signs above the Feynman diagrams in (b) and (c), respectively. The broken symmetry between the $|0\rangle \leftrightarrow |1\rangle$ and $|1\rangle \leftrightarrow |2\rangle$ transitions, due to different resonance energies and/or dephasing rates, results in a finite four-wave mixing signal.

The TFWM signal arising from the Feynman diagrams in Fig. 3.13 can be written as

$$\begin{aligned} S_{S_{III},3level}(\tau,T,t) =& |E|^3 {\mu_{01}}^2 {\mu_{12}}^2 \mathrm{e}^{i(\Delta_{01}\tau+\Delta_{02}T)} \mathrm{e}^{-(\gamma_{01}\tau+\gamma_{02}T)} \mathrm{e}^{-\frac{1}{2}(\sigma_{01}\tau+\sigma_{02}T+\sigma_{01}t)^2} \\ & \left(\mathrm{e}^{i\Delta_{01}t}\mathrm{e}^{-\gamma_{01}t} - \mathrm{e}^{i\Delta_{12}t}\mathrm{e}^{-\gamma_{12}t}\right) \Theta(\tau)\Theta(T)\Theta(t) \end{aligned} \tag{3.11}$$

where the usual meaning of variables is used along with subscripts 01, 02 and 12 denoting transitions $|0\rangle \leftrightarrow |1\rangle$, $|0\rangle \leftrightarrow |2\rangle$, and $|1\rangle \leftrightarrow |2\rangle$, respectively. The parameters of these three transitions are related:

$$\begin{aligned} \omega_{12} &= \omega_{01} + \omega' & \omega_{02} &= \omega_{01} + \omega_{12} = 2\omega_{01} + \omega' \\ \gamma_{12} &= \gamma_{01} + \gamma' & \gamma_{02} &= \gamma_{01} + \gamma_{12} = 2\gamma_{01} + \gamma' \\ \sigma_{12} &= \sigma_{01} & \sigma_{02} &= \sigma_{01} + \sigma_{12} = 2\sigma_{02} \\ \mu_{12} &= \mu_{01} & \Delta_{02} &= \omega_{02} - 2\omega = 2\Delta_{01} + \omega' \end{aligned} \tag{3.12}$$

The relations in Eq. (3.12) can be used to simplify Eq. (3.11) and obtain

$$\begin{aligned} S_{S_{III},3level}(\tau,T,t) =& |E|^3 {\mu_{01}}^4 \mathrm{e}^{i\Delta_{01}(\tau+2T+t)} \mathrm{e}^{-\gamma_{01}(\tau+2T+t)} \mathrm{e}^{-\frac{1}{2}{\sigma_{01}}^2(\tau+2T+t)^2} \mathrm{e}^{(i\omega'-\gamma')T} \\ & \left[1 - \mathrm{e}^{(i\omega'-\gamma')t}\right] \Theta(\tau)\Theta(T)\Theta(t). \end{aligned} \tag{3.13}$$

The first and second terms in Eq. (3.13) correspond to the Feynman diagrams shown in Fig. 3.13(b) and 3.13(c), respectively. It is apparent from Eq. (3.13) that the TFWM signal will be non-zero if and only if ω' and/or γ' are non-zero.

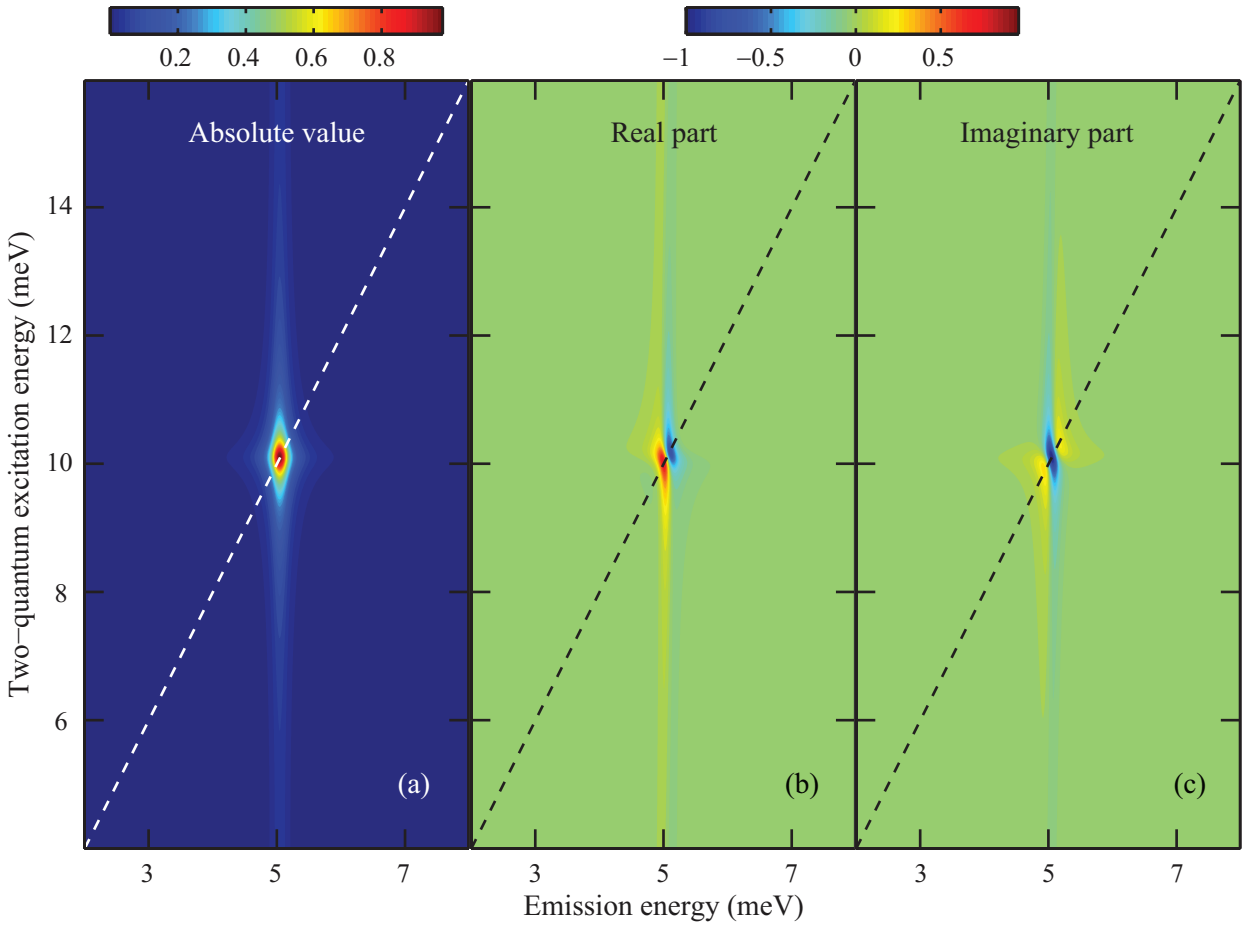

Figure 3.14: (a) Absolute value, (b) real part, and (c) imaginary part two-quantum 2D spectra for a homogeneously broadened two-level system. The peak in (b) comprises positive and negative peaks originating from Feynman diagrams in Fig. 3.13(b) and (c), respectively.

Figures 3.14(a), 3.14(b), and 3.14(c) show the simulated two-quantum absolute value, real and imaginary parts 2D spectra, respectively, for a homogeneously broadened system by taking a numerical Fourier transform of Eq. (3.13) along delays T and t. Similar to earlier values, we chose $\gamma_{01} = 0.1$ meV and $\Delta_{01} = 5$ meV. We set the symmetry breaking parameters as: $\gamma' = 0.01$ meV and $\omega' = 0.1$ meV. The vertical axis for these spectra is called the two-quantum excitation energy and corresponds to ω_T. $\omega_T = 2\omega_t$ is indicated by

a dashed diagonal line. The absolute value spectrum in Fig. 3.14(a) shows a single peak on the diagonal line corresponding to $\omega_t = \Delta_{01}$. The real part spectrum in Fig. 3.14(b) reveals that the peak in the absolute value spectrum arises from two peaks that are out of phase and very close to each other. The positive and negative peaks in Fig. 3.14(b) result from the first and second terms in Eq. (3.13), respectively, and are shifted along the emission energy axis by ω'. Next we will discuss how the presence of multiple coupled resonances is revealed in non-rephasing two-quantum spectrum.

Coherent coupling: The coupled states in the three-level V system shown in Fig. 3.5 does not result in any TFWM signal for the S_{III} time-ordering due to the same reason that results in no signal from a two-level system. Thus, we will discuss coupling between multiple resonances through the six-level system in Fig. 3.15. The various transitions and their parameters are very similar to those used previously, and is indicated in the figure. A similar system has been used to model interactions in various excitonic systems [105, 106]. The doubly excited states are now labeled $|11\rangle$, $|12\rangle$, and $|22\rangle$. The states $|11\rangle$ and $|22\rangle$ denote two correlated excitations in the states $|1\rangle$ and $|2\rangle$, respectively. Similarly, the state $|12\rangle$ represents excitations in states $|1\rangle$ and $|2\rangle$, which are correlated.

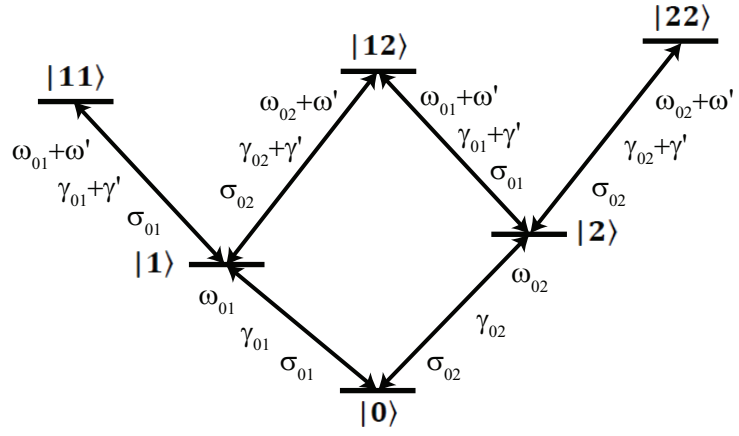

Figure 3.15: The six-level system originating from interactions between two three-level ladder systems similar to one shown in Fig. 3.13(a). The resonance energy ω, dephasing rate γ, and inhomogeneity σ are indicated for each transition.

As a result, the coherent coupling between states $|1\rangle$ and $|2\rangle$ involves the state $|12\rangle$ and contributes to the TFWM signal through Feynman diagrams shown in Figs. 3.16(a) – (d). These diagrams include the first and second interactions at energies close to $\hbar\omega_{01}$ and $\hbar\omega_{02}$, respectively. An alternate set of Feynman diagrams exist with these two interactions swapped. These two sets of diagrams are identical for $\tau = 0$; we will make this assumption for the sake of simplicity. In addition to the terms involving the $|12\rangle$ state, other Feynman diagrams similar to those in Fig. 3.13 also contribute to the TFWM signal, which can be written as

$$\begin{aligned} S_{S_{III},6level}(T,t) =& |E|^3 \mathrm{e}^{(i\omega'-\gamma')T}\left(1-\mathrm{e}^{(i\omega'-\gamma')t}\right)\Big[{\mu_{01}}^4 \mathrm{e}^{(i\Delta_{01}-\gamma_{01})(2T+t)}\mathrm{e}^{-\frac{1}{2}{\sigma_{01}}^2(2T+t)^2} + \\ & {\mu_{02}}^4 \mathrm{e}^{(i\Delta_{02}-\gamma_{02})(2T+t)}\mathrm{e}^{-\frac{1}{2}{\sigma_{02}}^2(2T+t)^2} + 2{\mu_{01}}^2{\mu_{02}}^2 \mathrm{e}^{i(\Delta_{01}+\Delta_{02})T} \\ & \mathrm{e}^{-(\gamma_{01}+\gamma_{02})T}\Big\{\mathrm{e}^{(i\Delta_{01}-\gamma_{01})t}\mathrm{e}^{-\frac{1}{2}[(\sigma_{01}+\sigma_{02})T+\sigma_{01}t]^2} + \mathrm{e}^{(i\Delta_{02}-\gamma_{02})t} \\ & \mathrm{e}^{-\frac{1}{2}[(\sigma_{01}+\sigma_{02})T+\sigma_{02}t]^2}\Big\}\Big]\,\Theta(\tau)\Theta(T)\Theta(t). \end{aligned} \tag{3.14}$$

The non-rephasing two-quantum absolute value 2D spectrum corresponding to the TFWM signal in Eq. (3.14) is shown in Fig. 3.16(e). We have used $\Delta_{01} = 4$ meV, $\Delta_{02} = 6$ meV, $\gamma_{01} = \gamma_{02} = 0.1$ meV, $\omega' = 0.1$ meV, $\gamma' = 0.01$ meV, and $\mu_{02}/\mu_{01} = 0.95$. The first two terms in the square brackets in Eq. (3.14) result in the two peaks on the diagonal line. The rest of the terms give rise to the circled coupling peaks, which appear shifted from the diagonal. Feynman diagrams in Figs. 3.16(a) and 3.16(b) result in the peak circled with dashed line and those in Figs. 3.16(c) and 3.16(d) give rise to the peak circled with solid line. Both coupling peaks have two-quantum excitation energy $= \Delta_{01} + \Delta_{02} + \omega' \approx \Delta_{01} + \Delta_{02}$. These peaks are more intense than the peaks on the diagonal because more Feynman diagrams contribute to these peaks.

It is important to note that for the S_{III} time-ordering the system is never in a population state. As a result, the signal originates entirely from interaction and/or coherent coupling between states. Thus, the two-quantum scans are extremely useful for studying coherent interactions.

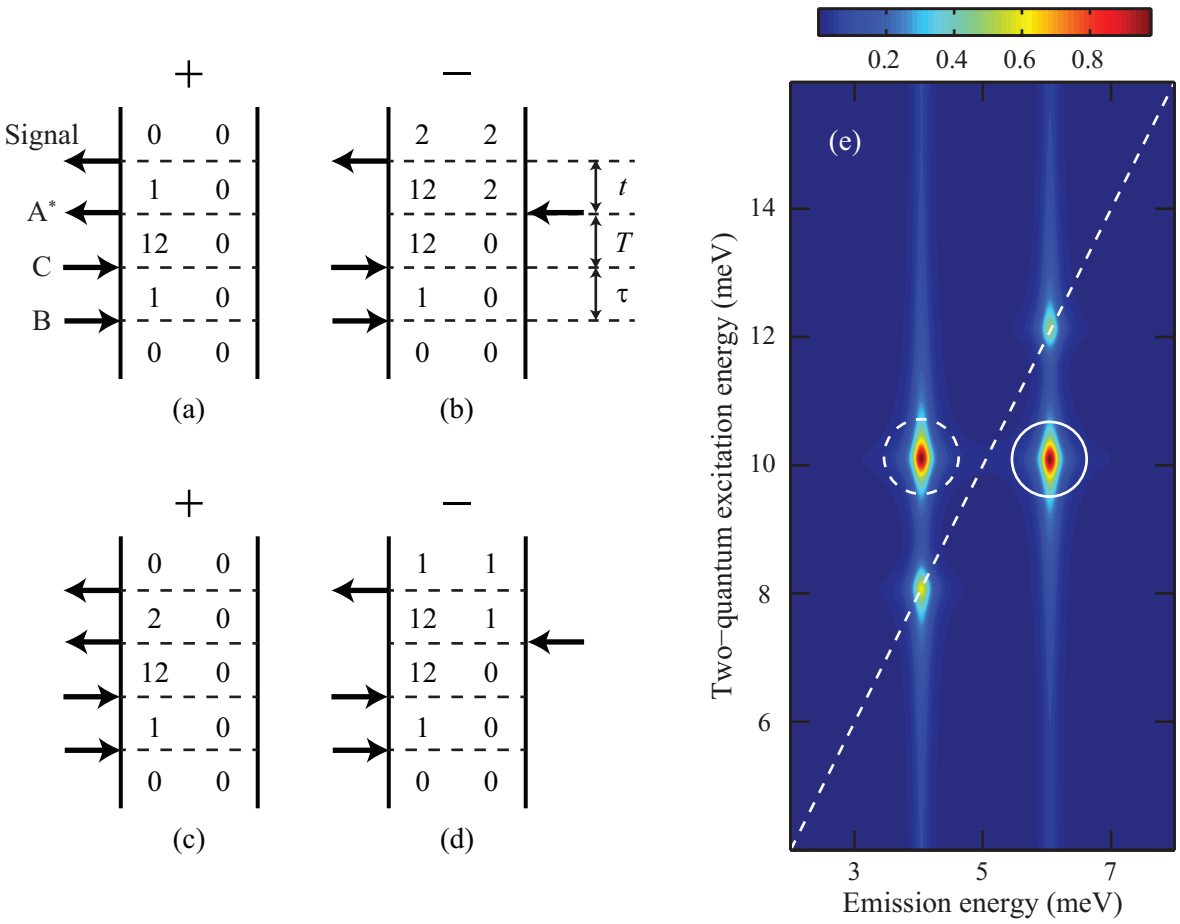

Figure 3.16: (a) – (d) Feynman diagrams for the coupling terms in the S_{III} time-ordering for the six-level system shown in Fig. 3.15. The pulse sequence is indicated in (a) and the relevant time delays are shown in (b). The + and - sign above the diagrams indicates the signal phase from the corresponding diagram. These diagrams show the first interaction involving the $|0\rangle \leftrightarrow |1\rangle$ transition followed by the $|1\rangle \leftrightarrow |12\rangle$. An equivalent set of diagrams with the first and second interactions involving the $|0\rangle \leftrightarrow |2\rangle$ and $|2\rangle \leftrightarrow |12\rangle$ transitions, respectively, is not shown. (e) Two-quantum non-rephasing absolute value spectrum. The coupling terms appear as the circled off-diagonal peaks.

Now that we have discussed the different types of 2D scans and spectra from the theoretical perspective, we will discuss the experimental aspects of 2DCS.

3.3 Two-dimensional coherent spectroscopy – experiment

We have shown how the TFWM technique is similar to 2DCS. The experimental implementations are also similar, in that even in a 2DCS experiment the TFWM signal is

detected as the time delay between a pair of pulses is scanned. However, 2DCS requires phase-stabilized measurement of signal electric field to enable taking a Fourier transform, which is a significant challenge for optical frequencies. Since stabilities up to a percent of the optical wavelength are needed, the experimental challenge increases for smaller wavelengths of light. Various experimental techniques have been developed to achieve phase-stability many of which rely on passive phase stabilization thorough dispersive optics [107, 108] and optical birefringence in the ultra-violet regime [88] and detection of signal field in the frequency domain. A similar method involving single-shot measurement of 2D spectrum has also been implemented [109]. A major disadvantage of these techniques is limited time delays that can be scanned. This disadvantage is countered by phase modulating collinear excitation beams and detecting photoluminescence [93] or photocurrent in case of semiconductors [110]. These experiments involve scanning two time delays through mechanical stage motion, which results in long scan durations. Additionally, since signal is detected as photocurrent, only heterostructures in a diode structure can be studied using this method. Since we want to study bare quantum wells with coherence lasting more than 10 ps, we use active stabilization of pulse delays is used [111]. The signal is detected on a spectrometer for different pulse delays.

3.3.1 Experimental setup

The experimental schematic is shown in Fig. 3.17, which shows four beam paths, in the box geometry, that are focused on the sample, which is kept in a cryostat, using lens f_1. The three excitation pulses go through three of these paths as shown in Fig. 3.17. The TFWM signal, which is emitted in the phase-matched direction given by Eq. (3.3), is collected by the collimating lens f_2. This direction is the same as that a pulse along the fourth path would follow. The fourth pulse is, however, routed around the sample while the experiment is executing, and is called the "Reference" pulse. The TFWM signal is interfered with this pulse and detected on a spectrometer through spectral interferometry, which enables

the detection of signal electric field [112]. The frequency resolution of the spectrometer is limited by the detection camera at ~ 40 μeV, half-width at half maximum (HWHM). This resolution can be improved by magnifying the image detected by the camera, although it results in decrease in efficiency due to reflection.

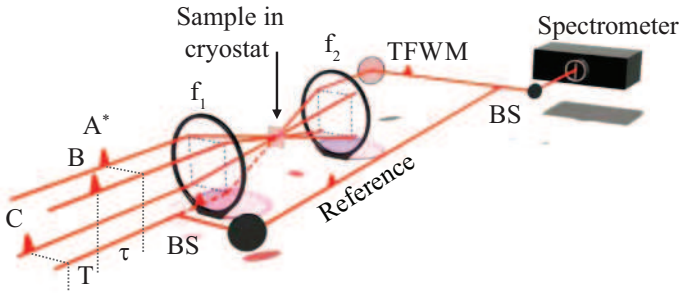

Figure 3.17: The experimental setup for two-dimensional coherent spectroscopy used in this work. The three excitation pulses are incident on the sample in the S_I time-ordering and are labeled A*, B and C. Lenses f_1 and f_2 are used to focus the excitation pulses and collimate the emitted transient four-wave mixing signal (TFWM), respectively. The reference pulse is routed around the sample, and interfered with the signal in a spectrometer. This figure has been adapted from Ref. [113].

Before we discuss the detection of signal in detail, it is imperative to mention how the pulses in the box-geometry are generated and phase stabilized. These pulses are generated from a mode-locked Titanium:Sapphire laser, which has a repetition rate of 76 MHz. The laser can be tuned in the wavelength range of 750 – 920 nm. The transform limited pulse duration can be set in the range of 100 – 200 fs. A single pulse from this laser is split into four parts, and aligned in the box-geometry, by a set of three actively phase stabilized Michelson interferometers dubbed the JILA multidimensional optical nonlinear spectrometer or JILA-MONSTR. Each pulse passes through a mechanincal stage, which is moved to scan the delay between different pulses. A continuous-wave HeNe laser co-propagates with the laser pulses, and is retro-reflected by a dichroic mirror at the exit of JILA-MONSTR, resulting in nested Michelson interferometers. These retro-reflected beams are interfered on photo-diodes. A mirror in each interferometer is mounted on a piezoelectric transducer. Thus, the path length of one arm of each interferometer can be adjusted by changing the drive voltage for

the transducer. The pulse delays are actively stabilized by stabilizing the voltage due to the interference from HeNe laser on the photo-diodes by driving the piezoelectric transducers through servo-loops. This system is used to step the delay between pulses with a $\lambda/100$ stability and accuracy [111]. Depending on the pulse being scanned, time delays of 300 ps – 1 ns can be achieved. More technical details on the JILA-MONSTR and active stabilization can be found elsewhere [111, 100].

Since the Reference pulse goes through different optics after exiting the JILA-MONSTR, another phase lock loop is used to stabilize it with respect to one of the excitation pulses coming passing through the sample to ensure no phase jitter in detection of the TFWM signal.

The polarization and average energy of the pulses coming out of the JILA-MONSTR are set using a half-wave plate followed by a linear polarizer in the path of each pulse. Circularly polarized pulses can be obtained by adding quarter-wave plates after the linear polarizers. The wave-plates and polarizers give us complete control over the polarization of the excitation pulses and the detected signal. In general, we define the polarization scheme used in a 2DCS experiment by a series of four alphabets/symbols, which indicate the polarization of the three excitation pulses, and the detected signal. For the S_I time ordering, the four alphabets/symbols denote the polarization of pulses A, B and C followed by that of the detected signal. Orthogonal linear polarizations – horizontal and vertical with respect to the optics table is denoted by letters X and Y, respectively. Similarly orthogonal circular polarizations – right-circular (σ_+) and left-circular (σ_-) polarizations are denoted by the symbols $+$ and $-$, respectively. For instance, the polarizations scheme $+-+-$ implies pulses A and C with σ_+ polarization and B and the signal with σ_- polarization. Some of the polarization schemes that are commonly used are – collinear (XXXX or YYYY), cross-linear (XYYX or YXXY), and co-circular ($++++$ or $----$) As we will see later, this versatility is extremely useful.

In addition to the polarizers and wave-plates, we also have a liquid crystal variable

retarder in the beam path of pulses A and B. These variable retarders are used to eliminate noise due to scatter in the detected signal through phase cycling, which will be discussed in Section 3.3.2.

3.3.2 Obtaining 2D spectrum

We have outlined the experimental design and setup. Next we will discuss how a 2D spectrum is obtained from experimentally measured data, including tricks to reduce noise and detection of the signal phase.

Electric field detection: Optical electric fields in the visible range oscillate at a few hundred terahertz, which cannot be detected by electronics directly. We use spectral interferometry to measure the electric field of the signal [112]. The signal and reference pulses propagate in the same direction with a time delay between them. The frequency domain interference (I) between a reference pulse and the signal is detected as

$$\begin{aligned} I(\omega) &= |E_R(\omega) + E_S(\omega)|^2 \\ &= |E_R(\omega)|^2 + |E_S(\omega)|^2 + E_R^*(\omega)E_S(\omega) + E_R(\omega)E_S^*(\omega) \end{aligned} \tag{3.15}$$

where E_R and E_S are the reference and signal complex electric fields, respectively. We can Fourier transform the measured spectrum to time-domain, isolate one of the interference terms, and, through inverse Fourier transform, obtain the interference term

$$S_{int}(\omega) = E_R^*(\omega)E_S(\omega) = |E_R(\omega)||E_S(\omega)|\mathrm{e}^{i[\omega\,\delta t + \{\phi_S(\omega) - \phi_R(\omega)\}]} \tag{3.16}$$

where δt is the time delay between signal and reference. ϕ_R and ϕ_S are the spectral phases of the reference pulse and the signal, respectively. $|E_R|$ is obtained through the reference spectrum while δt can be measured from the Fourier transform of Eq. (3.15). Thus, Eq. (3.16) results in the signal field $E_S(\omega)$ under the assumption that $\phi_R(\omega) = 0$. The signal electric field spectrum $E_S(\tau, \omega_t)$ is measured as a function of the time-delay that is scanned.[1] We shifted to denoting the frequency as ω_t to relate to the emission energy axis in a 2D

[1] The actual implementation is slightly different, as we will discuss later.

spectrum. A numerical Fourier transform of the measured signal along delay τ is taken to obtain a 2D spectrum $E_S(\omega_\tau, \omega_t)$.

Phase cycling: As mentioned in Section 3.1.1, phase-matching condition is used to isolate the TFWM signal from the linear response of the sample. However, a perfect isolation of the signal is an idealization; some scatter from excitation pulses is also emitted, in the phase-matched direction, along with the TFWM signal. This scatter can be reduced significantly through phase cycling [111].

The basic idea behind phase cycling is that the TFWM signal is measured for different phases of the incident pulses, which also modifies the detected signal. The liquid crystals are used to delay pulses A and B so as to modify their phase on the sample. Four spectra are recorded for each time delay. These spectra are processed to eliminate the noise due to scattering.

	A	B	C	S
1	+	+	+	+
2	-	+	+	-
3	-	-	+	+
4	+	-	+	-

Table 3.1: Phase cycling procedure

The phase cycling process is outlined in Table 3.1. Each row indicates the phase of excitation pulses (A, B and C) and the TFWM signal (S) for one of the four recorded spectrum. + and − signs are used to indicate electric fields with π phase shift between them. The phase of the TFWM signal depends on the phase of the excitation pulses. The phase-cycled signal is then calculated using the relation

$$S = \frac{1}{4}(S_1 - S_2 + S_3 - S_4) \tag{3.17}$$

where the subscripts denote the row numbers in Table 3.1. This procedure removes the scatter from each of the pulses.

2D spectrum: Although we mentioned earlier that $E_S(\omega)$ is measured for each time delay, that is not how the analysis is implemented. It is more efficient to record the interference term in Eq. (3.16) in the time domain, given by its Fourier transform $\mathcal{S}_{int}(t)$, which also enables us to deconvolve the artificial broadening due to the finite resolution of the spectrometer [114].

The time-domain interference term is recorded as a function of the scanned time delay τ to obtain $\mathcal{S}_{int}(\tau, t)$. An example of this signal is shown in Fig. 3.18(a), which was experimentally measured from a GaAs QW. The real time axis is obtained through a Fourier transform of the frequency axis obtained from the spectrometer. The dashed line indicates $t = 0$ and the value of real time axis at this point gives the delay δt between the signal and the reference pulse. This interference term $\mathcal{S}_{int}(\tau, t)$ is isolated by taking time cuts in the time-domain; the two solid lines indicate the region that is selected. The photon-echo like behavior of the signal is apparent, which allows us to take a time cut such as the one shown in Fig. 3.18(a). This time-cut reduces the noise significantly and results in a much cleaner spectrum than the one that would result without it. The reduced noise also allows us to scan up to larger values of τ, which results in better resolution in 2D spectrum.

After performing the processing mentioned above, we obtain the phase-cycled, two-dimensional time-domain interference term $\mathcal{S}_{int}(\tau, t)$. By taking a Fourier transform along both τ and t, we end up with the interference term in two-dimensions

$$S_{int}(\omega_\tau, \omega_t) = |E_R(\omega_t)||E_S(\omega_\tau, \omega_t)|\mathrm{e}^{i\phi_S(\omega_\tau, \omega_t)}. \tag{3.18}$$

Equation (3.18) is obtained after removing the spectral phase due to δt and under the assumption $\phi_R = 0$. A 2D spectrum $E_S(\omega_\tau, \omega_t)$ is obtained by dividing Eq. (3.18) by $|E_R(\omega_t)|$, which is measured by the spectrometer directly. Figure 3.18(b) shows the absolute value spectrum $|E_S(\omega_\tau, \omega_t)|$ obtained from the time-domain signal shown in Fig. 3.18(a).

Signal phase: In the discussion presented above we have implied that the signal phase is correctly measured. This signal phase is, in general, incorrect because of the ran-

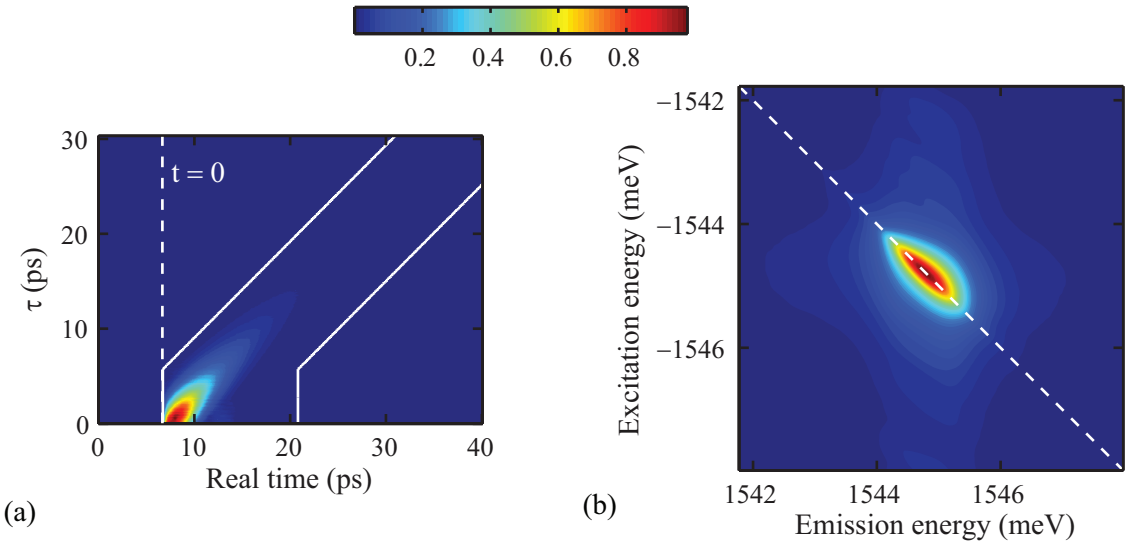

Figure 3.18: (a) Experimentally obtained absolute value 2D signal in the time domain from the heavy hole exciton resonance in GaAs/$Al_{0.3}Ga_{0.7}As$ quantum well. The dashed line in (a) indicates $t = 0$. The solid lines in (a) indicate the time cuts applied to reduce the detected scatter; the signal outside the two lines is set to 0. (b) 2D spectrum in the frequency domain by taking Fourier transform of the signal shown in (a) along τ and t.

dom phase shifts introduced when the delay between pulses is locked, and can be corrected through an all-optical technique [115]. Another method to obtain the correct signal phase is though a complimentary experiment – spectrally resolved pump-probe (SRPP) signal, which is analogous to a TFWM experiment. Under the right conditions the SRPP signal is equivalent to the TFWM signal [116].

$$S_{PP}(\omega_t) = \mathrm{Re}\left(E_S(\omega_t)|_{\tau=0}\, e^{i\phi_0}\right) \tag{3.19}$$

where $S_{PP}(\omega_t)$ is the spectrally resolved pump-probe signal, $E_S(\omega_t)$ is the measured complex signal field, and ϕ_0 is the phase offset is added to satisfy the equality. The experimentally measured spectra from the 2DCS and SRPP experiments are matched by varying ϕ_0. The result of such a procedure for the absolute value spectrum in Fig. 3.18(b) is illustrated in Fig. 3.19, where the SRPP signal is shown as black dots and the equivalent 2DCS signal is plotted as the red line. The measured ϕ_0 is then used to obtain the correctly-phased 2D

spectrum

$$E_{S,cor}(\omega_\tau, \omega_t) = E_S(\omega_\tau, \omega_t)\mathrm{e}^{i\phi_0}. \tag{3.20}$$

Figures 3.20(a) and 3.20(b) plot the real and imaginary parts of the absolute value 2D spectrum in Fig. 3.18(b).

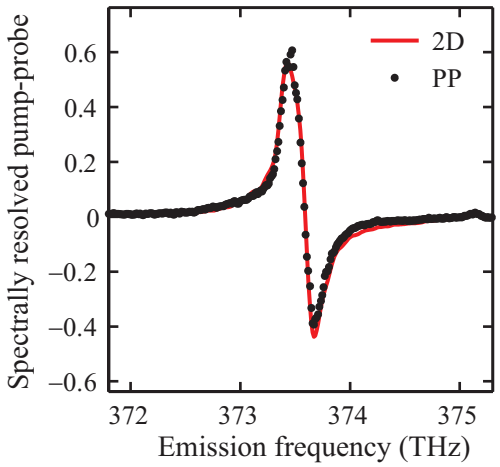

Figure 3.19: The real part of the 2D signal for $\tau = 0$, shown in red line, is adjusted to match the measured spectrally resolved pump-probe signal (PP) shown as black dots.

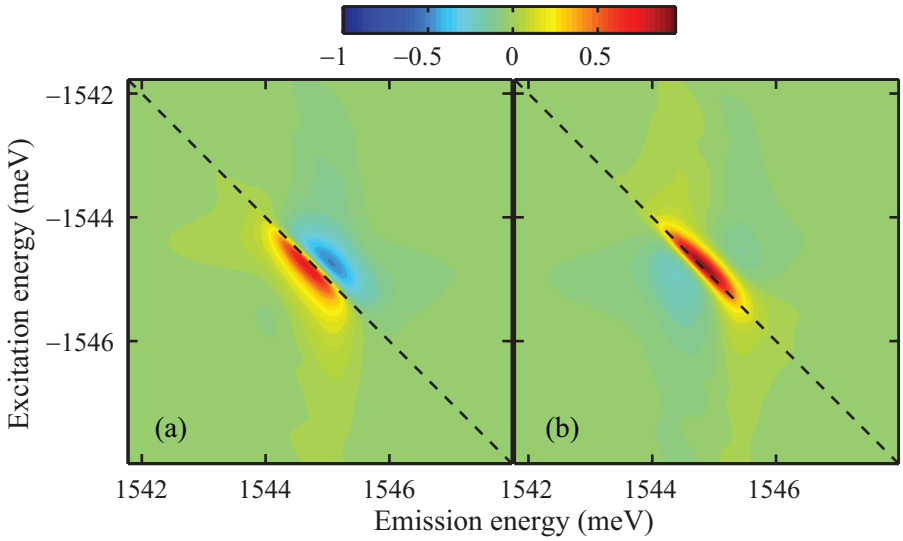

Figure 3.20: (a) Real and (b) imaginary part of the absolute value spectrum shown in Fig. 3.18(b).

However, there are certain disadvantages of using this method to find the signal phase.

These disadvantages arise from some of the following conditions, which must be satisfied for Eq. (3.19) to be true, and, consequently, this method to work:

- The system must be in a **real** population state during T. For instance, pulses A and B with orthogonal polarizations create a spin grating, which is not a real population grating. As a result, this technique will not work for such a polarization scheme.
- The delay between the pump and probe pulses should be set equal to T in the 2DCS experiment.
- The average power of the pump should equal the sum of the average powers of pulses A and B. The average power of the probe should equal the average power of pulse C.
- The measured signal phase is very sensitive to the pump-probe overlap and the overlap of excitation pulses in the 2DCS experiment.

The last two conditions are unique to semiconductors because of excitation induced effects such as EID and EIS. These conditions somewhat limit the applicability of this technique to find the signal phase. Despite these limitations, SRPP is applied extensively to extract the correct signal phase in this work.

3.4 Two-dimensional coherent spectroscopy – previous studies

In this chapter, we have discussed the experimental and theoretical aspects of 2DCS. Although this discussion was carried out for model systems, similar spectra are observed in QWs. In addition to the kinds of spectra discussed several modifications are made depending on the system and the experimental objective. We will discuss some of these modifications, which are relevant to this work, which will be discussed now.

Polarization dependence: We discussed the exciton and biexciton polarization selection rules in Section 2.7. As a result of those selection rules, the TFWM signal emitted

by an excitonic system can vary significantly as demonstrated by Bristow et al. [117]:

- The biexciton signal appears red-shifted compared to the exciton peak along the emission energy axis.
- The exciton signal is reduced significantly for the cross-linear polarization scheme, resulting in relatively stronger biexciton peak.
- The biexciton peak is not present for the co-circular polarization scheme, as is the case in the spectrum in Fig. 3.18(b).

Since the biexciton signal appears as a separate peak, we will see that, it is possible to obtain the parameters of the exciton $\leftrightarrow$ biexciton resonance. Furthermore, frequency dependent biexciton binding energy can also be easily measured [118].

Many-body effects: It is worth noting that the real part of 2D spectrum for the HH exciton resonance shown in Fig. 3.20(a) has a dispersive lineshape, i.e. it comprises comparable positive and negative parts with node on the diagonal line, which is not expected from a two-level system. Such a peak-shape was explained through EIS, which is a phenomenological many-body effect resulting from exciton-exciton interactions [13]. In addition to this, other many-body effects such as EID and local-field effects also modify the TFWM signal [5], and, as a result, the 2D spectrum. 2DCS is ideal to identify the effect of these phenomenological many-body effects, and can be simulated through numerical calculations, which are presented in Appendix B. Such numerical calculations are computationally intensive. In this work, however, we will discuss these many-body interactions from a different perspective, similar to those discussed in Section 3.2.5. We will show that such a description is much easier to simulate, and enable quantifying the strength of these interactions.

T-dependence: We will present studies on the spectral diffusion of excitons in QWs in this work. Previously spectral diffusion has been studied using other techniques such as 3PEPS spectroscopy [36, 40]. 2DCS is an excellent technique to study such a phenomenon,

and has been used to study spectral diffusion in molecular systems extensively [39, 119]. Spectral diffusion is measured by recording one-quantum 2DCS spectra for different values of T. These spectra directly depict the redistribution of resonance frequencies of the excited population. Through these measurements we will highlight the limitations of the strong-redistribution approximation, which is generally assumed for QW excitons. Additionally, it can be used to accurately model exciton-phonon interactions.

In this chapter we presented a general discussion of 2DCS, and the several studies relevant for the results that will be presented in this work. We will discuss the specific experimental results obtained in the following chapters. These results will include studies of excitons in (110)-oriented GaAs QWs, spectral diffusion of exciton in QWs and modeling QW excitons as bosons. We will find that the properties of 2DCS that we have discussed in this chapter, result in significant advantages for the aforementioned studies.

Chapter 4

Excitons in (110)-Oriented GaAs Quantum Wells

In this chapter, we report measurements of the homogeneous and inhomogeneous linewidths of the HH exciton state in a (110)-oriented GaAs QW sample for excitation polarized along X and Y directions in the plane of the QW. We have studied the 8-nm-wide QWs, which we discussed in Section 2.9.2. We have already discussed the reduced symmetry for (011)-oriented GaAs QWs, and some of the resulting properties in Section 2.6. We also discussed the anisotropic absorption coefficients for two orthogonal linear polarizations in Section 2.9.2. We find that while unequal absorption coefficients give rise to anisotropic EID effects, and, thus, different homogeneous linewidths for excitons excited along the two polarization directions, the extrapolated zero-excitation density homogeneous linewidth is the same for excitations along both directions. A study of the temperature dependence of the homogeneous linewidth reveals an activation-like behavior of thermal broadening. We also compare the results we obtain with those reported for (001)-oriented GaAs QWs to contrast the exciton dephasing mechanisms in QWs grown along the two growth directions.

The sample was kept in a cold finger continuous flow helium cryostat. The sample temperature was varied from 6 – 50 K. The excitation pulses are $\sim$ 120 fs long and are obtained from a 76 MHz repetition rate mode-locked Ti:sapphire laser. All the excitation beams are set to have, on an average, equal photon density per pulse. We present results for the collinear polarization schemes with X and Y polarization. The X and Y axes coincide with the [001] and [$1\bar{1}0$] crystal axes, respectively. Experiments were performed with the

excitation pulses in the rephasing time ordering.

4.1 Measuring linewidths

First we will present a typical 2D spectrum for these QWs and illustrate the measurement of the homogeneous and inhomogeneous linewidths. Figure 4.1 shows the (a) real part and (b) absolute value of a typical rephasing one-quantum 2D spectrum obtained for polarization scheme Y with the sample at a temperature of 10 K. The laser spectrum had a full width at half-maximum bandwidth of $\sim$ 16 meV and was tuned to be resonant with the HH exciton resonance, as indicated by the dotted lines in Fig. 4.1. In Fig. 4.1(a), the central dispersive peak (Ex) on the diagonal line is the HH exciton resonance. The negative absorptive peak (Bx) that is red-shifted relative to the exciton peak along the emission axis is due to the HH bound biexciton state. The marked elongation of the HH exciton peak in the diagonal direction is because of large inhomogeneous broadening in the sample. The dispersive lineshape of the exciton peak suggests that the signal is dominated by many-body effects including EID and excitation-induced shift [13].

From an absolute value 2D spectrum, such as Fig. 4.1(b), the homogeneous and inhomogeneous linewidths are obtained by simultaneously fitting the diagonal and cross-diagonal slices to analytical lineshapes [104]. Figure 4.2 shows an example of the data (dashed line) and fit curves (solid line) for slices from a 2D spectrum for polarization scheme Y. The sample was kept at a temperature of 10 K and the average photon density of $\sim$ 5.4 x 10^{11} cm^{-2} per pulse was incident on it. There is a distinct difference between the cross-diagonal slice and the obtained fit on the negative energy wing of the main peak. This discrepancy is due to the weak biexciton peak, which was not considered while performing the fits. For the slices shown in Fig. 4.2, we obtained values of 0.105 and 1.9 meV for the homogeneous and inhomogeneous linewidths, respectively. These, and the linewidths reported later on, are the half width at half-maximum (HWHM) values of the Lorentzian and Gaussian distribution functions, which correspond to homogeneous and inhomogeneous

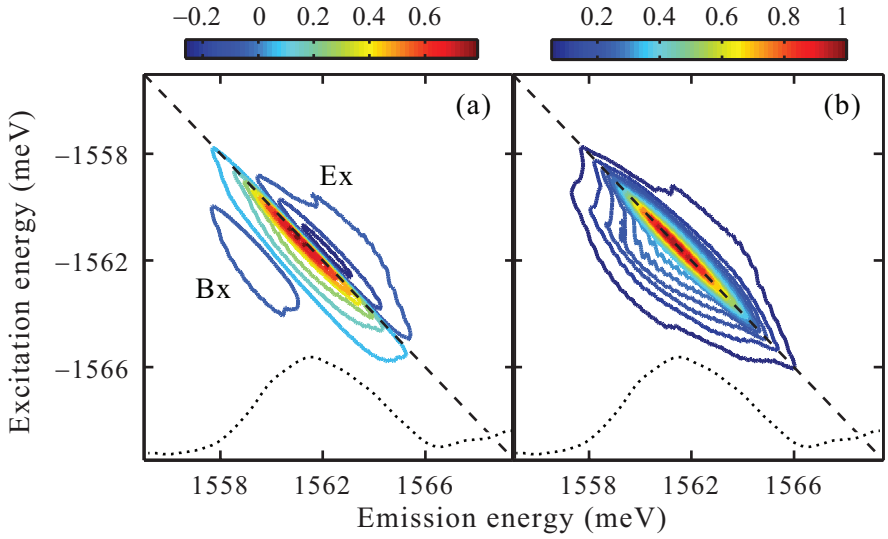

Figure 4.1: A typical (a) real part and (b) absolute value normalized 2D spectra of the complex rephasing signal for polarization scheme Y and sample temperature of 10 K. The exciton (Ex) and biexciton (Bx) peaks are marked in (a). The dotted line at the bottom of the figures shows the linear absorption spectrum.

linewidths, respectively, [104] and have been obtained after deconvolution of the signal with the spectrometer response. The ratio of the linewidths suggest that inhomogeneity is the dominant broadening mechanism in (110)-oriented GaAs QWs. This result is expected from a rough growth front along the (110) direction for GaAs [120].

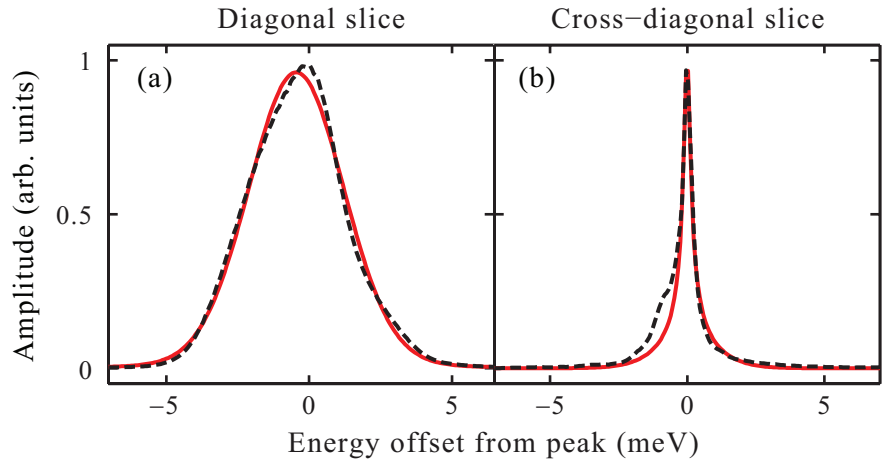

Figure 4.2: Slices (dashed line) and fits (solid line) along the (a) diagonal and (b) cross-diagonal directions of the normalized absolute value spectrum.

4.2 Excitation-density dependence

On repeating the above measurement for polarization scheme X while keeping the other parameters the same, we measured a smaller homogeneous linewidth (0.086 meV) while the inhomogeneous linewidth was the same. We investigated the reason for unequal homogeneous linewidths for the two polarization schemes by varying the average photon density incident on the sample. Figure 4.3 shows the variation of the homogeneous linewidth with the average photon density per pulse incident on the sample kept at a temperature of 10 K, along with a representative error bar obtained by repeating the experiment multiple times. Over the range of photon density shown, the HH exciton state exhibits different homogeneous linewidths for X and Y polarization schemes. For both the polarization schemes, the homogeneous linewidth increases with increasing photon density due to EID [55, 4], while the inhomogeneous linewidth is constant at ~ 1.9 meV.

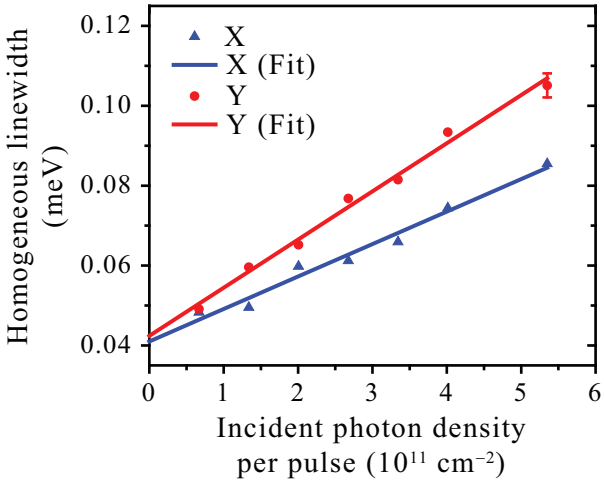

Figure 4.3: Incident photon density dependence of homogeneous linewidth for X (triangles) and Y (circles) polarization schemes. The linear fits to the data are shown by the solid lines. A representative error bar, obtained by repeating the same experiment multiple times, is shown. The sample was kept at a temperature of 10 K.

For low photon density incident on the sample, the photon density dependence of the

homogeneous linewidth can be approximated as [121]

$$\gamma(\phi) = \gamma_0 + \gamma_{EID} * \phi \tag{4.1}$$

where γ_0 is the zero-excitation density homogeneous linewidth, γ_{EID} is the rate of increase of homogeneous linewidth with average photon density per pulse ϕ incident on the sample. The solid lines in Fig. 4.3 are the fits to the data using Eq. (4.1). The fit parameters listed in Table 4.1 show that while the value of γ_0 is the same (within the errors obtained by assuming constant error in homogeneous linewidth over the range of photon density), different values of γ_{EID} are obtained for the two polarization schemes.

Polarization scheme	γ_0 (μeV)	γ_{EID} (10^{-17} eVcm^2)
X	41 ± 2	8.1 ± 0.6
Y	42 ± 2	12.1 ± 0.5

Table 4.1: Parameters of Eq. (4.1) for the fits shown in Fig. 4.3.

In Eq. (4.1), we use the average photon density per pulse incident on the sample rather than the exciton density in the QWs to quantify the effect of EID on the homogeneous linewidth. This is valid because, for relatively low photon density, the excitation density is directly proportional to the incident photon density. From the absorption spectra shown in Fig. 2.11, we estimate that the absorption of the HH exciton transition is ~ 1.3 times larger for Y polarization compared to X polarization. The difference in the exciton density for the same photon density incident on the sample results in different γ_{EID} values for the two polarization schemes. From the ratio of γ_{EID} for the two polarization schemes, we estimate an excitation density ratio of 1.5 ± 0.1 for polarization scheme Y to that for X. This ratio is in reasonable agreement with the estimate from the absorption curves and supports our analysis that anisotropic EID results in different homogeneous linewidth of the HH exciton transition polarized along X and Y axes.

For an electronic transition, both the absorption coefficient and the radiatively limited homogeneous linewidth are directly proportional to the square of the transition dipole mo-

ment [15]. Hence, if radiative decay was the only process contributing to γ_0, from unequal absorption coefficients for the HH exciton transitions polarized along X and Y axes, we would expect different γ_0 for the two polarizations. Equal values of γ_0 for both the polarizations suggest that it is not radiatively limited.

4.3 Population decay rate

We measure the population decay times from a rephasing zero-quantum 2D spectrum. Figure 4.4(a) shows such a 2D spectrum, for Y polarization scheme with the sample at a temperature of 10 K, where we plot the normalized signal intensity. When only a single resonance is excited, as is the case presently, the system is in a population state during T. Hence the linewidth in the mixing energy direction gives the population linewidth. We fit a slice from the zero-quantum 2DFT spectrum, indicated by the dashed line in Fig. 4.4(a), to a double Lorentzian. The linewidth of the narrower Lorentzian gives the population decay rate. The slice (dashed line) and the best-fit curve (solid line) are shown in Fig. 4.4(b). We measure a population linewidth of $\sim$ 10 μeV at a temperature of 10 K. We would like to point out that we did not measure different population linewidths for X and Y polarization schemes. However, due to $\sim$ 2 μeV uncertainty in the population linewidths measured, we cannot confirm the presence of non-radiative population decay pathways. In the absence of pure dephasing mechanisms, the measured population linewidth would result in a homogeneous linewidth of $\sim$5 μeV for both X and Y polarization schemes, according to Eq. (2.12). Since measured γ_0 is roughly 8 times this value, we can unambiguously conclude that pure dephasing processes contribute significantly to the measured γ_0. Exciton-phonon interaction is an important mechanism that contributes to the homogeneous linewidth in QWs. We investigate this interaction through the temperature dependence of the homogeneous linewidth.

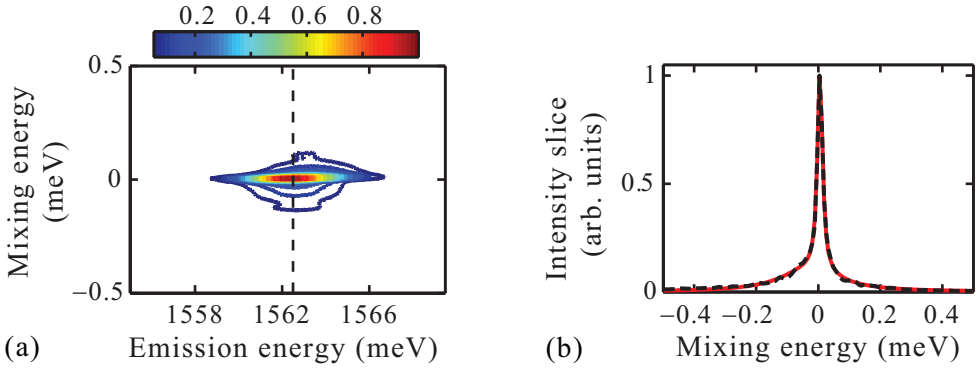

Figure 4.4: A rephasing zero-quantum 2DFT spectrum for Y polarization scheme is shown in (a). The spectrum plots signal intensity. The slice (dashed line) at the center of the inhomogeneous distribution of the spectrum in (a) is shown in (b). The solid line in (b) shows the best-fit double Lorentzian curve.

4.4 Temperature dependence

We repeated the power dependence study presented earlier for different sample temperatures varying from 6 – 50 K. We plot the values of γ_0 for X and Y polarization schemes for different temperatures in Fig. 4.5. For both the polarization schemes, nearly equal values of γ_0 are obtained over the temperature range studied as expected from the discussion of the anisotropic EID effect earlier. Additionally, we find that γ_0 increases with the sample temperature for both the polarization schemes. As the lattice temperature increases, exciton-phonon interactions increase resulting in a faster dephasing of excitons. Since, the phonon population follows the Bose - Einstein distribution, we can describe the thermal broadening as

$$\gamma_0(T_s) = \gamma_0(0) + \gamma^* \left[e^{\frac{E_{ph}}{k_B T_s}} - 1 \right]^{-1} \tag{4.2}$$

where we have written γ_0 as a function of the sample temperature T_s, γ^* is the amplitude of the thermal dephasing term, E_{ph} is the energy of the dominant phonon mode responsible for the dephasing and k_B is the Boltzmann constant. In Eq. (4.2) we have considered the contribution of only a single phonon mode to the pure dephasing of excitons. Equation (4.2) is similar to the one used by Lee et al. [122] for (001)-oriented GaAs QWs. The difference

here is that we have not used the term that is linear in T_s, kept E_{ph} as an adjustable parameter and not considered impurity scattering effects. The best-fit curves are shown in Fig. 4.5 by a solid (dashed) line for polarization scheme X (Y). The values obtained for the fit parameters, which are equal for the two polarization schemes (within the errors), are listed in Table 4.2.

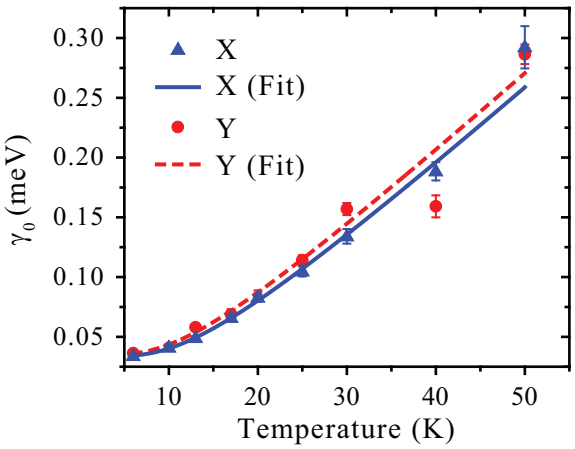

Figure 4.5: Sample temperature dependence of γ_0 for X (triangles) and Y (circles) polarization schemes. The fit, as per Eq. (4.2), is represented by the solid (dashed) line for X (Y) polarization scheme. The error bars represent the statistical errors only and additional systematic error might also be present. Note that for a few temperatures the data points for X and Y polarization schemes overlap.

We find the zero-excitation density homogeneous linewidth extrapolated to 0 K, $\gamma_0(0)$, is ~ 34 μeV (corresponding to a dephasing time of ~ 20 ps) and phonons with energy of ~ 3 meV are predominantly responsible for the faster dephasing of the HH exciton polarization at high temperatures. Usually E_{ph} corresponds to a transition to a real state which, in this case, could be delocalized exciton states centered ~ 3 meV above the line-center of the HH exciton inhomogeneous distribution. This activation would be an incoherent process that we can probe by varying the time delay between the second and third pulses [113]. We do not see any activation peak in these complimentary experiments (spectra not shown), which suggests that the thermal broadening is due to an elastic exciton-phonon scattering mediated virtual activation process. However, an activation peak too weak to be seen and/or

Polarization scheme	$\gamma_0(0)$ (μeV)	γ^* (meV)	E_{ph} (meV)
X	34 ± 2	0.24 ± 0.03	3.1 ± 0.3
Y	35 ± 4	0.22 ± 0.08	2.9 ± 0.7

Table 4.2: Parameters of Eq. (4.2) for the fits shown in Fig. 4.5.

activation to a dark state due to a change in the in-plane momentum of excitons cannot be ruled out. Equal values of γ^* and E_{ph} for both the polarization schemes suggest that the activation mechanism is isotropic for exciton transitions polarized along X and Y directions.

Compared with the population times reported earlier, the values of $\gamma_0(0)$ obtained for the two polarizations indicate that the HH exciton transition is dominated by pure dephasing processes even at low temperatures. We attribute this dephasing to acoustic phonon assisted tunneling of excitons between localization sites,[123] which exists due to disorder in the sample. This tunneling is important at low temperatures and does not show any activation-like behavior if it is accompanied with the emission of phonons.

We would like to point out that studies of temperature dependence of homogeneous linewidth of HH excitons in (001)-oriented GaAs QWs have shown [122, 124, 125, 126] that at low temperatures (< 50 K) the linewidth increased linearly with temperature. This behavior would be replicated by Eq. (4.2) for $E_{ph} \ll k_B T_s$. Thus, we conclude that for (001)-oriented GaAs QWs E_{ph} would be lesser than what we measure for the (110)-oriented QWs. We would also like to note that for (001)-oriented GaAs QWs with well widths ranging from 5 – 13 nm, low temperature dephasing times of 1 – 12 ps have been reported [124, 55, 126, 127, 31]. The homogeneous linewidth of excitons is sensitive to the inhomogeneity. As a consequence, the results in the publications cited above show quite large variation in dephasing times although all those results are for samples with relatively small inhomogeneous linewidth (HWHM < 0.5 meV). While the dephasing time we report here for (110)-oriented QWs is slightly longer than these values, it is smaller than the value of ~ 70 ps reported for (001)-oriented sample with significantly greater inhomogeneity [2].

In conclusion, we have measured the linewidths of the HH exciton resonance in (110)-oriented GaAs QWs. The measurements reveal that inhomogeneous broadening is the dominant broadening mechanism. In addition to reporting the dephasing time in a QW with reduced symmetry such as (110)-oriented GaAs QWs for the first time, we have also discussed important phenomena that affect the dephasing time. We show that anisotropic dipole moments along X and Y crystal axes, through EID, result in different homogeneous linewidths for exciton transitions polarized along the two axes. We find that the increase in homogeneous linewidth with temperature is isotropic along X and Y axes and shows an activation-like behavior, and that the homogeneous linewidth, even at low temperatures, is dominated by pure dephasing processes.

Another interesting feature of these QWs, which we have not discussed, is the presence of finite absorption between the HH and LH peaks in the absorption spectrum shown in Fig. 2.11. The absorption in this spectral region is probably due to the transition between the second HH state and the electron ground state. We observe peaks due to this nominally disallowed transition in some preliminary studies, which are discussed in Appendix C.

Chapter 5

Spectral Diffusion

We introduced the phenomenon of spectral diffusion, in which the resonance energy of the excitation changes over time, in Section 2.5. We also defined the normalized frequency-frequency correlation function, which we will be referred to as the correlation function from hereon, which is generally used to quantify spectral diffusion. Several experiments including 3PEPS [36, 37, 40, 102] and various observables in 2DCS [39, 119, 128] are used to study the spectral diffusion in various systems. Regardless of the technique, the final goal is to measure the correlation function, which is approximated through these experiments.

As mentioned in Section 2.5, the description of spectral diffusion through the correlation function is only valid in the case of the strong redistribution approximation. In this regime both increase and decrease of energy of the excitation are equally likely[129]. We have studied the spectral diffusion of excitons in QWs. In general, the strong redistribution approximation is assumed to be valid for excitons in QWs [130, 40, 41]. Furthermore, it is assumed that the correlation function decays exponentially with time; this is the Gauss-Markov approximation [38, 40].

In this chapter, we will discuss theoretical description of spectral diffusion in the strong redistribution approximation and its effect on 2D spectra through simulations. Next, we will present experimental results that show that the strong redistribution approximation is not valid for excitons in QWs for low sample temperatures. Finally, we will quantify spectral diffusion, for high sample temperatures, by measuring the correlation function through a

numerical fitting procedure. We show that even in the limit of strong redistribution approximation, the correlation function decay is non-exponential, which violates the Gauss-Markov approximation.

5.1 Frequency-frequency correlation function

The most common way of quantifying spectral diffusion is through the normalized the correlation function $C(T)$ defined in Eq. (2.16). Usually $C(T)$ is not measured directly, but is inferred through other experiments. One such experiment is the 3PEPS spectroscopy, which we discussed in 3.1.3. The decrease in the photon echo peak delay τ_m corresponds to a decrease in the value of the correlation function. It has been shown that the two values are proportional to each other, at least for large time delays [36, 37]. However quantitative analysis is based on assumptions of functional form of $C(T)$ [39]; an exponential decay is assumed in the Gauss-Markov approximation [38, 40]. Thus, a direct measurement of the correlation function is useful for quantifying spectral diffusion.

The TFWM signal given by Eq. (3.7) is modified due to the correlation function as [39]

$$S_{S_I,SD}(\tau,T,t) = 2|E|^3{\mu_{01}}^4 \mathrm{e}^{-i\Delta_{01}(\tau-t)} \mathrm{e}^{-(\gamma_{01}\tau+\Gamma_1 T+\gamma_{01}t)} \mathrm{e}^{-\frac{1}{2}{\sigma_{01}}^2(\tau^2+t^2-2C\tau t)} \Theta(\tau)\Theta(T)\Theta(t) \quad (5.1)$$

where all the parameters have the usual meaning. Equation (5.1) is exactly the same as Eq. (3.7) for $C = 1$.

The effect of change in the correlation function is apparent in 2D spectrum. Figures 5.1(a) and 5.1(b) illustrate this effect for $C = 1$ and $C = 0$, respectively. We used $\gamma_{01} = 0.1$ meV and $\sigma_{01} = 0.4$ meV. It is apparent that the the peak in 2D spectrum is no longer elongated along the diagonal line for $C = 0$. The excitation and emission energies are perfectly correlated for $C = 1$ resulting in the peak that is elongated along the diagonal direction in Fig. 5.1(a). For $C = 0$ there is no correlation between the excitation and emission frequencies, resulting in a peak that looks homogeneously broadened. The visible

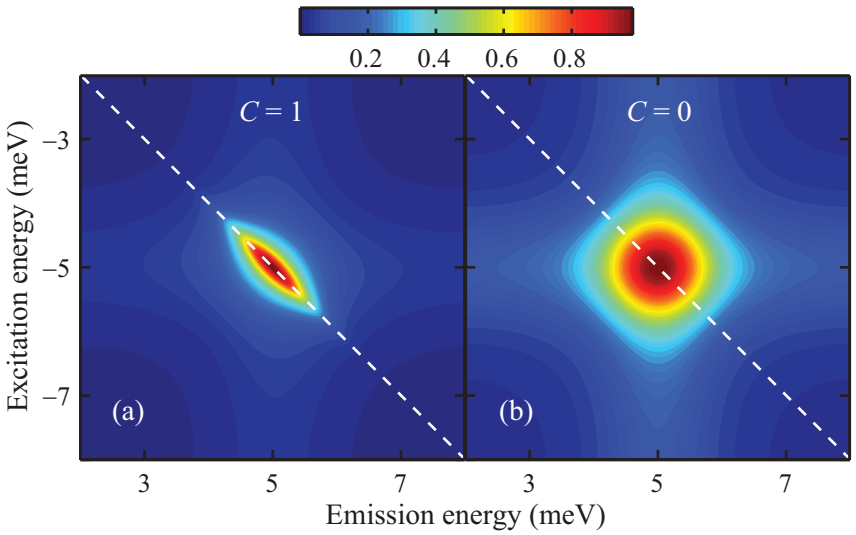

Figure 5.1: Effect of the frequency-frequency correlation function C on 2D spectrum for an inhomogeneously broadened resonance with (a) $C = 1$ and (b) $C = 0$.

effect of correlation function on 2D spectrum makes 2DCS a powerful technique to study spectral diffusion. A number of observables such as peak ellipticity [119], peak slope [128], and several others, as summarized by Roberts et al. [39] have been used as a proxy for the correlation function. In general, the change in the shape of the 2D peak is measured as a function of the waiting time T to quantify spectral diffusion through $C(T)$. Nevertheless, these observables only approximate the correlation function and not measure them directly. In this chapter, we would show that $C(T)$ can be obtained directly though a numerical fitting procedure. However, before we discuss those measurements, we present measurements that test the validity of the strong redistribution approximation for excitons in QWs. This is an important exercise because the correlation function does not have a physical meaning if the strong redistribution approximation is not valid.

5.2 Validity of the strong redistribution approximation

5.2.1 Spectral diffusion from 2D spectra

Spectral diffusion is measured by taking a series of rephasing one-quantum 2D spectra for different values of T. Since the system is in a population state during delay T, the change in 2D peak shape with T directly gives the redistribution of exciton energy. We have studied the spectral diffusion of HH excitons in (001)-oriented GaAs QW sample, which is described in Section 2.9.1. We can directly observe the effect of spectral diffusion in experimentally measured 2D spectra.

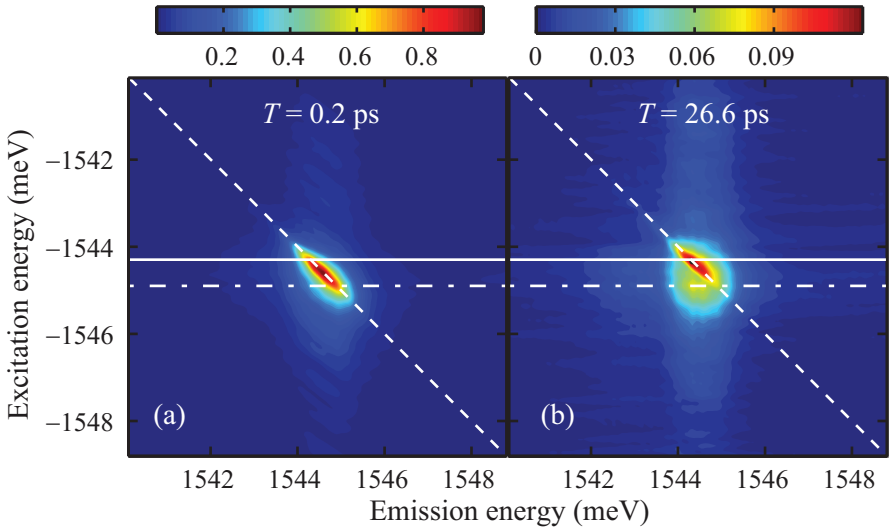

Figure 5.2: Rephasing one-quantum absolute value 2D spectra with (a) $T = 0.2$ ps and (b) $T = 26.6$ ps with the sample at a temperature of 5 K. We will compare the redistribution of the population of excitons created with energies indicated by the two horizontal lines. Note the asymmetric peak in (b).

Figures 5.2(a) and 5.2(b) show the HH exicton peak in rephasing one-quantum absolute value 2D spectra taken with $T = 0.2$ and 26.6 ps, respectively, with the sample kept at a temperature of 5 K. The peak in Fig. 5.2(a) is elongated along the diagonal line because the excitation and emission energies are correlated across the inhomogeneous distribution. In other words, excitons created with a particular energy radiate TFWM signal at the same

energy. The peak in Fig. 5.2(b), however, broadens due to redistribution of the exciton energy. This broadening, however, is different than in the simulation shown in Fig. 5.1(b). The difference arises because of preferential relaxation of excitons that were created at a higher energy, as denoted by the dash-dot line, to lower localized states compared to the excitation of low energy excitons to higher energies.

The high energy excitons are delocalized, and can easily be trapped in localization sites through emission of phonons. The low energy excitons are localized, and need to absorb phonons to tunnel through the localization barrier. Since, there isn't a significant phonon population at 5 K, the excitation of low energy excitons to higher energies is not favorable. Emission of phonons, however, does not need a phonon population. Thus, for low temperatures phonon emission is more likely than phonon absorption, resulting in the preferential relaxation of excitons and the resulting asymmetric peak in Fig. 5.2(b). We further confirm this claim through experiment performed at higher temperatures.

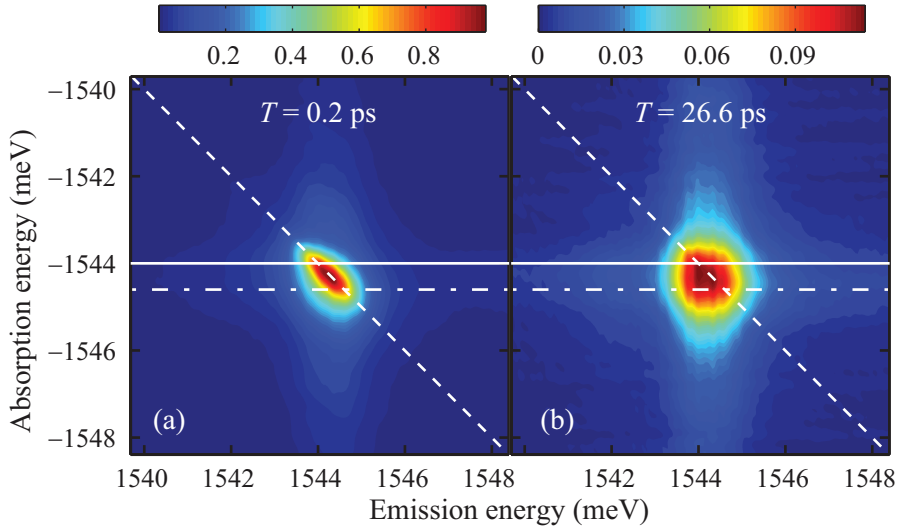

Figure 5.3: 2D spectra with (a) $T = 0.2$ ps and (b) $T = 26.6$ ps with the sample at a temperature of 25K. We will compare the redistribution of the population of excitons created with energies indicated by the two horizontal lines.

Figure 5.3 shows 2D spectra which are the same as those in Fig. 5.2 but were measured with the sample at a temperature of 25 K, which results in significant differences

between them. Firstly, the peak in Fig. 5.3(a) is broader due to increase in the homogeneous linewidth with temperature. But more importantly, the peak in Fig. 5.3(b) is almost perfectly symmetric. This observation is consistent with our explanation of the asymmetric peak in Fig. 5.2(b); increased phonon population, due to higher sample temperature, increases the likelihood of increase in exciton energy due to absorption of phonons, which results in a symmetrically broadened peak.

5.2.2 Population redistribution

Now we will analyze the asymmetry between the exciton relaxation and excitation processes through the evolution of the population of the excitons created with the excitation energies indicated by the horizontal lines in Figs. 5.2 and 5.3. These energies are offset by ± 0.3 meV from the excitation energy corresponding to the peak maximum. If the strong redistribution approximation is satisfied, the population redistribution for both these excitation energies should be identical. Conversely, different population redistribution of excitons created with these excitation energies would suggest that the strong redistribution approximation is not valid.

Figures 5.4(a) and 5.4(b) show the population redistribution of excitons created at excitation energies denoted by the dot-dash and solid lines, respectively, in Fig. 5.2. The spectrally-resolved change in the normalized population distribution[1] is plotted for both the excitation energies. Mathematically, the plotted quantity is

$$S_{diff,\omega'_\tau}(T,\omega_t) = S_N(\omega'_\tau, T, \omega_t) - S_N(\omega'_\tau, 0.2\,\mathrm{ps}, \omega_t) \tag{5.2}$$

where $S_{diff,\omega'_\tau}(T,\omega_t)$ is the population redistribution spectrum, S_N is the normalized 2D spectrum, and ω'_τ is the excitation energy for which the population redistribution is calculated. The emission energy equal to ω'_τ is indicated by the vertical lines in both the spectra

[1] Normalized population distribution is obtained by selecting a peak area and dividing by the average amplitude of the peak for each T. This procedure eliminates the effect of overall population decay with T, and isolates the population redistribution.

shown in Fig. 5.4.

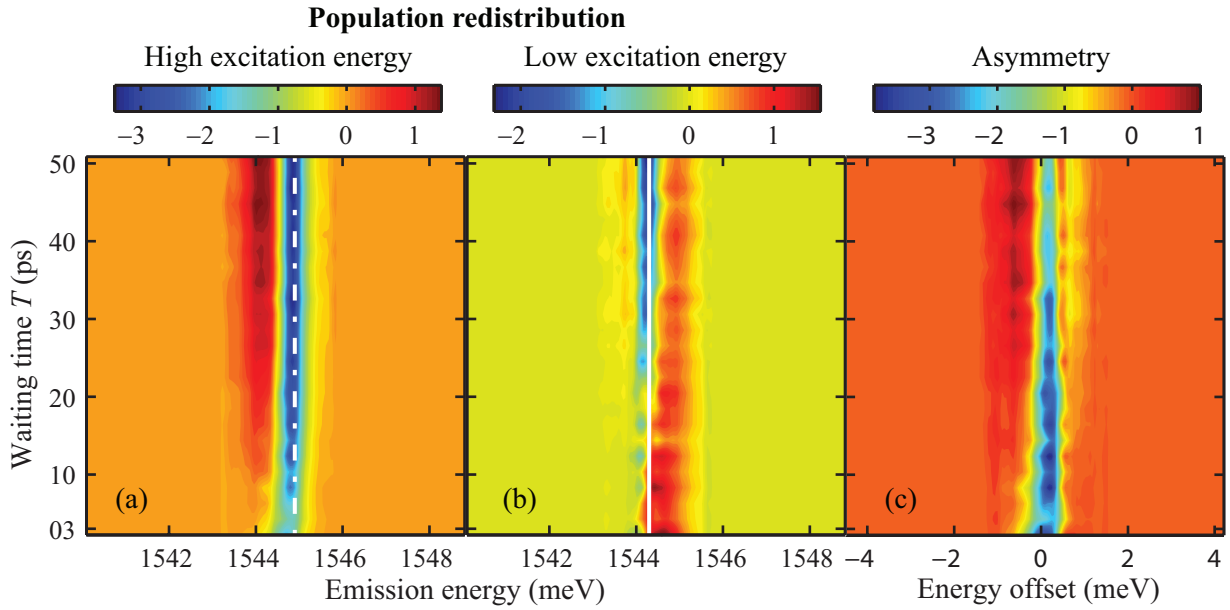

Figure 5.4: Population redistribution for (a) high excitation energy and (b) low excitation energy slices indicated in the 2D spectra in Fig. 5.2. The excitation energy is denoted by the vertical lines in (a) and (b). (c) The difference of the plots in (a) and (b). This plot highlights the asymmetry between the relaxation and excitation processes.

The plots in Figs. 5.4(a) and 5.4(b) look different in that the decrease and increase in population is significantly higher in the former spectrum. To highlight the asymmetry between these two plots, we take a difference of the two plots, which is shown in Fig. 5.4(c). One of the plots is rotated about the emission energy of the peak before calculating the difference and the horizontal axis is plotted as the energy offset from the emission energy of the peak. We would expect this plot to have values close to zero if the strong redistribution approximation valid.

The same set of plots are shown in Fig. 5.5 for the 25 K data shown in Fig. 5.3. We can clearly see that the plots shown in Figs. 5.5(a) and 5.5(b) are more symmetric than their counterparts in Fig. 5.4. This is further corroborated by the plot in Fig. 5.5(c), which has smaller values compared to the plot in Fig. 5.4(c).

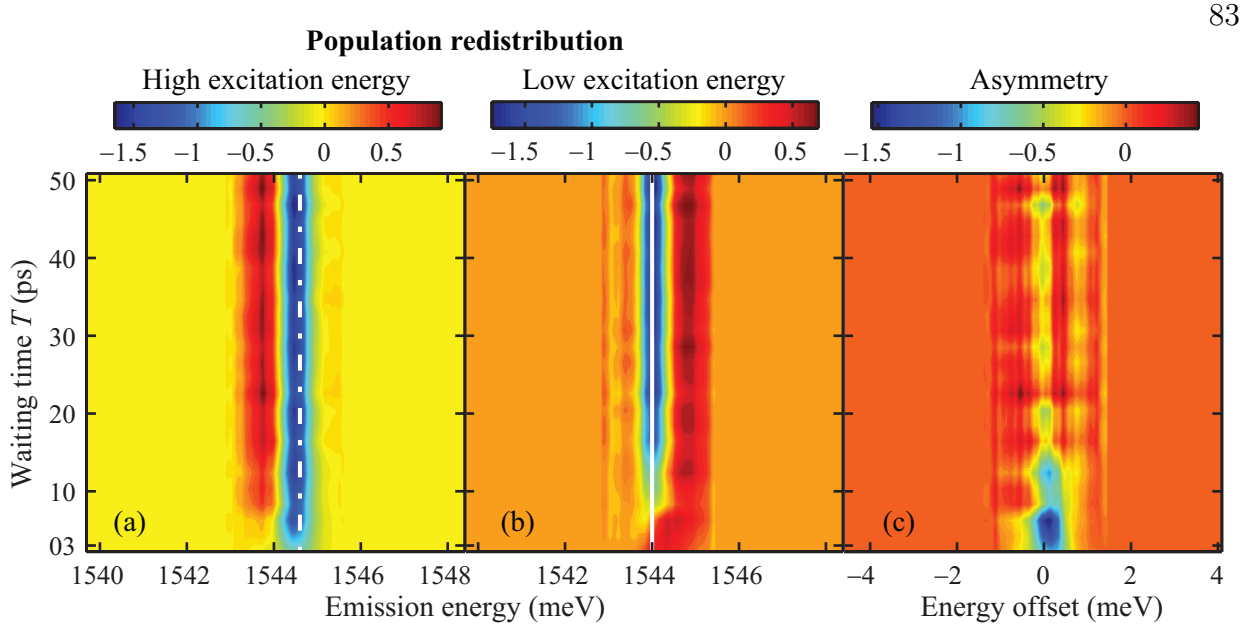

Figure 5.5: Population redistribution for (a) high excitation energy and (b) low excitation energy slices indicated in the 2D spectra in Fig. 5.3. The excitation energy is denoted by the vertical lines in (a) and (b). (c) The difference of the plots in (a) and (b). This plot highlights the asymmetry between the relaxation and excitation processes.

5.2.3 Temperature dependence

The analysis presented in Section 5.2.2 is helpful to qualitatively highlight the changes in the spectral diffusion characteristics with the sample temperatures. Even so, it merely stresses the features that were already apparent from the 2D spectra and the accompanying discussion in Section 5.2.1. Now we will use spectra similar to those in Figs. 5.4(c) and 5.5(c) to compare the validity of the strong redistribution approximation for different temperatures. We quantify the asymmetry between the exciton relaxation and excitation processes, for a given temperature, by taking the sum of the absolute value of all the points in the "Asymmetry" spectrum, which yields zero for symmetric population redistribution. This asymmetry, as a function of sample temperature, is shown in Fig. 5.6. The asymmetry values have been normalized by dividing by the value for 5 K.

We observe a fast decrease in the asymmetry parameter with an increase in the sample temperature. Furthermore, we find that, for temperatures higher than 20 K, the asymmetry

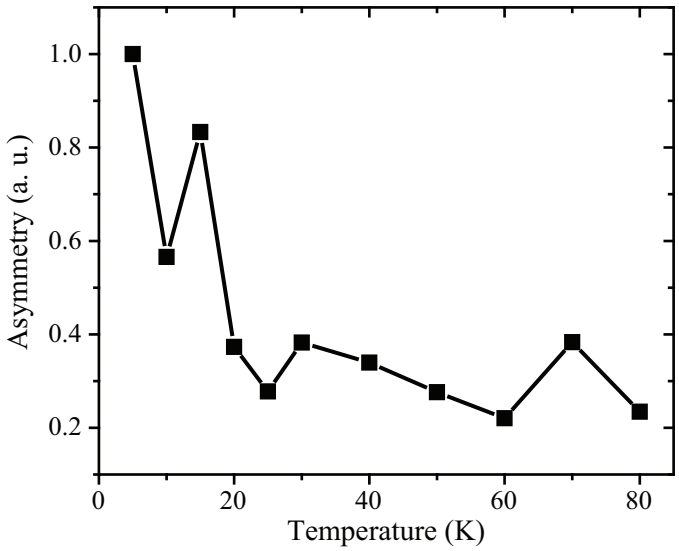

Figure 5.6: Asymmetry between the relaxation and excitation processes as a function of sample temperature. The asymmetry value is obtained by summing the absolute value of all points in the plots similar to those shown in Figs. 5.4(c) and 5.5(c) for each temperature.

value is basically independent of the sample temperature. Ideally, the normalized asymmetry quantity should go from 1 to 0 as the temperature is increased. We observe that this value only decays to $\sim 0.3 \pm 0.1$. We attribute this anomaly to experimental noise in the measured spectra, which is accentuated on taking the difference between spectra. Nevertheless, from the graph in Fig. 5.6, we infer that the strong redistribution approximation is valid for temperatures above 20 K. Thus, spectral diffusion can be quantified using the correlation function for temperatures higher than 20 K, as will be demonstrated next.

5.3 High temperature regime

We have already discussed the effect of the change in correlation function on 2D spectrum in Section 5.1. Now we will see how to use that effect to measure the correlation function from experimental data.

5.3.1 Fitting procedure

In Section 3.2, we discussed extensively the procedure to simulate 2D spectrum from time-domain TFWM signal, which is given by Eq. (5.1) including the correlation function C. Now we will match the simulated and experimental spectra to obtain the best-fit parameters through a numerical fitting procedure. Before, we describe the fitting procedure, we rewrite Eq. (5.1), in a more useful form, as

$$S_{S_I,SD}(\tau,T,t) = A(T)\mathrm{e}^{-\gamma_{01}(\tau+t)}\mathrm{e}^{-\frac{1}{2}{\sigma_{01}}^2(\tau^2+t^2-2C(T)\tau t)}\Theta(\tau)\Theta(T)\Theta(t) \tag{5.3}$$

where A is the amplitude term, which includes electric fields, dipole moments, and the signal decay with T. We show the dependence of the amplitude and correlation function on waiting time T explicitly. The variable parameters in Eq. (5.3) are – $A(T)$, γ_{01}, σ_{01}, and $C(T)$. The exciton resonance energy is directly measured from 2D spectrum, and is not varied during the fitting procedure; thus, we do not show that term in Eq. (5.3). In order to obtain meaningful value of $A(T)$, normalized signal is used in the fitting procedure. This normalized signal is related to the one given by Eq. (5.3) as

$$S_{norm}(\tau,T,t) = \frac{S_{S_I,SD}(\tau,T,t)}{\left[\int_{-\infty}^{\infty}\int_{-\infty}^{\infty} dt\, d\tau \left|\frac{S_{S_I,SD}(\tau,T,t)}{A(T)}\right|^2\right]^{1/2}}. \tag{5.4}$$

Diagonal and cross-diagonal slices from the simulated and measured 2D spectra are matched, by minimizing the sum of square of the difference between simulated and measured slices, to obtain the values of A, γ_{01}, and σ_{01}. This procedure was followed for 2D spectrum with smallest T, which in the present case was 0.2 ps. We set $C = 1$ for the first spectrum. γ_{01}, and σ_{01} are kept fixed for subsequent 2D spectra; A and C are the only variable parameters.

5.3.2 Analysis results

The plots in Fig. 5.7 show slices from the experimental and simulated spectra. The simulated spectra used the parameters obtained from the fitting procedure described in Section 5.3.1. The diagonal and cross-diagonal slices are shown in the left and right columns, respectively. The top and bottom rows show slices from spectra measured with $T = 0.2$ and 26.6 ps, respectively. An excellent match between the measured and simulated slices is obtained.

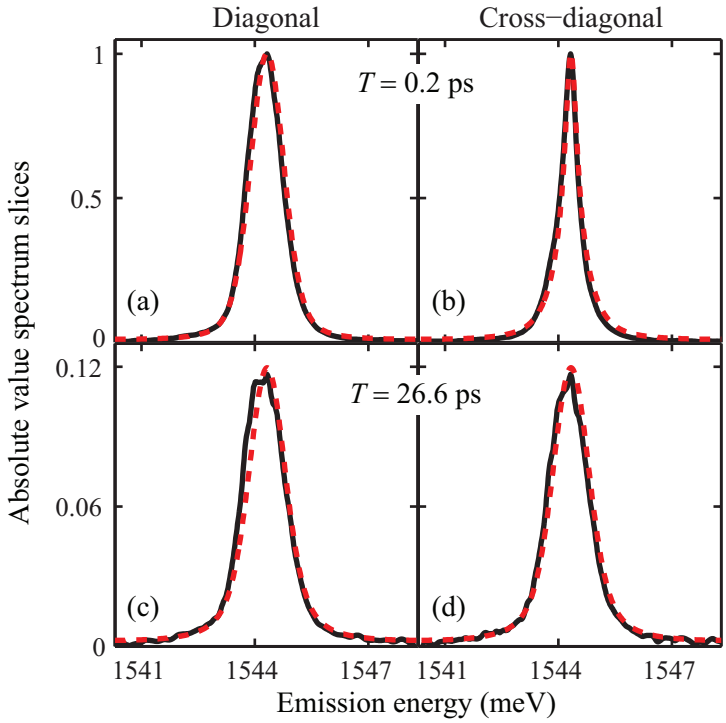

Figure 5.7: (a) Diagonal and (b) cross-diagonal slices from experimental (solid) and simulated (dashed) spectrum for $T = 0.2$ ps. (c) Diagonal and (d) cross-diagonal slices from experimental (solid) and simulated (dashed) spectrum for $T = 26.6$ ps. The simulated spectrum is obtained using the parameters obtained through the fitting procedure. The sample temperature was 25 K.

The fitting procedure is repeated for several sample temperatures from 5 – 80 K. The measured values of the correlation function as a function of the waiting time for a few temperatures are shown in Fig. 5.8 in a semi-log plot. 2D spectra were measured for

$T = 0.2 - 50.9$ ps for each temperature; a small subset of these points are shown in Fig. 5.8 to avoid the noisy points with $C < 0.1$. As expected, the correlation function decays with increasing waiting time and the rate of decay increases with sample temperature. An interesting finding is that the decay of the correlation function is not exponential with the waiting time. This deviation from exponential decay is most apparent for 20 K and becomes progressively less apparent as the sample temperature is increased. We conclude that even though strong-redistribution approximation is valid for temperatures higher than 20 K, the Gauss-Markov approximation is not valid.

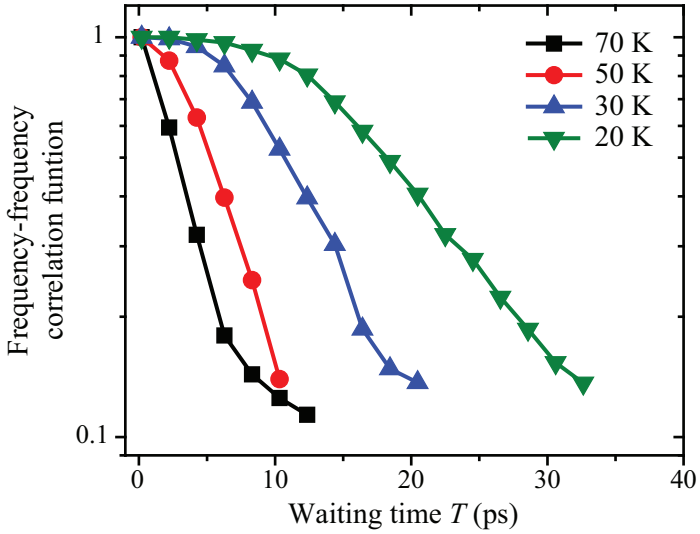

Figure 5.8: Decrease in the normalized frequency-frequency correlation function with waiting time for different sample temperatures on a semi-log scale.

Next we present the measured values for the amplitude term A as a function of the waiting time for various sample temperatures, which are shown in Fig. 5.9. The amplitude term denotes the total exciton population. There are several interesting features of the evolution of signal amplitude with the waiting time. Firstly, all the curves are non-exponential. This suggests that our treatment of population decay in Chapter 3 is not valid for excitons. Even more surprising is the non-monotonic population evolution for 50 and 70 K – there is a sharp fall for small T followed first by an increase and then a slow decay. This non-

monotonic behavior is reproduced consistently for all the sample temperatures above 50 K, and suggests an increase in population with time.

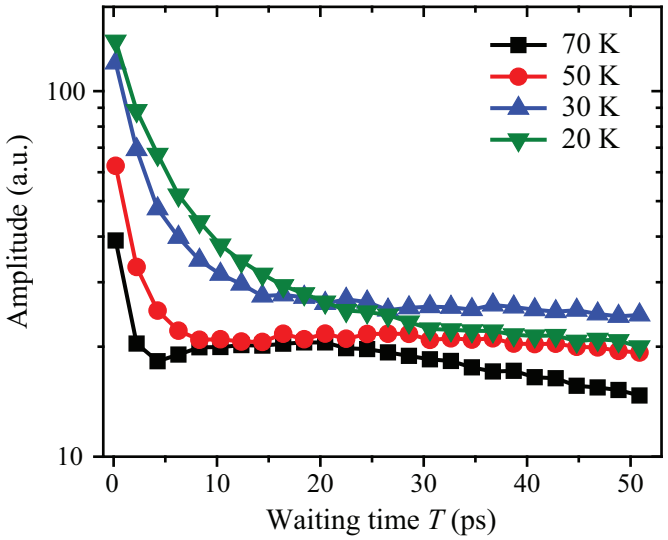

Figure 5.9: Variation in total signal strength with the waiting time for various sample temperatures. Notice the non-monotonic behavior for 50 K and 70 K.

The non-monotonic evolution is not an artifact of our fitting procedure, and is reproduced from rephasing zero-quantum scans, which are discussed in Appendix D. We do not understand this unexpected increase in signal strength. Exciton spin-flip [131] and creation of excitons from electron-hole pairs created in the continuum are a couple of probable causes for this unexpected behavior.

In this chapter we have shown that the usual description of spectral diffusion based on the correlation function and its exponential decay does not work for excitons in semiconductor QWs. At low temperatures, the strong redistribution approximation is not valid, which means spectral diffusion cannot be described through the correlation function. This approximation is satisfied for high (> 20 K) temperatures. For these temperatures the correlation function is measured through a numerical fitting procedure, which, to the best of our knowledge, has been demonstrated for the first time. The decay of this correlation function is non-exponential, which violates the Gauss-Markov approximation usually used to model

spectral diffusion. In addition to the novel properties of spectral diffusion of excitons in QWs, our results also show interesting, non-monotonic evolution of TFWM signal with the waiting time for temperatures > 50 K. Further work is needed to explain this phenomenon.

Chapter 6

Excitons as Interacting Bosons

One of the puzzles in early TFWM experiments was the dependence of signal decay rate on the polarization of the excitation pulses. It was observed that the TFWM signal decays faster for the cross-linear polarization scheme than for the co-circular and co-linear polarization schemes [77, 78, 79]. The contribution of disorder-mediated coupling [132] and multi-exciton correlations through bound and unbound two-exciton states to the TFWM signal [133] have been previously used to explain this phenomenon. However, these models cannot reproduce the correct TFWM signal phase [13].

Exciton physics in QWs is generally modeled using a two-level system, as has been done so far in this work. Many-body effects can be added phenomenologically to the OBEs describing such a system and solved numerically [5]. A more rigorous description of excitons is possible through the semiconductor Bloch equations [54]. Both methods of including inter-excitonic interactions are computationally intensive, which makes it impractical to use these methods to quantify exciton-exciton interaction strengths.

In this chapter, we discuss modeling excitons as interacting bosons. First we will introduce the theoretical framework; we will show that exciton-exciton interactions can be separated into intra- and inter-mode interactions. Next we will show that the polarization dependent dephasing rate as well as EIS-modified signal phase [13] are a direct consequence of the bosonic nature of excitons. Due to the significant reduction in computational complexity, we can fit simulation results to experimental data and quantify exciton-exciton interactions.

Also, we highlight how the signal in a non-linear optics experiment, such as TFWM, is affected by the bosonic character of the system being studied. After establishing the validity of this model, we will separate and quantify the intra- and inter-mode interactions through exciton-density-dependent measurements.

6.1 Bosonic model for excitons

6.1.1 Interactions between same-spin excitons

For the sake of simplicity, we consider excitons with the same spin. We describe excitons as a harmonic ladder of states. Inter-exciton interactions are introduced through anharmonic terms in the Hamiltonian [134, 135]. The Hamiltonian for multiple exciton modes can be written as

$$H_{tot} = \hbar \sum_{i=1}^{N} \omega_i n_i + \sum_{i=1}^{N} \widetilde{\Delta}_i n_i (n_i - 1) + \sum_{i,j=1,\ i\neq j}^{N} \widetilde{\Delta}_{ij} n_i n_j \tag{6.1}$$

where i, j denote exciton modes, N is the total number of available modes, $\hbar\omega_i$ is the energy of an isolated exciton in mode i, n_i is occupation number for mode i, and $\widetilde{\Delta}_i$ and $\widetilde{\Delta}_{ij}$ are the intra- and inter-mode interaction energies, respectively. The multiple modes could be due to different in-plane exciton wavevector or the different states due to the inhomogeneity. Assuming constant intra- and inter-mode interaction energies of $\frac{1}{2}\Delta$ and Δ', respectively, Eq. (6.1) can be simplified to obtain the Hamiltonian for a single exciton mode

$$H_i = \hbar\omega_i n_i + \frac{1}{2}\Delta n_i(n_i - 1) + \Delta' N_{ex} n_i \tag{6.2}$$

where $N_{ex} = \sum_{j=1;\ j\neq i}^{N} n_j$ is approximately the total number of excitons. Under the mean-field approximation, we consider the system to be defined by the Hamiltonian in Eq. (6.2), which we can rewrite by explicitly removing the mode-index i

$$\begin{aligned} H &= (\hbar\omega_0 + \Delta' N_{ex})n + \frac{1}{2}\Delta n(n-1) \\ &= \hbar\omega n + \frac{1}{2}\Delta n(n-1) \end{aligned} \tag{6.3}$$

where $\hbar\omega_0$ is the resonance energy of a non-interacting exciton. The density dependent transition energy of the $|0\rangle \leftrightarrow |1\rangle$ transition is

$$\hbar\omega = \hbar\omega_0 + \Delta' N_{ex} \ . \tag{6.4}$$

The energy scheme shown in Fig. 6.1(a) represents the Hamiltonian given by Eq. (6.3) showing the ground $|0\rangle$, single exciton $|1\rangle$, and two-exciton $|2\rangle$ states. The higher lying states are not shown because they do not contribute to the TFWM signal in the $\chi^{(3)}$ regime, and are therefore not ordinarily needed if pulse energies are kept sufficiently low during an experiment. In addition to the energy shift, exciton-exciton interactions result in increased dephasing rates, which are added phenomenologically. Intra-mode interactions result in a difference of ξ in the dephasing rates between the $|0\rangle \leftrightarrow |1\rangle$ and $|1\rangle \leftrightarrow |2\rangle$ transitions. Similar to the relation in Eq. (6.4), inter-mode interactions results in an exciton-density dependent dephasing rate of the $|0\rangle \leftrightarrow |1\rangle$ transition

$$\gamma = \gamma_0 + \xi' N_{ex} \tag{6.5}$$

where γ_0 is the dephasing rate of the $|0\rangle \leftrightarrow |1\rangle$ transition for an unexcited sample. The aforementioned energy shift terms (Δ and Δ') and dephasing rate terms (ξ and ξ') are equivalent of the many-body terms EIS and EID, respectively [134]. The obvious difference is that we have now separated the EIS and EID terms into inter- and intra-mode interactions. Later on in this chapter, we will quantify all of these terms.

The transition dipole moments for the $|0\rangle \leftrightarrow |1\rangle$ and $|1\rangle \leftrightarrow |2\rangle$ are μ_1 and μ_2, respectively. In general, these are related as

$$\mu_2 = \sqrt{2}\mu_1 - \mu' \tag{6.6}$$

where the factor of $\sqrt{2}$ results from the bosonic nature and μ' accounts for phase-space filling (PSF) effect due to the fermionic nature of electrons and holes. From experimental measurements, we find that $\mu' \approx 0$. Thus, we ignore the PSF effect and set $\mu_2 = \sqrt{2}\mu_1$.

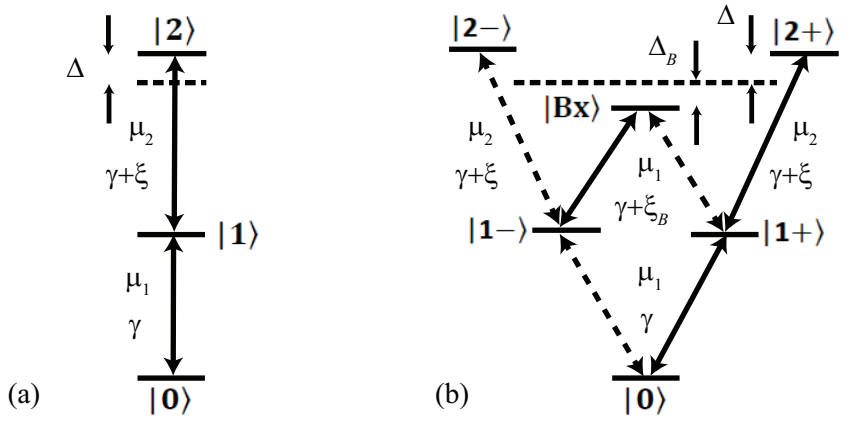

Figure 6.1: Energy level scheme for excitons as harmonic oscillators for excitons with (a) the same spin and (b) both ± 1 spins. (a) Shows the ground $|0\rangle$, single exciton $|1\rangle$, and two-exciton $|2\rangle$ states where the excitons are implicitly assumed to have the same spin. (b) Shows the ground $|0\rangle$, single exciton $|1\pm\rangle$, two-exciton $|2\pm\rangle$ and biexciton $|\mathrm{Bx}\rangle$ states. Optical transitions are indicated by arrows. The solid and dashed arrows indicate transitions excited by σ_+ and σ_- polarized light, respectively, in (b). The transition dipole moments (μ_1 and μ_2) and dephasing rates (γ, $\gamma+\xi$ and $\gamma+\xi_B$) are indicated next to the arrows. Note that $\mu_2 = \sqrt{2}\mu_1$. The dashed line indicates the energy of the two-exciton states in the absence of inter-exciton interactions. The same spin two-exciton states, $|2\rangle$ in (a) and $|2\pm\rangle$ in (b), are blue shifted by interaction energy Δ. The bound biexciton state, $|\mathrm{Bx}\rangle$ in (b), is red shifted by binding energy Δ_B and states

6.1.2 Interactions between opposite-spin excitons

We have described the same-spin exciton as bosons. Now we extend this model to include excitons of opposite spins and biexcitons, which are bound opposite-spin exciton pairs. The combined Hamiltonian for excitons with both ± 1 spins, based on Eq. (6.3), can be written as

$$H = \hbar\omega \sum_{i=\pm} n_i + \frac{1}{2}\Delta \sum_{i=\pm} n_i(n_i - 1) + \Delta_B n_+ n_- \tag{6.7}$$

where the index i is now used to denote exciton-spin and Δ_B is the biexciton binding energy. This Hamiltonian is represented by the energy level scheme shown in Fig. 6.1(b). As in Fig. 6.1(a), we only show the energy levels up to the two-exciton states. The optical transitions that are possible using σ_+ and σ_- polarized lights are indicated by solid and dashed arrows, respectively. The spin of the exciton states is explicitly indicated. In addition to the binding

energy, the interactions between opposite-spin excitons results in the change in dephasing rate of the $|1\pm\rangle \leftrightarrow |\mathrm{Bx}\rangle$ transitions with respect to that of the $|0\rangle \leftrightarrow |1\pm\rangle$ transitions by ξ_B.

6.2 Polarization dependence

In the previous section, we presented a model to treat excitons as interacting bosons. Now we will test the validity of this model by using it to analyze polarization-dependent 2DCS measurements. We have performed experiments for the co-circular, cross-linear and co-linear polarization schemes. All the transition shown in Fig. 6.1 are accessible through circularly polarized light. Thus, we need to be able to model the TFWM signal for linearly-polarized light using the circularly-polarized transitions shown in Fig. 6.1. We will discuss this procedure next.

6.2.1 Linear and circular bases

We begin by listing the Feynman diagrams for all possible polarization schemes in the circular basis. These Feynman diagrams are labeled I – VII in Fig. 6.2. The first interaction in all these diagrams are with σ_+ polarized light. The polarization of each pulse and the radiated signal is indicated next to the arrows in each Feynman diagram. Feynman diagrams I – IV involve only the $|0\rangle \leftrightarrow |1\pm\rangle$ transitions. Feynman diagram V includes contributions from $|0\rangle \leftrightarrow |1+\rangle$ and $|1+\rangle \leftrightarrow |2+\rangle$ transitions. Another identical set of Feynman diagrams exist where the σ_+ polarized pulses are replaced with σ_- polarized pulses and vice-versa, which have not been shown. Since these diagrams essentially include interactions identical to those in the diagrams shown in Fig. 6.2, we will use the labels I′ – VII′ for these diagrams. We will discuss the origin of TFWM signal for the co-circular, cross-linear and co-linear polarization schemes using these fourteen Feynman diagrams.

To calculate the FWM signal for linearly polarized excitation pulses, we use the rela-

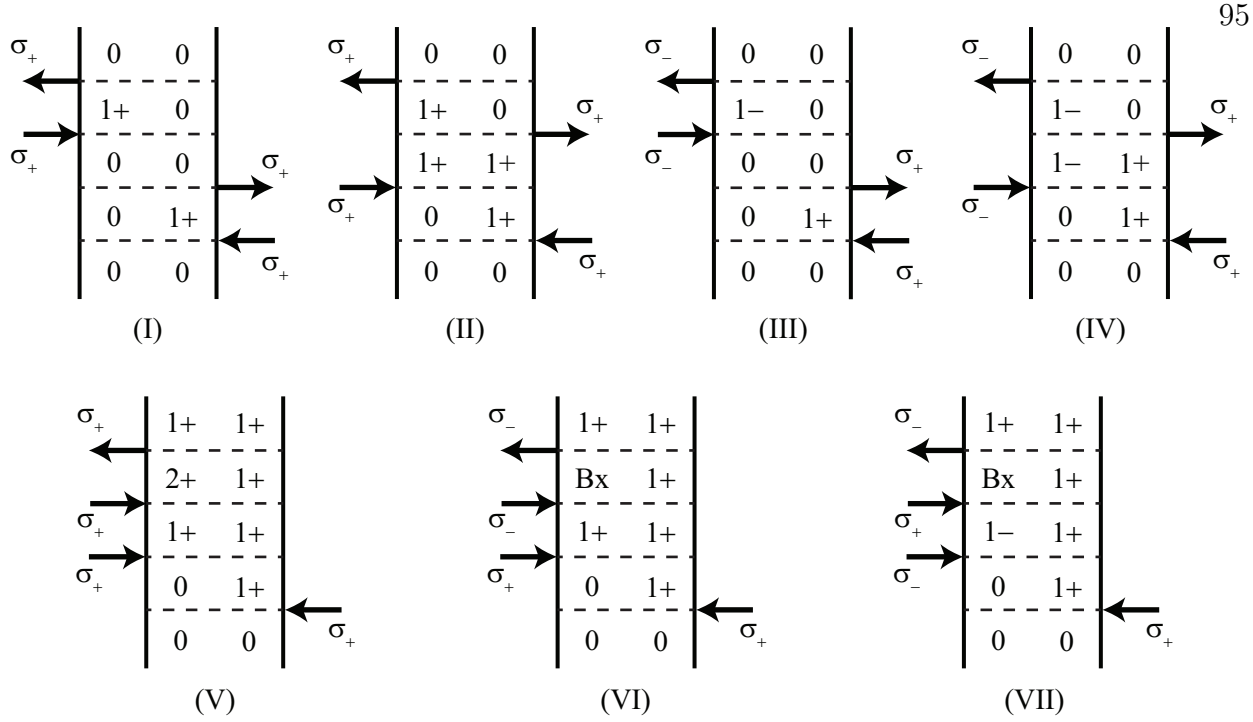

Figure 6.2: Feynman diagrams (I – VII) denoting the dipole allowed quantum pathways that contribute to TFWM signal for the energy level scheme shown in Fig. 6.1(b). All possible excitation pulse polarizations in the circular basis have been considered with σ_+ polarization of the first pulse. Feynman diagrams (I – IV) involve the transitions between the ground and one-exciton levels only, while Feynman diagrams (V – VII) also involve transitions between one-exciton and two-exciton levels. Another identical set of diagrams can be written down by swapping the σ_+ and σ_- polarized pulses, which are not shown. These diagrams will be referred to by numbers I′ – VII′ indicating the corresponding diagram that has been shown.

tionship between linear and circular polarizations:

$$\sigma_+ = \frac{1}{\sqrt{2}}\,(X + iY) \qquad\qquad \sigma_- = \frac{1}{\sqrt{2}}\,(X - iY) \tag{6.8}$$

where $\sigma_\pm$ denote orthogonal circular polarizations and X and Y denote orthogonal linear polarizations. The relations in Eq. (6.8) can be re-written as

$$X = \frac{1}{\sqrt{2}}\,(\sigma_+ + \sigma_-) \qquad\qquad Y = -\frac{i}{\sqrt{2}}\,(\sigma_+ - \sigma_-)\ . \tag{6.9}$$

We can write the contribution of each Feynman diagram to the TFWM signal for each polarization scheme using the relations in Eqs. (6.8) and (6.9). First, we consider only the strength, phase and the polarization of the TFWM signal, which are collectively

Feynman diagram	Co-circular	Cross-linear	Co-linear
I	${\mu_1}^4\sigma_+$	$-\left(\frac{1}{2\sqrt{2}}\right){\mu_1}^4\sigma_+$	$\left(\frac{1}{2\sqrt{2}}\right){\mu_1}^4\sigma_+$
I′	0	$-\left(\frac{1}{2\sqrt{2}}\right){\mu_1}^4\sigma_-$	$\left(\frac{1}{2\sqrt{2}}\right){\mu_1}^4\sigma_-$
II	${\mu_1}^4\sigma_+$	$-\left(\frac{1}{2\sqrt{2}}\right){\mu_1}^4\sigma_+$	$\left(\frac{1}{2\sqrt{2}}\right){\mu_1}^4\sigma_+$
II′	0	$-\left(\frac{1}{2\sqrt{2}}\right){\mu_1}^4\sigma_-$	$\left(\frac{1}{2\sqrt{2}}\right){\mu_1}^4\sigma_-$
III	0	$\left(\frac{1}{2\sqrt{2}}\right){\mu_1}^4\sigma_-$	$\left(\frac{1}{2\sqrt{2}}\right){\mu_1}^4\sigma_-$
III′	0	$\left(\frac{1}{2\sqrt{2}}\right){\mu_1}^4\sigma_+$	$\left(\frac{1}{2\sqrt{2}}\right){\mu_1}^4\sigma_+$
IV	0	$\left(\frac{1}{2\sqrt{2}}\right){\mu_1}^4\sigma_-$	$\left(\frac{1}{2\sqrt{2}}\right){\mu_1}^4\sigma_-$
IV′	0	$\left(\frac{1}{2\sqrt{2}}\right){\mu_1}^4\sigma_+$	$\left(\frac{1}{2\sqrt{2}}\right){\mu_1}^4\sigma_+$
V	$-(\mu_1\mu_2)^2\sigma_+$	$\left(\frac{1}{2\sqrt{2}}\right)(\mu_1\mu_2)^2\sigma_+$	$-\left(\frac{1}{2\sqrt{2}}\right)(\mu_1\mu_2)^2\sigma_+$
V′	0	$\left(\frac{1}{2\sqrt{2}}\right)(\mu_1\mu_2)^2\sigma_-$	$-\left(\frac{1}{2\sqrt{2}}\right)(\mu_1\mu_2)^2\sigma_-$
VI	0	$-\left(\frac{1}{2\sqrt{2}}\right){\mu_1}^4\sigma_-$	$-\left(\frac{1}{2\sqrt{2}}\right){\mu_1}^4\sigma_-$
VI′	0	$-\left(\frac{1}{2\sqrt{2}}\right){\mu_1}^4\sigma_+$	$-\left(\frac{1}{2\sqrt{2}}\right){\mu_1}^4\sigma_+$
VII	0	$-\left(\frac{1}{2\sqrt{2}}\right){\mu_1}^4\sigma_-$	$-\left(\frac{1}{2\sqrt{2}}\right){\mu_1}^4\sigma_-$
VII′	0	$-\left(\frac{1}{2\sqrt{2}}\right){\mu_1}^4\sigma_+$	$-\left(\frac{1}{2\sqrt{2}}\right){\mu_1}^4\sigma_+$

Table 6.1: Contributions to the transient four-wave mixing signal from the Feynman diagrams in Fig. 6.2 for the co-circular, cross-linear and co-linear polarization schemes.

shown for each Feynman diagram for different polarization schemes. We have considered σ_+ polarization for the co-circular polarization scheme. For the cross-linear and co-linear

polarization schemes, we have assumed XYYX and XXXX polarizations, respectively.

In addition to the contributions of each Feynman diagram listed in Table 6.1, we need to include the excitation and emission frequencies for each diagram. We note that all the Feynman diagrams have the same excitation energy $\hbar\omega$ corresponding to the transition energy of the $|0\rangle \leftrightarrow |1\pm\rangle$ transitions. Also, all the diagrams decay with the same dephasing rate γ during delay τ. However, based on the emission energies and dephasing rates, the Feynman diagrams can be separated into the following groups:

(1) The diagrams I – IV and I′ – IV′ with the emission energy equal to the excitation energy $\hbar\omega$. These diagrams decay with dephasing rate γ during delay t.

(2) The diagrams V and V′, which have the emission energy of $\hbar\omega + \Delta$ corresponding to the $|1\pm\rangle \leftrightarrow |2\pm\rangle$ transitions. These diagrams decay with dephasing rate $\gamma + \xi$ during delay t.

(3) The remaining diagrams with the emission energy of $\hbar\omega - \Delta_B$ corresponding to the $|1\pm\rangle \leftrightarrow |\mathrm{Bx}\rangle$ transitions. These diagrams decay with dephasing rate $\gamma + \xi_B$ during delay t.

Now we have all the information needed to write down the TFWM signal for each polarization scheme. We use the relation $\mu_2 = \sqrt{2}\mu_1$ and those in Eq. (6.9) to obtain the following TFWM signals:

$$S_{CoCir}(\tau,t) = A_{CoCir}\,\mathrm{e}^{-\gamma(\tau+t)}\,\mathrm{e}^{-\frac{1}{2}\sigma^2(\tau-t)^2}\left(1-\mathrm{e}^{(i\Delta-\xi)t}\right) \tag{6.10}$$

$$S_{XLin}(\tau,t) = \mathrm{e}^{-\gamma(\tau+t)}\left(A1_{XLin}\,\mathrm{e}^{-\frac{1}{2}\sigma^2(\tau-t)^2}\,\mathrm{e}^{(i\Delta-\xi)t} - A2_{XLin}\,\mathrm{e}^{-\frac{1}{2}(\sigma\tau-\sigma_B t)^2}\,\mathrm{e}^{(-i\Delta_B-\xi_B)t}\right) \tag{6.11}$$

$$S_{CoLin}(\tau,t) = \mathrm{e}^{-\gamma(\tau+t)}\left[A1_{CoLin}\,\mathrm{e}^{-\frac{1}{2}\sigma^2(\tau-t)^2}\left(2-\mathrm{e}^{(i\Delta-\xi)t}\right) - A2_{CoLin}\,\mathrm{e}^{-\frac{1}{2}(\sigma\tau-\sigma_B t)^2}\,\mathrm{e}^{(-i\Delta_B-\xi_B)t}\right] \tag{6.12}$$

where the subscripts $CoCir$, $XLin$ and $CoLin$ are used for the co-circular, cross-linear and co-linear polarization schemes, respectively. These signals are written as a function of delays

t and τ since we will only consider one-quantum rephasing spectra. Signal amplitudes are denoted by A; different amplitudes are used for the different polarization schemes. Separate exciton and biexciton signal amplitudes are used. The parameters σ and σ_B describe the inhomogeneous broadening for the $|0\rangle \leftrightarrow |1\pm\rangle$ and $|1\pm\rangle \leftrightarrow |\mathrm{Bx}\rangle$ transitions, respectively. Equal inhomogeneities for the $|0\rangle \leftrightarrow |1\pm\rangle$ and $|1\pm\rangle \leftrightarrow |2\pm\rangle$ transitions are assumed. All the other parameters are shown in Fig. 6.1 and explained earlier. We do not show the exciton resonance energy explicitly.

We have laid down the theoretical background to understand the dependence of the TFWM signal on the polarization scheme. The physical consequence of the above equations will be discussed in detail with the experimental results, which will be discussed next. We have measured rephasing one-quantum 2D spectra for the (001)-oriented GaAs QWs described in Section 2.9.1. The experiments were performed with $\sim$ 200 fs pulses generated by a mode-locked Ti:sapphire oscillator. The delay between pulses B and C was kept constant at 300 fs to ensure correct time-ordering. On average an exciton density of $\sim 10^{10}$ cm^{-2} per pulse per QW was excited. The sample was kept at a temperature of 10 K in a sample-in-vapor flow cryostat.

6.2.2 Co-circular polarization scheme

We will discuss the experimental results for the co-circular polarization scheme first. The $|\mathrm{Bx}\rangle$ state does not contribute to the signal for this polarization scheme [117]. A measured absolute value 2D spectrum for co-circular polarization scheme is shown in Fig. 6.3(a), which comprises a single peak labeled P1. Figure 6.3(c) shows the real part of the spectrum shown in Fig. 6.3(a); the signal phase is obtained through the SRPP technique discussed in Section 3.3.2. The peak in Fig. 6.3(c) has a dispersive lineshape, which has been previously attributed to EIS through numerical simulations [13].

We simulate the 2D spectra from the TFWM signal in Eq. (6.10). It should be noted that for $\Delta, \xi = 0$ both the terms in the parenthesis cancel each other exactly and there is no

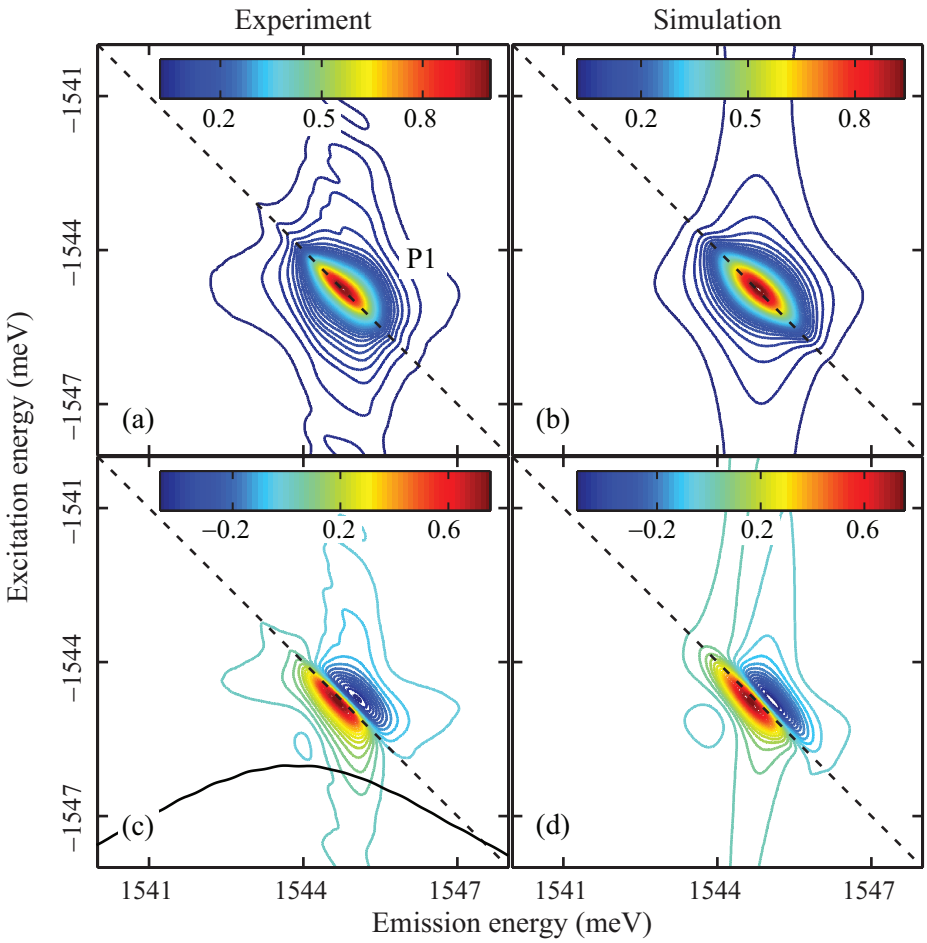

Figure 6.3: Measured (a) absolute value and (c) real part 2D spectra for the co-circular polarization scheme. The corresponding simulated spectra using best-fit parameter values are shown in (b), and (d), respectively. The peak is labeled P1 in (a). The excitation spectrum is shown as the solid line in (c).

TFWM signal, as expected from a perfectly bosonic system [136]. If the above equality is not satisfied, however, this cancellation is not perfect and a TFWM signal results. Specifically, for $\Delta > 0$, the real part of the signal comprises a positive and a negative peak shifted along the emission energy axis. The interference between these peaks results in a peak shape similar to the dispersive peak in Fig. 6.3(c) for small Δ ($< \gamma$). Such a lineshape is not obtained for a two-level system, which yields a single positive peak, as shown in Section 3.2.1.

We perform a fitting procedure similar to the one outlined in Section 5.3.1. The

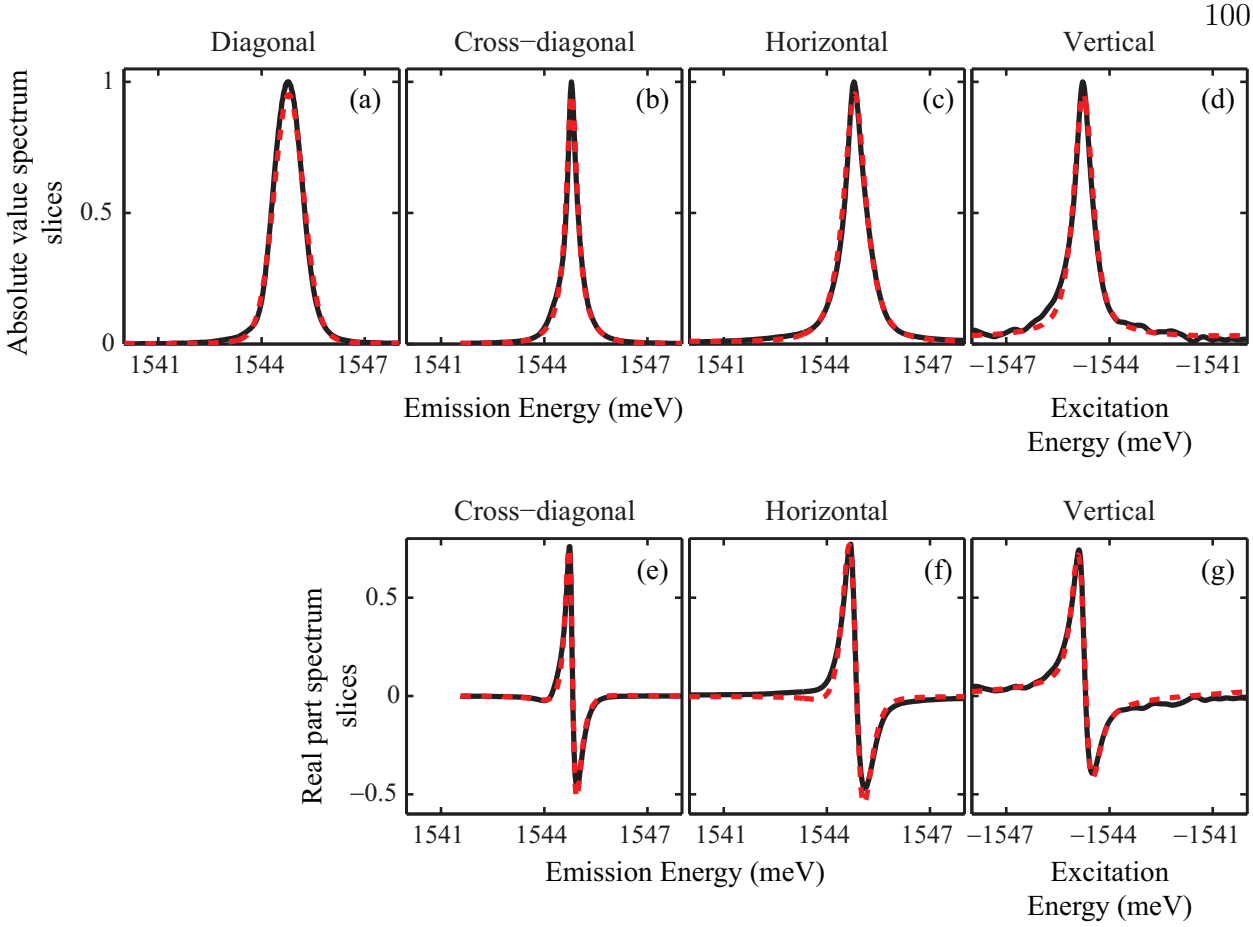

Figure 6.4: Experimental and simulation results for the slices used in the fitting procedure for the co-circular polarization scheme are shown in solid black and dashed red lines, respectively. The slices are taken through the maximum of the peak P1 shown in Fig. 6.3(a). The top and bottom rows shows the slices taken from the absolute value (Fig. 6.3(a)) and real part (Fig. 6.3(c)) spectra, respectively. The particular slice is indicated by the label above each plot.

simulated absolute value and real part spectra, using the best-fit parameter values, are shown in Figs. 6.3(b) and 6.3(d), respectively. We obtain an excellent match between the measured and simulated spectra for the following best-fit parameters: $\sigma = 383 \pm 2$ μeV, $\gamma = 191 \pm 3$ μeV, $\Delta = 13 \pm 10$ μeV, and $\xi = 6 \pm 6$ μeV. The good agreement between the simulated and measured spectra is also apparent in the slices used in the fitting procedure, which are shown in Fig. 6.4. The experiment and fitting procedure was repeated five times and we report the statistical standard deviation in the parameters values as the error. As

discussed earlier, the dispersive lineshape in Fig. 6.3(c) is a consequence of $\Delta > 0$. The measured dephasing rate γ is significantly different than that obtained by fitting the diagonal and cross-diagonal slices of absolute value spectrum to lineshapes obtained by considering exciton as a two-level system (102 ± 1 μeV) [104].

6.2.3 Cross-linear polarization scheme

We will now discuss results from 2DCS experiment performed with the cross-linear polarization scheme. Figure 6.5(a) shows the measured absolute value 2D spectrum for this polarization scheme. We see two distinct peaks in the spectrum – P2 and P3. The peak P3 is red-shifted, along the emission energy axis, with respect to peak P2 due to the biexciton binding energy. The relevant TFWM signal is given by Eq. (6.11); the first and second terms of the equation result in the peaks P2 and P3, respectively. The peak P3 is tilted with respect to the diagonal line, as indicated by the solid black line through it. This tilt is due to energy dependent biexciton binding energy and can be accounted for by different inhomogeneous widths for the $|0\rangle \leftrightarrow |1\pm\rangle$ and $|1\pm\rangle \leftrightarrow |\mathrm{Bx}\rangle$ transitions [118].

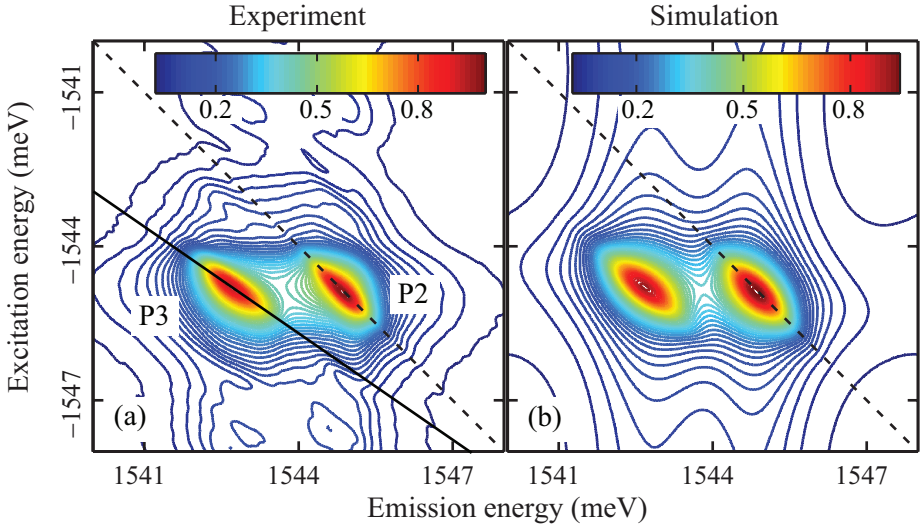

Figure 6.5: (a) Measured absolute value 2D spectrum for the cross-linear polarization scheme. (b) The corresponding simulated spectra using best-fit parameter values.The different peaks are labeled P2 and P3.

Although Eq. (6.11) results in two peaks, it does not indicate the correct relative phase between the two peaks. Thus, we add an ad-hoc phase term $e^{i\phi}$ to Eq. (6.11) and obtain

$$S_{XLin}(\tau,t) = e^{-\gamma(\tau+t)}\left(A1_{XLin}\, e^{-\frac{1}{2}\sigma^2(\tau-t)^2}\, e^{(i\Delta-\xi)t} - A2_{XLin}\, e^{i\phi}\, e^{-\frac{1}{2}(\sigma\tau-\sigma_B t)^2}\, e^{(-i\Delta_B-\xi_B)t}\right). \tag{6.13}$$

We match the slices from the 2D spectra simulated using Eq. (6.13) to the slices from the experimentally measured spectra. The variable parameters for this fitting procedure are – $A1_{XLin}$, $A2_{XLin}$, ϕ, Δ_B, and ξ_B. The other parameters are fixed to those obtained for the co-circular polarization scheme. Different inhomogeneous widths during delays τ and t result in a peak that is tilted with respect to the diagonal line. Thus, the relative tilt between the two peaks gives the ratio between σ/σ_B, which is used to fix $\sigma_B = 467 \pm 5$ μeV. The best-fit parameter values are – $\Delta_B = 2.099 \pm 0.016$ meV, and $\xi_B = 12 \pm 8$ μeV. The simulated spectrum from the parameter values obtained through the fitting procedure is shown in Fig. 6.5(b). The excellent match between theory and experiment is also highlighted by the slices shown in Fig. 6.6.

The horizontal slices in Figs. 6.6(c) and 6.6(g) indicate a weak peak between the two prominent peaks. Our model does not include that peak, and results in the incorrect phase between peaks P2 and P3, which is compensated by the ad-hoc phase term to some extent.

6.2.4 Co-linear polarization scheme

Next we will discuss at the experimental results obtained for the co-linear polarization scheme. The absolute value and real part 2D spectra for this scheme are shown in Figs. 6.7(a) and 6.7(c). The spectrum exhibits two peaks, which are labeled P4 and P5 in Fig. 6.7(a). Although the positions of these peaks are similar to those of P2 and P3 in Fig. 6.5(a), the relative strengths of the two peaks are very different. Also, the real part of peak P4 in Fig. 6.7(c) has a distinctive dispersive character similar to that in Fig. 6.3(c) for the co-circular polarization scheme.

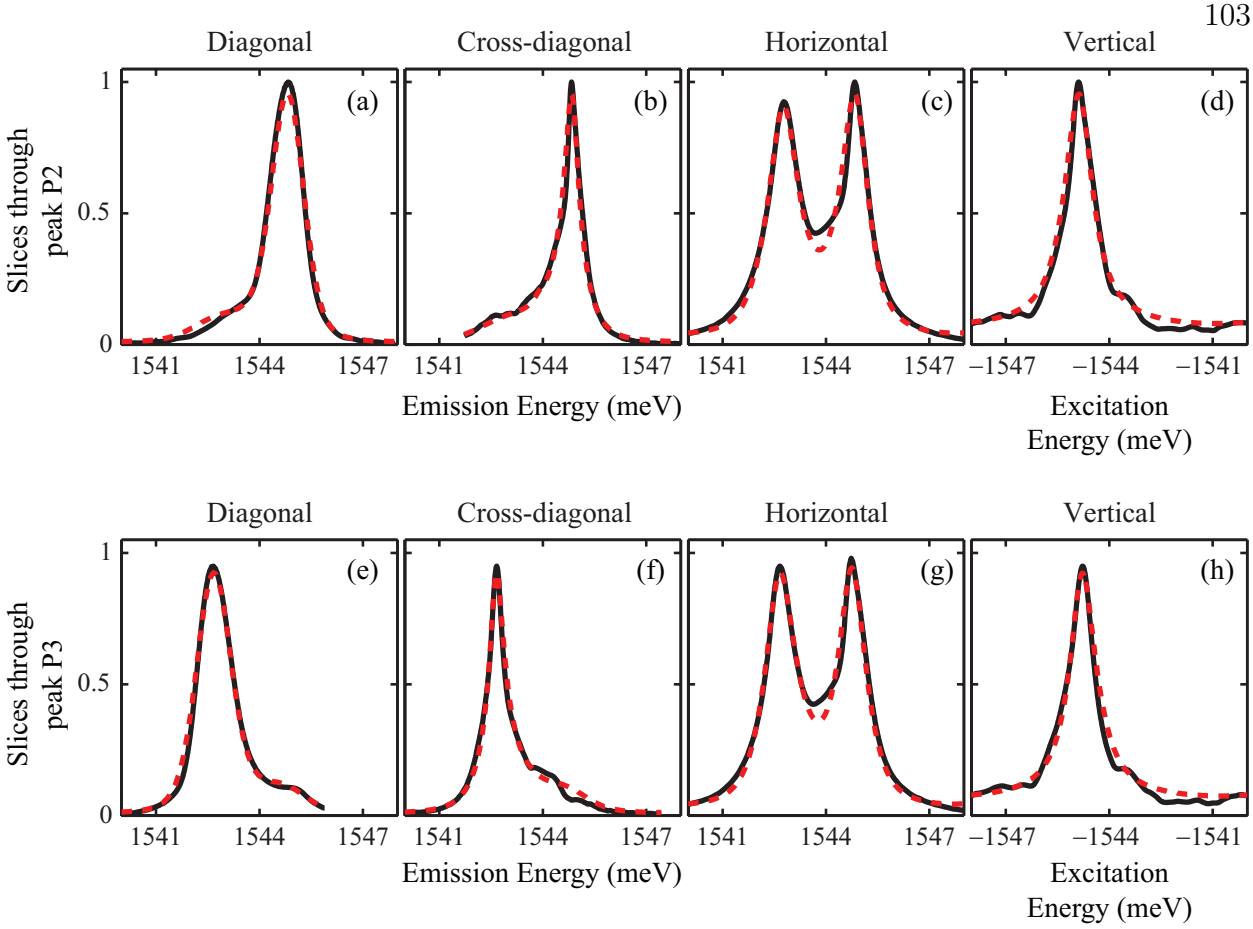

Figure 6.6: Experimental and simulation results for the slices used in the fitting procedure for the cross-linear polarization scheme are shown in solid black and dashed red lines, respectively. The slices are taken through the maximum of the peaks P2 and P3 in Fig. 6.5(a). The top and bottom rows shows the slices taken for peaks P2 and P3, respectively. The particular slice is indicated by the label above each plot.

The first and second terms, in the square brackets, in Eq. (6.12) give rise to peaks P4 and P5, similar to the situation for the cross-linear polarization scheme. The first of these terms looks similar to the TFWM signal in Eq. (6.10) for the co-circular polarization scheme. A key difference, however, is a ratio of two between the two parts of this term. As a result, the real part of the 2D spectrum obtained from Eq. (6.12) does not give a dispersive peak. This anomaly probably arises due to our simplistic treatment of density dependent resonance energies and dephasing rates given by Eqs. (6.4) and (6.5). Specifically, the density-dependent terms give rise to additional signal terms, which need to be calculated

numerically [5]. The model we have presented clearly does not capture this feature and results in the aforementioned anomaly. Since we find that the peak shape for the co-linear and co-circular polarizations are the same, we modify the first term in Eq. (6.12) to be similar to that in Eq. (6.10). The modified TFWM signal for the co-linear polarization is

$$S_{CoLin}(\tau,t) = \mathrm{e}^{-\gamma(\tau+t)}\left[A1_{CoLin}\,\mathrm{e}^{-\frac{1}{2}\sigma^2(\tau-t)^2}\left(1-\mathrm{e}^{(i\Delta-\xi)t}\right) - A2_{CoLin}\,\mathrm{e}^{-\frac{1}{2}(\sigma\tau-\sigma_B t)^2}\,\mathrm{e}^{(-i\Delta_B-\xi_B)t}\right]. \tag{6.14}$$

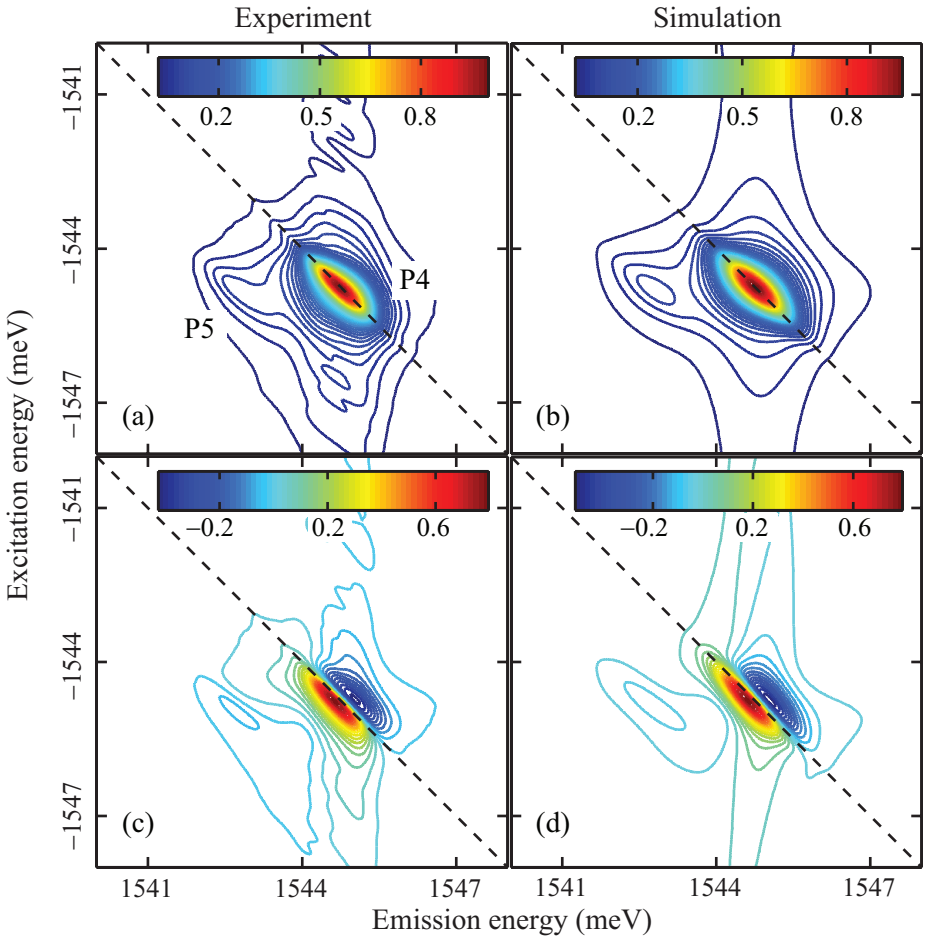

Figure 6.7: Measured (a) absolute value and (c) real part 2D spectra for the co-linear polarization scheme. The corresponding simulated spectra using best-fit parameter values are shown in (b), and (d), respectively. The peaks are labeled P4 and P5 in (a).

We perform the fitting procedure using slices from 2D spectrum simulated from Eq. (6.14). The only free parameters are the amplitude terms $A1_{CoLin}$ and $A2_{CoLin}$ since all the

other parameters were obtained from the co-circular and cross-linear spectra. Once again we obtain a very good match between theory and experiment, which is highlighted in the slices shown in Fig. 6.8. Only slices through peak P4 are shown because peak P5 is much weaker.

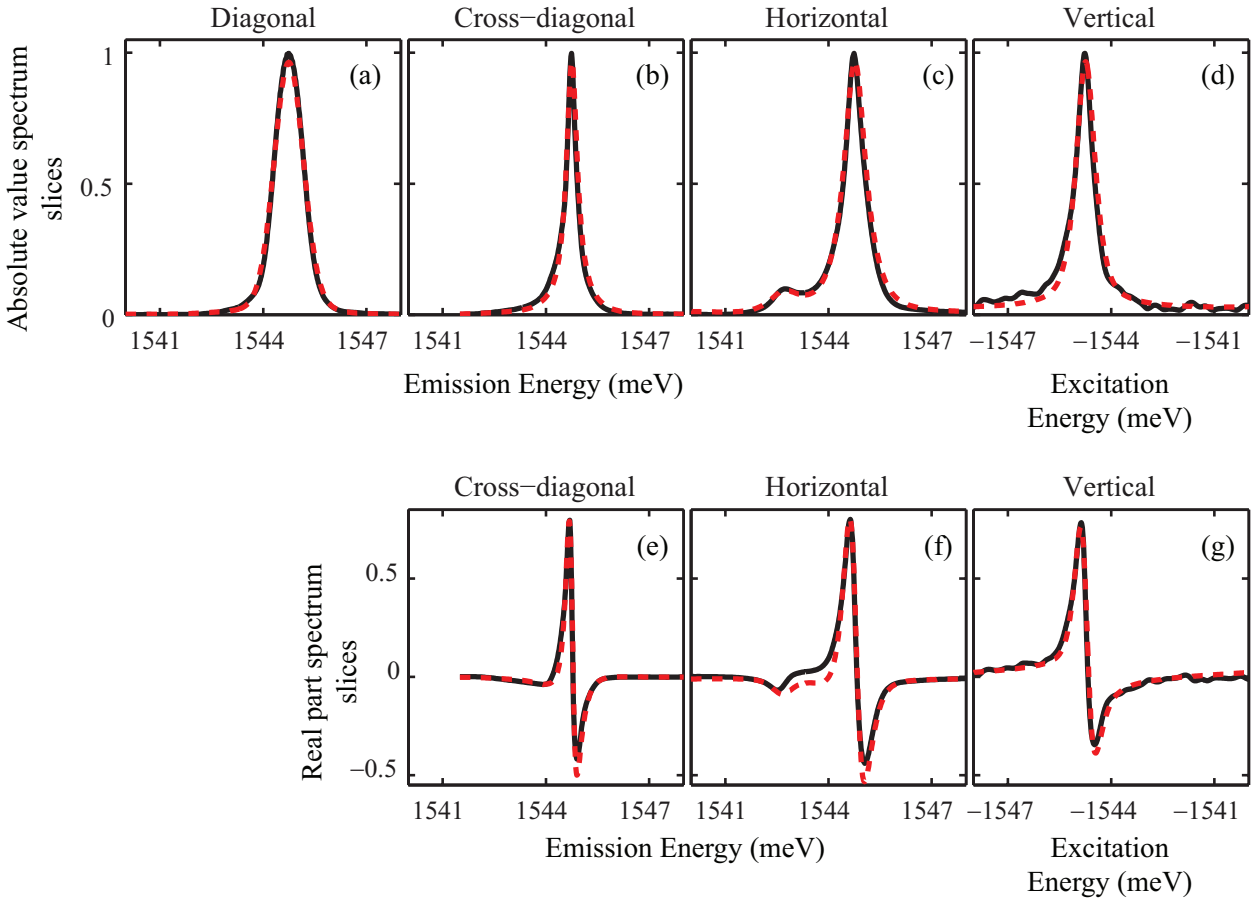

Figure 6.8: Experimental and simulation results for the slices used in the fitting procedure for the co-linear polarization scheme are shown in solid black and dashed red lines, respectively. The slices are taken through the maximum of the peak P4 shown in Fig. 6.7(a). The top and bottom rows shows the slices taken from the absolute value (Fig. 6.7(a)) and real part (Fig. 6.7(c)) spectra, respectively. The particular slice is indicated by the label above each plot.

The polarization dependent measurements that we have presented so far, highlight the effectiveness of the bosonic model. Despite its certain limitations, we can reproduce the experimentally obtained spectrum using a self consistent set of parameters, which were obtained though a fitting procedure. Next we will discuss the polarization-dependent dephasing

rate of excitons in these QWs measured from TFWM experiments [77, 78, 79].

6.2.5 Polarization dependent dephasing rate

The polarization dependent dephasing rate can be clearly seen in the cross-diagonal absolute value slices through peaks P1, P2 and P4 as shown in Fig. 6.9 as the markers. We find that while the peak-widths along the cross-diagonal direction for co-circular and co-linear polarization schemes are identical, they are significantly smaller than that for the cross-linear polarization scheme. This observation is similar to those previously reported [77, 78, 79]. Figure 6.9 also shows the cross-diagonal slices from the simulated spectra as lines. We can clearly reproduce the lineshapes measured for the different polarization schemes although the relevant linewidths are obtained only from 2D spectra measured for co-circular polarization scheme.

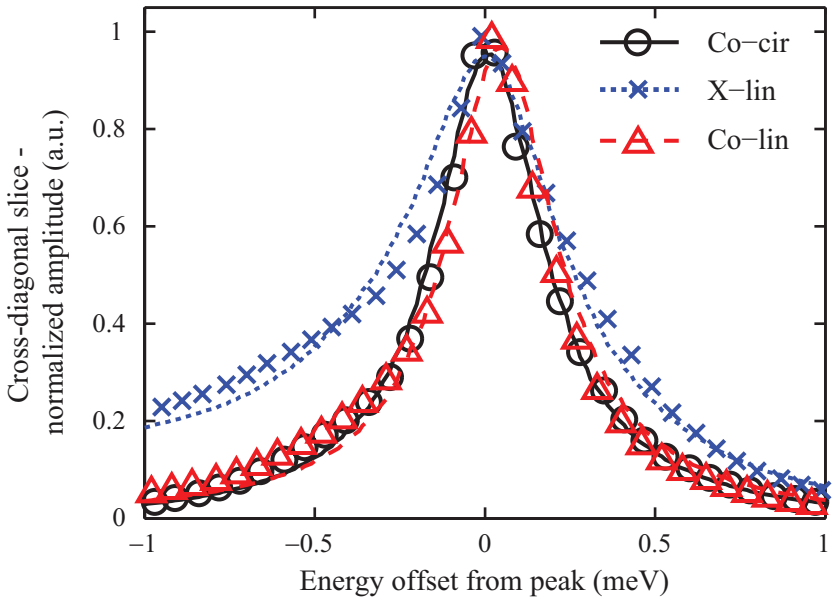

Figure 6.9: The cross-diagonal slices in measured and simulated spectra for the co-circular (Co-cir), cross-linear (X-lin) and co-linear (Co-lin) polarization schemes are shown by markers and lines, respectively. Note the broader cross-diagonal slice for cross-linear polarization compared to those for co-circular and co-linear polarizations. The asymmetric lineshape for cross-linear polarization is due to the wing of the biexciton peak.

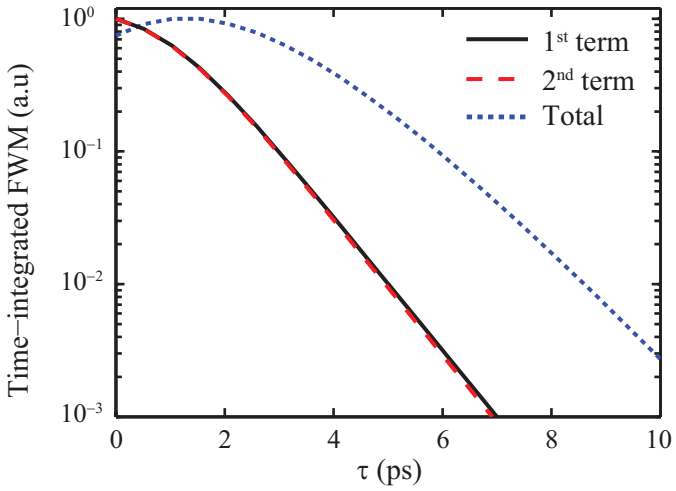

Figure 6.10: Simulated time-integrated transient four wave mixing signal for the first and second terms and the total signal in Eq. (6.10). The signals have been rescaled to have comparable values.

The difference in the lineshapes observed for different polarization schemes can be understood through the interference, or lack thereof, of signals from different quantum pathways that contribute to the peak appearing on the diagonal line. The spectral proximity of signal due to the different quantum pathways for co-circular polarization – including or excluding the $|1\pm\rangle\leftrightarrow|2\pm\rangle$ transitions – leads to nearly complete destructive interference at the wings of P1, along the horizontal direction, in Fig. 6.3(a). This interference results in a total nonlinear signal with significantly narrower width compared to the individual quantum pathway contributions. To highlight this point, we plot the time-integrated TFWM signal intensities for each quantum pathway (individual terms in Eq. (6.10)) as well as the total signal in Fig. 6.10 [1] . It is apparent that independently, the TFWM signal intensity from each quantum pathway is similar and decays at a fast rate (given by γ) compared to the total signal. The slower total signal decay rate results in a narrower peak in the frequency domain. However, for the cross-linear polarization scheme, quantum pathways involving only the $|G\rangle\leftrightarrow|1\pm\rangle$ transitions do not contribute to the signal at peak P2; the aforementioned interference goes

[1] We use the example of the time-integrated FWM signal to compare with the previous experimental results. However, the following discussion is valid for the decay of the signal during both delays – τ and t.

away, resulting in a much broader peak. Thus, the decay rate of total signal can be significantly different than decay rates of the individual transitions that constitute the signal. This effect is a manifestation of the bosonic character of excitons and has not been previous highlighted although scattering states of unbound two-exciton states have been considered [137, 138, 133, 105, 106] to obtain energy-level schemes similar to the one shown in Fig. 6.1(b). The scattering state was either considered to have the same polarization selection rule as the biexciton state and was ignored for co-circular excitation [137, 138, 133] or the relation $\mu_1 = \mu_2$ was assumed [105, 106], which does not give the dispersive peak observed in Fig. 6.3(c).

6.3 Excitation-density dependence

In Section 6.2 we illustrated the validity of the bosonic model of excitons through polarization dependent experiments. We were also able to quantify the exciton-exciton interaction terms. While introducing this model in Section 6.1.1, we distinguished between the inter- and intra-mode interactions. Now we will quantify these interactions through exciton-density-dependent measurements.

6.3.1 Inter-mode interactions

The exciton-exciton interactions between different modes results in an exciton-density dependent resonance energy of the $|0\rangle \leftrightarrow |1\pm\rangle$ transitions. The exciton-density dependence of these parameters is linear and given by Eqs. (6.4) and (6.5). Measurements of $\hbar\omega$ and γ as a function of the exciton density will be used to obtain the inter-mode interaction terms Δ' and ξ'.

The transition energy of the $|0\rangle \leftrightarrow |1\pm\rangle$ can be directly measured from the peak position in the absolute value spectrum for the co-circular polarization. The measured values as a function of the exciton density is shown in Fig. 6.11(a) as the markers. The statistical error bars are obtained by repeating the measurement for each power thrice. The figure also

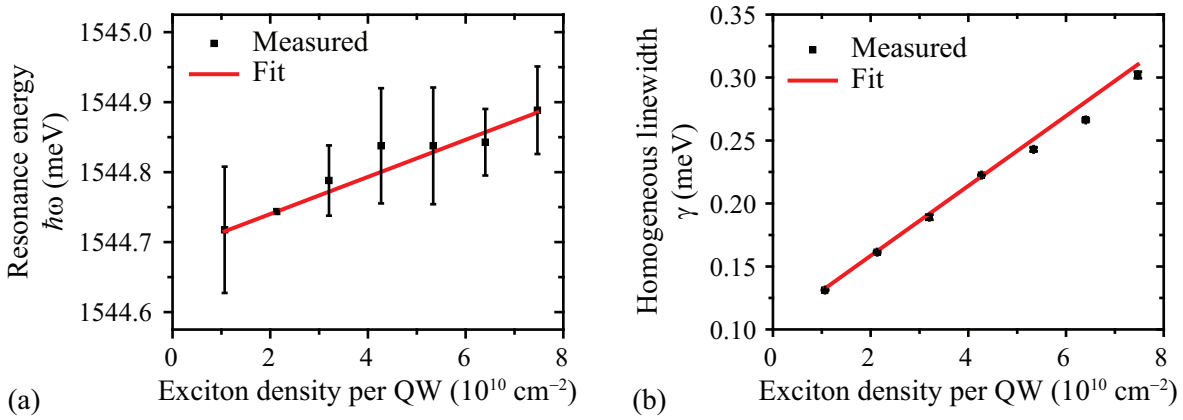

Figure 6.11: The excitation density dependence of (a) the resonance energy and (b) the dephasing rate of the $|G\rangle \leftrightarrow |1\pm\rangle$ transitions. The statistical error bars are obtained by repeating measurements thrice. The linear fit to the data is indicated by the solid red line.

shows the linear-fit to the data as the red line. We obtain $\hbar\omega_0 = 1544.687 \pm 0.005$ meV and $\Delta' \approx 0.53$ μeV/exciton for a spot diameter of ~ 50 microns.

We repeat the fitting procedure for different exciton densities to obtain the measured γ as shown in Fig. 6.11(b). Once again we observe that γ increases linearly with the exciton density, as expected from Eq. (6.5). The linear fit to the data is indicated by the red line in Fig. 6.11(b). We measure $\gamma_0 = 0.103 \pm 0.003$ meV and $\xi' \approx 0.55$ μeV/exciton. We find that Δ' and ξ' are approximately equal. Approximate values of Δ' and ξ' are quoted because the exciton density indicated in the plots in Fig. 6.11 are approximate.

6.3.2 Intra-mode interactions

It follows from the discussion in Section 6.1.1 that the intra-mode interaction terms should be independent of the exciton density. The measured values of the intra-mode interaction terms Δ and ξ are plotted in Figs. 6.12(a) and 6.12(b), respectively. As expected, the values of these parameters, within the error bars, do not change with the exciton density. We obtain $\Delta = 19 \pm 3$ μeV and $\xi = 6 \pm 1$ μeV by taking a weighted mean over the values measured over the entire exciton-density range studied. We would like to emphasize that although the values of Δ and ξ are independent of the excitation density, the resonance

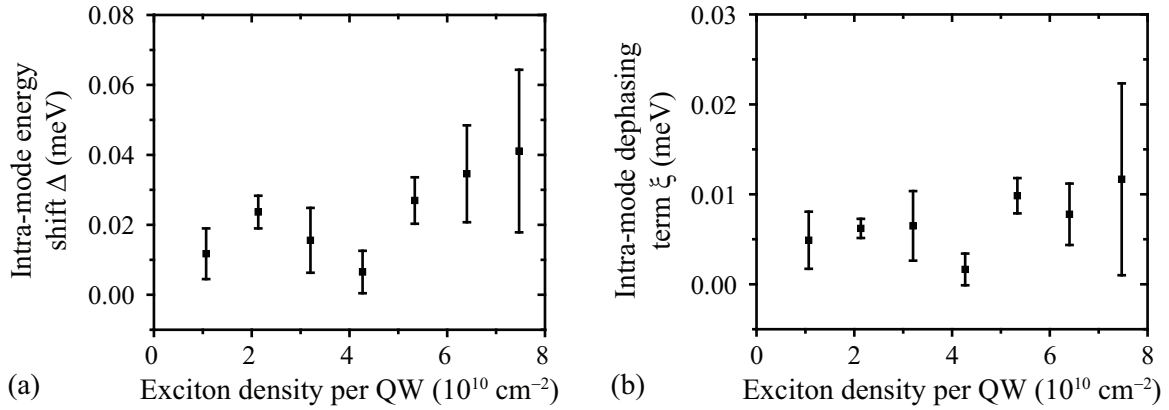

Figure 6.12: The intra-mode exciton-exciton (a) interaction energy and (b) dephasing term as a function of the exciton density. Both parameters are independent of the exciton density. The statistical error bars are obtained by repeating measurements thrice.

energy and dephasing rate during delay t is different than that during delay τ. As a result, these parameters indicate EIS and EID, respectively.

6.3.3 Biexcitonic interactions

We also performed the exciton-density-dependence experiment for the cross-linear polarization scheme. We repeated the fitting procedure mentioned in Section 6.2.3 for each exciton density. We plot the biexciton interaction energies Δ_B and ξ_B in Figs. 6.13(a) and 6.13(b), respectively.

We find that the biexciton binding energy increases with the exciton density. This trend is similar to the trend measured, for significantly higher exciton densities, by Almand-Hunter et al. [65]. Interestingly the rate of increase in the biexciton binding energy is approximately the same as the rate of increase in the transition energy of the $|0\rangle \leftrightarrow |1\pm\rangle$ transitions indicated in Fig. 6.11(a). The upshot is that the energy of the $|\mathrm{Bx}\rangle$ state is independent of the exciton density in the range of exciton densities probed.

The difference between the dephasing rates of the $|1\pm\rangle \leftrightarrow |\mathrm{Bx}\rangle$ and $|0\rangle \leftrightarrow |1\pm\rangle$ transitions decreases, and changes sign, with an increase in the exciton density, as shown in Fig. 6.13(b). This behavior is not expected from the model that we have presented. Coinci-

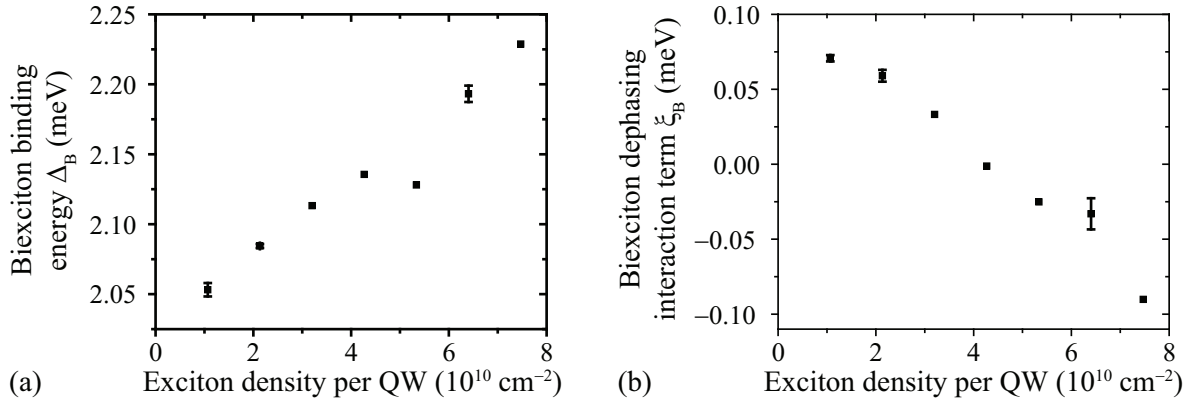

Figure 6.13: The biexciton (a) binding energy and (b) dephasing term as a function of the exciton density. Both the values are nominally independent of the exciton density. The statistical error bars are obtained by repeating measurements thrice.

dentally, this decrease in dephasing rate almost cancels the increase in the dephasing rate of the $|0\rangle \leftrightarrow |1\pm\rangle$ transition shown in Fig. 6.11(b), which results in the dephasing rate of the $|1\pm\rangle \leftrightarrow |\mathrm{Bx}\rangle$ transition that is independent of the exciton density. In addition to the interaction between opposite-spin excitons, other higher-order correlations also contribute to the formation of biexctions [139]. This simplification could be a possible reason for the unexpected exciton density dependence of the interactions between opposite-spin excitons.

In this chapter, we have used 2DCS experiments to highlight the bosonic nature of QW excitons and their effect on the radiated non-linear signal. The previous measurements of polarization dependent exciton dephasing rate is a natural consequence of this bosonic nature. Exciton-exciton interactions are included in a physically intuitive and straightforward way using the model of interacting bosons. Also, we have shown that the observed decay rate of measured non-linear signal can be different from the dephasing rate of individual transitions that contribute to the signal for a boson-like system. In addition to providing important insight into exciton physics in QWs, these results also highlight the effects of a bosonic transition in non-linear optics experiments. Finally, we were able to separate and quantify inter- and intra-mode interactions between excitons through exciton-density-dependent experiments.

Chapter 7

Conclusion

We have explored various aspects of exciton physics in semiconductor QWs through 2DCS. The effect of structural symmetry on QW excitons was studied in (110)-oriented GaAs QWs. Properties of excitons such as spectral diffusion and exciton-exciton interactions, which have been previously studied extensively, were presented in a new light.

The polarization dependent dephasing rate of excitons in (110)-oriented QWs was found to be due to the anisotropic absorption coefficient in these structures. We found that the exciton dephasing is dominated by non-radiative processes. The thermal broadening revealed an activation-like behavior.

We demonstrated that the strong-redistribution approximation is not valid for the low sample temperatures although it is generally used to analyze spectral diffusion. Other methods such as 3PEPS are not sensitive enough to reveal this behavior. We have attributed this behavior to the lack of exciton population at low temperatures.

An important aspect of this work is the development of a numerical fitting procedure to analyze the measured 2D spectra quantitatively. The normalized frequency-frequency correlation function was quantified, for high sample temperatures, using this procedure. Although this correlation function is generally assumed to follow an exponential decay, our results show that this assumption is not valid.

A simple and physically-intuitive model of treating excitons as interacting bosons is introduced. We separated the exciton-exciton interactions into inter- and intra-mode com-

ponents. The numerical fitting procedure was used to quantify these interactions. The significantly simpler modeling of exciton-exciton interactions, compared to the previously used models, was critical for quantifying these interactions. We were able to explain the polarization-dependent exciton dephasing rates in these samples using the bosonic model.

7.1 Outlook

In this work we have revealed several novel properties of excitons in semiconductor QWs using 2DCS. A detailed investigation into some of these effects is currently being pursued. Some of the specific ongoing efforts are:

- We have proved that the strong-redistribution approximation is not valid in the case of excitons. We are collaborating with Marten Richter (Technische Universität Berlin) to develop a theoretical model of spectral diffusion. A series of exciton states are considered based on the spatial fluctuations in the QW width. Initial results reproduce the experimental observations qualitatively. Further work is being done to obtain a quantitative agreement between the experiment and theory.

- In Section 6.2.3, we noted that our modeling of the biexciton state is probably too simplistic. Specifically, the horizontal slices in Figs. 6.6(c) and 6.6(g) indicate an additional, albeit weak, peak. This peak suggests the existence of a bound vibrational state of the biexciton. Further modeling is required to confirm this hypothesis.

- We have also developed a numerical simulation method to solve the modified OBEs, which is presented in Appendix B. Our aim is to compare the effects due to EIS and local-field corrections. We are working on the correctly incorporate the local-field corrections in order to compare these effects.

- Preliminary results indicating the contribution of nominally disallowed exciton transition in (110)-oriented GaAs QWs to the 2D spectrum are presented in Appendix

D. Further experiments are needed to study the properties of this state along with its coupling with the other states. This exciton state might play a crucial for the observed spectral dependence of photocurrent direction in these samples [45].

- Preliminary experiments have also revealed the non-monotonic exciton-population evolution for sample temperatures > 40 K. This result is pretty interesting, and probably results from thermal activation of bright excitons to some high-energy dark exciton states. More experimental and theoretical studies are needed to probe this behavior.

Furthermore, the numerical fitting technique developed in this work can be applied to other systems. This procedure would be especially useful to quantify spectral diffusion using 2DCS since several observables are used to approximate the frequency-frequency correlation function [39]. Also, the bosonic model of excitons, and the modeling procedure can be extended to other systems such as exciton-polaritons [140] and plasmons [141]. The simplified simulation and fitting procedure is, in principle, very general and can be applied to any system where the system response can be modeled through OBEs.

Bibliography

[1] Steven T. Cundiff, "Coherent spectroscopy of semiconductors," Opt. Express, vol. 16, pp. 4639–4664, Mar 2008.

[2] M. D. Webb, S. T. Cundiff, and D. G. Steel, "Observation of time-resolved picosecond stimulated photon echoes and free polarization decay in GaAs/AlGaAs multiple quantum wells," Phys. Rev. Lett., vol. 66, pp. 934–937, Feb 1991.

[3] M. Koch, J. Feldmann, G. von Plessen, E. O. Göbel, P. Thomas, and K. Köhler, "Quantum beats versus polarization interference: An experimental distinction," Phys. Rev. Lett., vol. 69, pp. 3631–3634, Dec 1992.

[4] H. Wang, K. Ferrio, D. G. Steel, Y. Z. Hu, R. Binder, and S. W. Koch, "Transient nonlinear optical response from excitation induced dephasing in GaAs," Phys. Rev. Lett., vol. 71, pp. 1261–1264, Aug 1993.

[5] J. M. Shacklette and S. T. Cundiff, "Role of excitation-induced shift in the coherent optical response of semiconductors," Phys. Rev. B, vol. 66, p. 045309, Jul 2002.

[6] M. Wegener, D. S. Chemla, S. Schmitt Rink, and W. Schäfer, "Line shape of time-resolved four-wave mixing," Phys. Rev. A, vol. 42, pp. 5675–5683, Nov 1990.

[7] R. R. Ernst, G. Bodenhausen, and A. Wokaun, Principles of nuclear magnetic resonance in one and two dimensions. Oxford University Press, New York, 1987.

[8] John D. Hybl, Allison W. Albrecht, Sarah M. Gallagher Faeder, and David M. Jonas, "Two-dimensional electronic spectroscopy," Chem. Phys. Lett., vol. 297, no. 34, pp. 307 – 313, 1998.

[9] M. C. Asplund, M. T. Zanni, and R. M. Hochstrasser, "Two-dimensional infrared spectroscopy of peptides by phase-controlled femtosecond vibrational photon echoes," Proc. Natl. Acad. Sci. USA, vol. 97, no. 15, pp. 8219–8224, 2000.

[10] S. Cundiff, A. Bristow, M. Siemens, Hebin Li, G. Moody, D. Karaiskaj, Xingcan Dai, and Tianhao Zhang, "Optical 2-D Fourier Transform Spectroscopy of Excitons in Semiconductor Nanostructures," IEEE J. Sel. Topics Quantum Electron., vol. 18, pp. 318–328, Jan 2012.

[11] G. Moody, M. E. Siemens, A. D. Bristow, X. Dai, D. Karaiskaj, A. S. Bracker, D. Gammon, and S. T. Cundiff, "Exciton-exciton and exciton-phonon interactions in an interfacial GaAs quantum dot ensemble," Phys. Rev. B, vol. 83, p. 115324, Mar 2011.

[12] Camelia N. Borca, Tianhao Zhang, Xiaoqin Li, and Steven T. Cundiff, "Optical two-dimensional Fourier transform spectroscopy of semiconductors," Chem. Phys. Lett., vol. 416, no. 46, pp. 311 – 315, 2005.

[13] X. Li, T. Zhang, C. N. Borca, and S. T. Cundiff, "Many-Body Interactions in Semiconductors Probed by Optical Two-Dimensional Fourier Transform Spectroscopy," Phys. Rev. Lett., vol. 96, p. 057406, Feb 2006.

[14] I. Kuznetsova, P. Thomas, T. Meier, T. Zhang, X. Li, R. Mirin, and S. Cundiff, "Signatures of many-particle correlations in two-dimensional Fourier-transform spectra of semiconductor nanostructures," Solid State Commun., vol. 142, no. 3, pp. 154 – 158, 2007.

[15] H. Haug and S. W. Koch, Quantum Theory of the Optical and Electronic Properties of Semiconductors. World Scientific, Singapore, 2009.

[16] D. S. Chemla and J. Shah, "Many-body and correlation effects in semiconductors," Nature, vol. 411, pp. 549–557, May 2001.

[17] S. T. Cundiff, "Optical two-dimensional Fourier transform spectroscopy of semiconductor nanostructures [Invited]," J. Opt. Soc. Am. B, vol. 29, pp. A69–A81, Feb 2012.

[18] O. Madelung, ed., Semiconductors – Basic Data. Springer-Verlag, Berlin, 1996.

[19] C. L. Tang, Fundamentals of Quantum Mechanics: For Solid State Electronics and Optics. Cambridge University Press, Cambridge, 2009.

[20] R. P. Smith, Quantitative measurements of many-body exciton dynamics in GaAs quantum-well structures. PhD thesis, University of Colorado Boulder, 2010.

[21] T. Zhang, Optical Two-Dimensional Fourier Transform Spectroscopy of Semiconductors. PhD thesis, University of Colorado Boulder, 2008.

[22] N. Peyghambarian, S. W. Koch, and A. Mysyrowicz, Introduction to Semiconductor Optics. Prentice Hall, New Jersey, 1993.

[23] R. C. Miller, D. A. Kleinman, W. T. Tsang, and A. C. Gossard, "Observation of the excited level of excitons in GaAs quantum wells," Phys. Rev. B, vol. 24, pp. 1134–1136, Jul 1981.

[24] R. L. Greene and K. Bajaj, "Binding energies of wannier excitons in GaAs-Ga1xAlxAs quantum well structures," Solid State Commun., vol. 45, no. 9, pp. 831 – 835, 1983.

[25] J. F. Ryan, R. A. Taylor, A. J. Turberfield, A. Maciel, J. M. Worlock, A. C. Gossard, and W. Wiegmann, "Time-Resolved Photoluminescence of Two-Dimensional Hot Carriers in GaAs-AlGaAs Heterostructures," Phys. Rev. Lett., vol. 53, pp. 1841–1844, Nov 1984.

[26] B. Deveaud, F. Clérot, N. Roy, K. Satzke, B. Sermage, and D. S. Katzer, "Enhanced radiative recombination of free excitons in GaAs quantum wells," Phys. Rev. Lett., vol. 67, pp. 2355–2358, Oct 1991.

[27] C. Weisbuch, R. Dingle, A. Gossard, and W. Wiegmann, "Optical characterization of interface disorder in GaAs-$Ga_{1-x}Al_xAs$ multi-quantum well structures," Solid State Commun., vol. 38, no. 8, pp. 709 – 712, 1981.

[28] A. Catellani and P. Ballone, "Islands at semiconductor interfaces," Phys. Rev. B, vol. 45, pp. 14197–14203, Jun 1992.

[29] A. Zrenner, L. V. Butov, M. Hagn, G. Abstreiter, G. Böhm, and G. Weimann, "Quantum dots formed by interface fluctuations in AlAs/GaAs coupled quantum well structures," Phys. Rev. Lett., vol. 72, pp. 3382–3385, May 1994.

[30] D. S. Citrin, "Radiative lifetimes of excitons in quantum wells: Localization and phase-coherence effects," Phys. Rev. B, vol. 47, pp. 3832–3841, Feb 1993.

[31] A. D. Bristow, T. Zhang, M. E. Siemens, S. T. Cundiff, and R. P. Mirin, "Separating Homogeneous and Inhomogeneous Line Widths of Heavy- and Light-Hole Excitons in Weakly Disordered Semiconductor Quantum Wells," J. Phys. Chem. B, vol. 115, no. 18, pp. 5365–5371, 2011.

[32] J. Hegarty, L. Goldner, and M. D. Sturge, "Localized and delocalized two-dimensional excitons in GaAs-AlGaAs multiple-quantum-well structures," Phys. Rev. B, vol. 30, pp. 7346–7348, Dec 1984.

[33] U. Jahn, M. Ramsteiner, R. Hey, H. T. Grahn, E. Runge, and R. Zimmermann, "Effective exciton mobility edge in narrow quantum wells," Phys. Rev. B, vol. 56, pp. R4387–R4390, Aug 1997.

[34] J. Hegarty and M. D. Sturge, "Studies of exciton localization in quantum-well structures by nonlinear-optical techniques," J. Opt. Soc. Am. B, vol. 2, pp. 1143–1154, Jul 1985.

[35] V. O. Lorenz and S. T. Cundiff, "Non-Markovian Dynamics in a Dense Potassium Vapor," Phys. Rev. Lett., vol. 95, p. 163601, Oct 2005.

[36] M. Cho, J.-Y. Yu, T. Joo, Y. Nagasawa, S. A. Passino, and G. R. Fleming, "The Integrated Photon Echo and Solvation Dynamics," J. Phys. Chem., vol. 100, no. 29, pp. 11944–11953, 1996.

[37] W. P. de Boeij, M. S. Pshenichnikov, and D. A. Wiersma, "Ultrafast Solvation Dynamics Eexplored by Femtosecond Photon Echo Spectroscopies," Annu. Rev. Phys. Chem, vol. 49, no. 1, pp. 99–123, 1998.

[38] S. Mukamel, Principles of Nonlinear Optical Spectroscopy. Oxford University Press, New York, 1995.

[39] S. T. Roberts, J. J. Loparo, and A. Tokmakoff, "Characterization of spectral diffusion from two-dimensional line shapes," J. Chem. Phys., vol. 125, no. 8, p. 084502, 2006.

[40] S. G. Carter, Z. Chen, and S. T. Cundiff, "Echo peak-shift spectroscopy of non-Markovian exciton dynamics in quantum wells," Phys. Rev. B, vol. 76, p. 121303, Sep 2007.

[41] Y. Ogawa, H. Tahara, and F. Minami, "Non-Markovian nature of exciton-exciton scattering in a GaAs single quantum well observed by phase-locked laser pulses," Phys. Rev. B, vol. 87, p. 165305, Apr 2013.

[42] H. Diehl, V. A. Shalygin, V. V. Bel'kov, Ch. Hoffmann, S. N. Danilov, T. Herrle, S. A. Tarasenko, D. Schuh, Ch. Gerl, W. Wegscheider, W. Prettl, and S. D. Ganichev, "Spin photocurrents in (110)-grown quantum well structures," New J. Phys., vol. 9, no. 9, p. 349, 2007.

[43] M. Bieler, "THz Generation From Resonant Excitation of Semiconductor Nanostructures: Investigation of Second-Order Nonlinear Optical Effects," IEEE J. Sel. Topics Quantum Electron., vol. 14, pp. 458 –469, march-april 2008.

[44] S. D. Ganichev and W. Prettl, "Spin photocurrents in quantum wells," J. Phys. Condens. Matter, vol. 15, no. 20, p. R935, 2003.

[45] H. T. Duc, J. Förstner, and T. Meier, "Microscopic analysis of charge and spin photocurrents injected by circularly polarized one-color laser pulses in GaAs quantum wells," Phys. Rev. B, vol. 82, p. 115316, Sep 2010.

[46] R. Singh, T. M. Autry, G. Nardin, G. Moody, H. Li, K. Pierz, M. Bieler, and S. T. Cundiff, "Anisotropic homogeneous linewidth of the heavy-hole exciton in (110)-oriented GaAs quantum wells," Phys. Rev. B, vol. 88, p. 045304, Jul 2013.

[47] Y. Ohno, R. Terauchi, T. Adachi, F. Matsukura, and H. Ohno, "Spin Relaxation in GaAs(110) Quantum Wells," Phys. Rev. Lett., vol. 83, pp. 4196–4199, Nov 1999.

[48] G. M. Müller, M. Römer, D. Schuh, W. Wegscheider, J. Hübner, and M. Oestreich, "Spin Noise Spectroscopy in GaAs (110) Quantum Wells: Access to Intrinsic Spin Lifetimes and Equilibrium Electron Dynamics," Phys. Rev. Lett., vol. 101, p. 206601, Nov 2008.

[49] A. Haché, Y. Kostoulas, R. Atanasov, J. L. P. Hughes, J. E. Sipe, and H. M. van Driel, "Observation of Coherently Controlled Photocurrent in Unbiased, Bulk GaAs," Phys. Rev. Lett., vol. 78, pp. 306–309, Jan 1997.

[50] M. J. Stevens, A. L. Smirl, R. D. R. Bhat, A. Najmaie, J. E. Sipe, and H. M. van Driel, "Quantum Interference Control of Ballistic Pure Spin Currents in Semiconductors," Phys. Rev. Lett., vol. 90, p. 136603, Apr 2003.

[51] S. Priyadarshi, K. Pierz, and M. Bieler, "All-Optically Induced Ultrafast Photocurrents: Beyond the Instantaneous Coherent Response," Phys. Rev. Lett., vol. 109, p. 216601, Nov 2012.

[52] M. Bieler, K. Pierz, U. Siegner, and P. Dawson, "Quantum interference currents by excitation of heavy- and light-hole excitons in GaAs/$Al_{0.3}Ga_{0.7}As$ quantum wells," Phys. Rev. B, vol. 73, p. 241312, Jun 2006.

[53] S. Oertel, S. Kunz, D. Schuh, W. Wegscheider, J. Hübner, and M. Oestreich, "Electron spin relaxation as tracer of excitons in a two-dimensional electron-hole plasma inside a (110)-GaAs quantum well," Europhys. Lett., vol. 96, no. 6, p. 67010, 2011.

[54] M. Lindberg and S. W. Koch, "Effective Bloch equations for semiconductors," Phys. Rev. B, vol. 38, pp. 3342–3350, Aug 1988.

[55] A. Honold, L. Schultheis, J. Kuhl, and C. W. Tu, "Collision broadening of two-dimensional excitons in a GaAs single quantum well," Phys. Rev. B, vol. 40, pp. 6442–6445, Sep 1989.

[56] B. H. Bransden and C. J. Joachain, Physics of Atoms and Molecules. Pearson Education, Delhi, 1996.

[57] G. W. Fehrenbach, W. Schäfer, J. Treusch, and R. G. Ulbrich, "Transient Optical Spectra of a Dense Exciton Gas in a Direct-Gap Semiconductor," Phys. Rev. Lett., vol. 49, pp. 1281–1284, Oct 1982.

[58] N. Peyghambarian, H. M. Gibbs, J. L. Jewell, A. Antonetti, A. Migus, D. Hulin, and A. Mysyrowicz, "Blue Shift of the Exciton Resonance due to Exciton-Exciton Interactions in a Multiple-Quantum-Well Structure," Phys. Rev. Lett., vol. 53, pp. 2433–2436, Dec 1984.

[59] D. Chemla, W. Knox, D. Miller, S. Schmitt Rink, J. Stark, and R. Zimmermann, "The excitonic optical stark effect in semiconductor quantum wells probed with femtosecond optical pulses," J. Lumin., vol. 44, no. 46, pp. 233 – 246, 1989.

[60] K. Leo, M. Wegener, J. Shah, D. S. Chemla, E. O. Göbel, T. C. Damen, S. Schmitt Rink, and W. Schäfer, "Effects of coherent polarization interactions on time-resolved degenerate four-wave mixing," Phys. Rev. Lett., vol. 65, pp. 1340–1343, Sep 1990.

[61] R. C. Miller, D. A. Kleinman, A. C. Gossard, and O. Munteanu, "Biexcitons in GaAs quantum wells," Phys. Rev. B, vol. 25, pp. 6545–6547, May 1982.

[62] K. W. Stone, K. Gundogdu, D. B. Turner, X. Li, S. T. Cundiff, and K. A. Nelson, "Two-Quantum 2D FT Electronic Spectroscopy of Biexcitons in GaAs Quantum Wells," Science, vol. 324, no. 5931, pp. 1169–1173, 2009.

[63] D. Karaiskaj, A. D. Bristow, L. Yang, X. Dai, R. P. Mirin, S. Mukamel, and S. T. Cundiff, "Two-Quantum Many-Body Coherences in Two-Dimensional Fourier-Transform Spectra of Exciton Resonances in Semiconductor Quantum Wells," Phys. Rev. Lett., vol. 104, p. 117401, Mar 2010.

[64] D. B. Turner and K. A. Nelson, "Coherent measurements of high-order electronic correlations in quantum wells," Nature, vol. 466, pp. 1089–1092, Aug. 2010.

[65] A. E. Almand Hunter, H. Li, S. T. Cundiff, M. Mootz, M. Kira, and S. W. Koch, "Quantum droplets of electrons and holes," Nature, vol. 506, pp. 471–475, Feb. 2014.

[66] G. Finkelstein, S. Bar Ad, O. Carmel, I. Bar Joseph, and Y. Levinson, "Biexcitonic effects in transient nonlinear optical experiments in quantum wells," Phys. Rev. B, vol. 47, pp. 12964–12967, May 1993.

[67] K. Bott, O. Heller, D. Bennhardt, S. T. Cundiff, P. Thomas, E. J. Mayer, G. O. Smith, R. Eccleston, J. Kuhl, and K. Ploog, "Influence of exciton-exciton interactions on the coherent optical response in GaAs quantum wells," Phys. Rev. B, vol. 48, pp. 17418–17426, Dec 1993.

[68] J. J. Hopfield, "Theory of the Contribution of Excitons to the Complex Dielectric Constant of Crystals," Phys. Rev., vol. 112, pp. 1555–1567, Dec 1958.

[69] E. Hanamura and H. Haug, "Condensation effects of excitons," Phys. Rep., vol. 33, no. 4, pp. 209 – 284, 1977.

[70] G. Rochat, C. Ciuti, V. Savona, C. Piermarocchi, A. Quattropani, and P. Schwendimann, "Excitonic Bloch equations for a two-dimensional system of interacting excitons," Phys. Rev. B, vol. 61, pp. 13856–13862, May 2000.

[71] M. Kuwata Gonokami, S. Inouye, H. Suzuura, M. Shirane, R. Shimano, T. Someya, and H. Sakaki, "Parametric Scattering of Cavity Polaritons," Phys. Rev. Lett., vol. 79, pp. 1341–1344, Aug 1997.

[72] J. P. Eisenstein and A. H. MacDonald, "Bose-Einstein condensation of excitons in bilayer electron systems," Nature, vol. 432, pp. 691–694, Dec. 2004.

[73] T. Häupl, H. Nickolaus, F. Henneberger, and A. Schülzgen, "Femtosecond degenerate four-wave mixing study of exciton coherence in wide-gap II–VI quantum wells," Phys. Status Solidi B, vol. 194, no. 1, pp. 219–230, 1996.

[74] M. Shirane, C. Ramkumar, Y. P. Svirko, H. Suzuura, S. Inouye, R. Shimano, T. Someya, H. Sakaki, and M. Kuwata Gonokami, "Degenerate four-wave mixing measurements on an exciton-photon coupled system in a semiconductor microcavity," Phys. Rev. B, vol. 58, pp. 7978–7985, Sep 1998.

[75] G. Khitrova, H. M. Gibbs, F. Jahnke, M. Kira, and S. W. Koch, "Nonlinear optics of normal-mode-coupling semiconductor microcavities," Rev. Mod. Phys., vol. 71, pp. 1591–1639, Oct 1999.

[76] S. Savasta and R. Girlanda, "Cavity polaritons beyond the boson approximation," Il Nuovo Cimento D, vol. 17, no. 11-12, pp. 1705–1712, 1995.

[77] S. T. Cundiff, H. Wang, and D. G. Steel, "Polarization-dependent picosecond excitonic nonlinearities and the complexities of disorder," Phys. Rev. B, vol. 46, pp. 7248–7251, Sep 1992.

[78] S. Schmitt Rink, D. Bennhardt, V. Heuckeroth, P. Thomas, P. Haring, G. Maidorn, H. Bakker, K. Leo, D.-S. Kim, J. Shah, and K. Köhler, "Polarization dependence of heavy- and light-hole quantum beats," Phys. Rev. B, vol. 46, pp. 10460–10463, Oct 1992.

[79] H. H. Yaffe, J. P. Harbison, L. T. Florez, and Y. Prior, "Polarization dependence and selection rules of transient four-wave mixing in GaAs quantum-well excitons," J. Opt. Soc. Am. B, vol. 10, pp. 578–583, Apr 1993.

[80] D. Gershoni, I. Brener, G. A. Baraff, S. N. G. Chu, L. N. Pfeiffer, and K. West, "Anisotropic optical properties of (110)-oriented quantum wells," Phys. Rev. B, vol. 44, pp. 1930–1933, Jul 1991.

[81] E. D. Potter, J. L. Herek, S. Pedersen, Q. Liu, and A. H. Zewail, "Femtosecond laser control of a chemical reaction," Nature, vol. 355, pp. 66–68, Jan. 1992.

[82] A. Assion, T. Baumert, M. Bergt, T. Brixner, B. Kiefer, V. Seyfried, M. Strehle, and G. Gerber, "Control of Chemical Reactions by Feedback-Optimized Phase-Shaped Femtosecond Laser Pulses," Science, vol. 282, no. 5390, pp. 919–922, 1998.

[83] E. Dupont, P. B. Corkum, H. C. Liu, M. Buchanan, and Z. R. Wasilewski, "Phase-Controlled Currents in Semiconductors," Phys. Rev. Lett., vol. 74, pp. 3596–3599, May 1995.

[84] A. P. Heberle, J. J. Baumberg, and K. Köhler, "Ultrafast Coherent Control and Destruction of Excitons in Quantum Wells," Phys. Rev. Lett., vol. 75, pp. 2598–2601, Sep 1995.

[85] Michael Woerner, Wilhelm Kuehn, Pamela Bowlan, Klaus Reimann, and Thomas Elsaesser, "Ultrafast two-dimensional terahertz spectroscopy of elementary excitations in solids," New J. Phys., vol. 15, no. 2, p. 025039, 2013.

[86] O. Golonzka, M. Khalil, N. Demirdöven, and A. Tokmakoff, "Vibrational Anharmonicities Revealed by Coherent Two-Dimensional Infrared Spectroscopy," Phys. Rev. Lett., vol. 86, pp. 2154–2157, Mar 2001.

[87] C.-h. Tseng, S. Matsika, and T. C. Weinacht, "Two-Dimensional Ultrafast Fourier Transform Spectroscopy in the Deep Ultraviolet," Opt. Express, vol. 17, pp. 18788–18793, Oct 2009.

[88] D. Brida, C. Manzoni, and G. Cerullo, "Phase-locked pulses for two-dimensional spectroscopy by a birefringent delay line," Opt. Lett., vol. 37, pp. 3027–3029, Aug 2012.

[89] D. B. Turner, K. W. Stone, K. Gundogdu, and K. A. Nelson, "Three-dimensional electronic spectroscopy of excitons in GaAs quantum wells," J. Chem. Phys., vol. 131, no. 14, p. 144510, 2009.

[90] H. Li, A. D. Bristow, M. E. Siemens, G. Moody, and S. T. Cundiff, "Unraveling quantum pathways using optical 3D Fourier-transform spectroscopy," Nat Commun, vol. 4, pp. 1390–, Jan. 2013.

[91] P. Tian, D. Keusters, Y. Suzaki, and W. S. Warren, "Femtosecond Phase-Coherent Two-Dimensional Spectroscopy," Science, vol. 300, no. 5625, pp. 1553–1555, 2003.

[92] J. C. Vaughan, T. Hornung, K. W. Stone, and K. A. Nelson, "Coherently Controlled Ultrafast Four-Wave Mixing Spectroscopy," J. Phys. Chem. A, vol. 111, no. 23, pp. 4873–4883, 2007.

[93] P. F. Tekavec, G. A. Lott, and A. H. Marcus, "Fluorescence-detected two-dimensional electronic coherence spectroscopy by acousto-optic phase modulation," J. Chem. Phys., vol. 127, no. 21, p. 214307, 2007.

[94] X. Dai, M. Richter, H. Li, A. D. Bristow, C. Falvo, S. Mukamel, and S. T. Cundiff, "Two-Dimensional Double-Quantum Spectra Reveal Collective Resonances in an Atomic Vapor," Phys. Rev. Lett., vol. 108, p. 193201, May 2012.

[95] C. Y. Wong and G. D. Scholes, "Biexcitonic Fine Structure of CdSe Nanocrystals Probed by Polarization-Dependent Two-Dimensional Photon Echo Spectroscopy," J. Phys. Chem. A, vol. 115, no. 16, pp. 3797–3806, 2011.

[96] T. Brixner, J. Stenger, H. M. Vaswani, M. Cho, R. E. Blankenship, and G. R. Fleming, "Two-dimensional spectroscopy of electronic couplings in photosynthesis," Nature, vol. 434, pp. 625–628, Mar. 2005.

[97] J. Kasprzak, B. Patton, V. Savona, and W. Langbein, "Coherent coupling between distant excitons revealed by two-dimensional nonlinear hyperspectral imaging," Nat Photon, vol. 5, pp. 57–63, Jan. 2011.

[98] V. M. Huxter, T. A. A. Oliver, D. Budker, and G. R. Fleming, "Vibrational and electronic dynamics of nitrogen-vacancy centres in diamond revealed by two-dimensional ultrafast spectroscopy," Nat Phys, vol. 9, pp. 744–749, Nov. 2013.

[99] T. Zhang, I. Kuznetsova, T. Meier, X. Li, R. P. Mirin, P. Thomas, and S. T. Cundiff, "Polarization-dependent optical 2D Fourier transform spectroscopy of semiconductors," Proc. Natl. Acad. Sci. USA, vol. 104, no. 36, pp. 14227–14232, 2007.

[100] G. Moody, Confinement Effects on the Electronic and Optical Properties of Semiconductor Quantum Dots Revealed with Two-Dimensional Coherent Spectroscopy. PhD thesis, University of Colorado Boulder, 2013.

[101] V. G. Lyssenko, J. Erland, I. Balslev, K.-H. Pantke, B. S. Razbirin, and J. M. Hvam, "Nature of nonlinear four-wave-mixing beats in semiconductors," Phys. Rev. B, vol. 48, pp. 5720–5723, Aug 1993.

[102] V. O. Lorenz, S. Mukamel, W. Zhuang, and S. T. Cundiff, "Ultrafast Optical Spectroscopy of Spectral Fluctuations in a Dense Atomic Vapor," Phys. Rev. Lett., vol. 100, p. 013603, Jan 2008.

[103] M. Khalil, N. Demirdöven, and A. Tokmakoff, "Obtaining Absorptive Line Shapes in Two-Dimensional Infrared Vibrational Correlation Spectra," Phys. Rev. Lett., vol. 90, p. 047401, Jan 2003.

[104] M. E. Siemens, G. Moody, H. Li, A. D. Bristow, and S. T. Cundiff, "Resonance lineshapes in two-dimensional Fourier transform spectroscopy," Opt. Express, vol. 18, pp. 17699–17708, Aug 2010.

[105] G. Nardin, G. Moody, R. Singh, T. M. Autry, H. Li, F. Morier Genoud, and S. T. Cundiff, "Coherent Excitonic Coupling in an Asymmetric Double InGaAs Quantum Well Arises from Many-Body Effects," Phys. Rev. Lett., vol. 112, p. 046402, Jan 2014.

[106] G. Moody, I. A. Akimov, H. Li, R. Singh, D. R. Yakovlev, G. Karczewski, M. Wiater, T. Wojtowicz, M. Bayer, and S. T. Cundiff, "Coherent Coupling of Excitons and Trions in a Photoexcited CdTe/CdMgTe Quantum Well," Phys. Rev. Lett., vol. 112, p. 097401, Mar 2014.

[107] T. Brixner, T. Mančal, I. V. Stiopkin, and G. R. Fleming, "Phase-stabilized two-dimensional electronic spectroscopy," J. Chem. Phys., vol. 121, no. 9, pp. 4221–4236, 2004.

[108] M. Cowan, J. Ogilvie, and R. Miller, "Two-dimensional spectroscopy using diffractive optics based phased-locked photon echoes," Chem. Phys. Lett., vol. 386, no. 13, pp. 184 – 189, 2004.

[109] E. Harel, A. F. Fidler, and G. S. Engel, "Single-Shot Gradient-Assisted Photon Echo Electronic Spectroscopy," J. Phys. Chem. A, vol. 115, no. 16, pp. 3787–3796, 2011.

[110] Gaël Nardin, Travis M. Autry, Kevin L. Silverman, and S. T. Cundiff, "Multidimensional coherent photocurrent spectroscopy of a semiconductor nanostructure," Opt. Express, vol. 21, pp. 28617–28627, Nov 2013.

[111] A. D. Bristow, D. Karaiskaj, X. Dai, T. Zhang, C. Carlsson, K. R. Hagen, R. Jimenez, and S. T. Cundiff, "A versatile ultrastable platform for optical multidimensional Fourier-transform spectroscopy," Rev. Sci. Instrum., vol. 80, no. 7, p. 073108, 2009.

[112] L. Lepetit, G. Chériaux, and M. Joffre, "Linear techniques of phase measurement by femtosecond spectral interferometry for applications in spectroscopy," J. Opt. Soc. Am. B, vol. 12, pp. 2467–2474, Dec 1995.

[113] G. Moody, M. E. Siemens, A. D. Bristow, X. Dai, A. S. Bracker, D. Gammon, and S. T. Cundiff, "Exciton relaxation and coupling dynamics in a GaAs/$Al_xGa_{1-x}As$ quantum well and quantum dot ensemble," Phys. Rev. B, vol. 83, p. 245316, Jun 2011.

[114] Michael K. Yetzbacher, Trevor L. Courtney, William K. Peters, Katherine A. Kitney, Eric Ryan Smith, and David M. Jonas, "Spectral restoration for femtosecond spectral interferometry with attosecond accuracy," J. Opt. Soc. Am. B, vol. 27, pp. 1104–1117, May 2010.

[115] Alan D. Bristow, Denis Karaiskaj, Xingcan Dai, and Steven T. Cundiff, "All-optical retrieval of the global phase for two-dimensionalFourier-transform spectroscopy," Opt. Express, vol. 16, pp. 18017–18027, Oct 2008.

[116] S. M. Gallagher Faeder and D. M. Jonas, "Two-Dimensional Electronic Correlation and Relaxation Spectra: Theory and Model Calculations," J. Phys. Chem. A, vol. 103, no. 49, pp. 10489–10505, 1999.

[117] A. D. Bristow, D. Karaiskaj, X. Dai, R. P. Mirin, and S. T. Cundiff, "Polarization dependence of semiconductor exciton and biexciton contributions to phase-resolved optical two-dimensional Fourier-transform spectra," Phys. Rev. B, vol. 79, p. 161305, Apr 2009.

[118] G. Moody, R. Singh, H. Li, I. A. Akimov, M. Bayer, D. Reuter, A. D. Wieck, A. S. Bracker, D. Gammon, and S. T. Cundiff, "Influence of confinement on biexciton binding in semiconductor quantum dot ensembles measured with two-dimensional spectroscopy," Phys. Rev. B, vol. 87, p. 041304, Jan 2013.

[119] Kees Lazonder, Maxim S. Pshenichnikov, and Douwe A. Wiersma, "Easy interpretation of optical two-dimensional correlation spectra," Opt. Lett., vol. 31, pp. 3354–3356, Nov 2006.

[120] M. Yoshita, N. Kondo, H. Sakaki, M. Baba, and H. Akiyama, "Large terrace formation and modulated electronic states in (110) GaAs quantum wells," Phys. Rev. B, vol. 63, p. 075305, Jan 2001.

[121] Y. Z. Hu, R. Binder, S. W. Koch, S. T. Cundiff, H. Wang, and D. G. Steel, "Excitation and polarization effects in semiconductor four-wave-mixing spectroscopy," Phys. Rev. B, vol. 49, pp. 14382–14386, May 1994.

[122] J. Lee, E. S. Koteles, and M. O. Vassell, "Luminescence linewidths of excitons in GaAs quantum wells below 150 K," Phys. Rev. B, vol. 33, pp. 5512–5516, Apr 1986.

[123] T. Takagahara, "Localization and homogeneous dephasing relaxation of quasi-two-dimensional excitons in quantum-well heterostructures," Phys. Rev. B, vol. 32, pp. 7013–7015, Nov 1985.

[124] L. Schultheis, A. Honold, J. Kuhl, K. Köhler, and C. W. Tu, "Optical dephasing of homogeneously broadened two-dimensional exciton transitions in GaAs quantum wells," Phys. Rev. B, vol. 34, pp. 9027–9030, Dec 1986.

[125] T. Ruf, J. Spitzer, V. F. Sapega, V. I. Belitsky, M. Cardona, and K. Ploog, "Interface roughness and homogeneous linewidths in quantum wells and superlattices studied by resonant acoustic-phonon Raman scattering," Phys. Rev. B, vol. 50, pp. 1792–1806, Jul 1994.

[126] D. Gammon, S. Rudin, T. L. Reinecke, D. S. Katzer, and C. S. Kyono, "Phonon broadening of excitons in GaAs/al$_x$ga$_{1-x}$As quantum wells," Phys. Rev. B, vol. 51, pp. 16785–16789, Jun 1995.

[127] D. Birkedal, V. G. Lyssenko, J. M. Hvam, and K. El Sayed, "Continuum contribution to excitonic four-wave mixing due to interaction-induced nonlinearities," Phys. Rev. B, vol. 54, pp. R14250–R14253, Nov 1996.

[128] K. Kwak, S. Park, I. J. Finkelstein, and M. D. Fayer, "Frequency-frequency correlation functions and apodization in two-dimensional infrared vibrational echo spectroscopy: A new approach," J. Chem. Phys., vol. 127, no. 12, p. 124503, 2007.

[129] P. R. Berman and R. G. Brewer, "Modified optical Bloch equations for solids," Phys. Rev. A, vol. 32, pp. 2784–2796, Nov 1985.

[130] H. Wang and D. G. Steel, "Effects of spectral diffusion on frequency-domain four-wave-mixing spectroscopy," Phys. Rev. A, vol. 43, pp. 3823–3831, Apr 1991.

[131] M. Z. Maialle, E. A. de Andrada e Silva, and L. J. Sham, "Exciton spin dynamics in quantum wells," Phys. Rev. B, vol. 47, pp. 15776–15788, Jun 1993.

[132] D. Bennhardt, P. Thomas, R. Eccleston, E. J. Mayer, and J. Kuhl, "Polarization dependence of four-wave-mixing signals in quantum wells," Phys. Rev. B, vol. 47, pp. 13485–13490, May 1993.

[133] W. Langbein and J. Hvam, "Biexcitonic Bound and Continuum States of Homogeneously and Inhomogeneously Broadened Exciton Resonances," Phys. Status Solidi A, vol. 190, no. 1, pp. 167–174, 2002.

[134] Y. P. Svirko, M. Shirane, H. Suzuura, and M. Kuwata Gonokami, "Four-Wave Mixing Theory at the Excitonic Resonance: Weakly Interacting Boson Model," J. Phys. Soc. Jpn., vol. 68, no. 2, pp. 674–682, 1999.

[135] S. Rudin and T. Reinecke, "Anharmonic oscillator model for driven and vacuum-field Rabi oscillations," Phys. Rev. B, vol. 63, p. 075308, Jan 2001.

[136] S. Mukamel, "Multidimensional Femtosecond Correlation Spectroscopies of Electronic and Vibrational Excitations," Annu. Rev. Phys. Chem, vol. 51, no. 1, pp. 691–729, 2000.

[137] E. Mayer, G. Smith, V. Heuckeroth, J. Kuhl, K. Bott, A. Schulze, T. Meier, D. Bennhardt, S. Koch, P. Thomas, R. Hey, and K. Ploog, "Evidence of biexcitonic contributions to four-wave mixing in GaAs quantum wells," Phys. Rev. B, vol. 50, pp. 14730–14733, Nov 1994.

[138] T. F. Albrecht, K. Bott, T. Meier, A. Schulze, M. Koch, S. T. Cundiff, J. Feldmann, W. Stolz, P. Thomas, S. W. Koch, and E. O. Göbel, "Disorder mediated biexcitonic beats in semiconductor quantum wells," Phys. Rev. B, vol. 54, pp. 4436–4439, Aug 1996.

[139] J.-i. Inoue, T. Brandes, and A. Shimizu, "Renormalized bosonic interaction of excitons," Phys. Rev. B, vol. 61, pp. 2863–2873, Jan 2000.

[140] B. L. Wilmer, F. Passmann, M. Gehl, G. Khitrova, and A. D. Bristow, "Multidimensional coherent spectroscopy of a semiconductor microcavity," Phys. Rev. B, vol. 91, p. 201304, May 2015.

[141] S. Palomba and L. Novotny, "Nonlinear Excitation of Surface Plasmon Polaritons by Four-Wave Mixing," Phys. Rev. Lett., vol. 101, p. 056802, Aug 2008.

[142] R. W. Boyd, Nonlinear optics. Academic press, San Diego, 2003.

[143] J. M. Shacklette and S. T. Cundiff, "Nonperturbative transient four-wave-mixing line shapes due to excitation-induced shift and excitation-induced dephasing," J. Opt. Soc. Am. B, vol. 20, pp. 764–769, Apr 2003.

[144] S. Priyadarshi, A. M. Racu, K. Pierz, U. Siegner, M. Bieler, H. T. Duc, J. Förstner, and T. Meier, "Reversal of Coherently Controlled Ultrafast Photocurrents by Band Mixing in Undoped GaAs Quantum Wells," Phys. Rev. Lett., vol. 104, p. 217401, May 2010.

Appendix A

Optical Bloch equations

In the discussion of FWM theory in Section 3.1.2, we had directly written down the OBEs for a two-level system in the rotating wave approximation. Here, we will derive the OBEs for a two-level system starting from the light-matter interaction in the dipole approximation. A similar procedure can be followed to obtain the OBEs for a more complicated system. The derivation presented here is based on the discussion by Boyd [142]. We will derive these equations for the two-level system shown in Fig. 3.2(a).

The total Hamiltonian of the system can be written as

$$H = H_0 + H_{int} \tag{A.1}$$

where H_0 is the unperturbed Hamiltonian and H_{int} is the light-matter interaction. For a two-level system, these Hamiltonians can be represented by 2x2 matrices:

$$H_0 = \begin{pmatrix} 0 & 0 \\ 0 & \hbar\omega_{01} \end{pmatrix} \qquad H_{int} = \begin{pmatrix} 0 & -\mu_{01}\mathscr{E} \\ -\mu_{01}\mathscr{E} & 0 \end{pmatrix} \tag{A.2}$$

where H_{int} is written in the dipole approximation for light-matter interaction and $\mathscr{E}$ is the electric field of light given by

$$\mathscr{E} = \frac{1}{2}|E|\left(\mathrm{e}^{i(\mathbf{k}\cdot\mathbf{r}-\omega t)} + \mathrm{e}^{-i(\mathbf{k}\cdot\mathbf{r}-\omega t)}\right) \tag{A.3}$$

where $|E|$, $\mathbf{k}$, and ω are the amplitude, wavevector, and frequency of the optical electric field, respectively, and $\mathbf{r}$ is a position vector.

The time-evolution of the density matrix is given by

$$\dot{\rho} = -\frac{i}{\hbar}\left[H, \rho\right] \tag{A.4}$$

where ρ is the density matrix for the two-level system and the square brackets indicate the commutator operation. Equation (A.4) can be written explicitly in the matrix form

$$\begin{pmatrix} \dot{\rho}_{00} & \dot{\rho}_{01} \\ \dot{\rho}_{10} & \dot{\rho}_{11} \end{pmatrix} = -\frac{i}{\hbar}\left[\begin{pmatrix} 0 & \mu_{01}\mathscr{E} \\ \mu_{01}\mathscr{E} & \hbar\omega_{01} \end{pmatrix}\begin{pmatrix} \rho_{00} & \rho_{01} \\ \rho_{10} & \rho_{11} \end{pmatrix} - \begin{pmatrix} \rho_{00} & \rho_{01} \\ \rho_{10} & \rho_{11} \end{pmatrix}\begin{pmatrix} 0 & \mu_{01}\mathscr{E} \\ \mu_{01}\mathscr{E} & \hbar\omega_{01} \end{pmatrix}\right]. \tag{A.5}$$

Equation (A.5) yields the following set of equations:

$$\begin{aligned} \dot{\rho}_{00} &= -\frac{i}{\hbar}\mu_{01}\mathscr{E}(\rho_{10} - \rho_{01}) \\ \dot{\rho}_{01} &= -\frac{i}{\hbar}[\mu_{01}\mathscr{E}(\rho_{11} - \rho_{00}) - \hbar\omega_{01}\rho_{01}] \\ \dot{\rho}_{10} &= -\frac{i}{\hbar}[\mu_{01}\mathscr{E}(\rho_{00} - \rho_{11}) + \hbar\omega_{01}\rho_{10}] \\ \dot{\rho}_{11} &= -\frac{i}{\hbar}\mu_{01}\mathscr{E}(\rho_{01} - \rho_{10}) \end{aligned} \tag{A.6}$$

It is apparent from Eqs. (A.6) that $\dot{\rho}_{01}$ and $\dot{\rho}_{10}$ are complex conjugates of each other. Also, $\dot{\rho}_{00} = -\dot{\rho}_{11}$, which follows from $\rho_{00} + \rho_{11} = 1$. Thus, we can completely describe the time-evolution of the system through the time-evolution of ρ_{01} and ρ_{11}. It should be noted that we have not included any decay terms in Eqs. (A.6). The relevant equations with the decay terms can be written as

$$\begin{aligned} \dot{\rho}_{01} &= (-\gamma_{01} + i\omega_{01})\rho_{01} - \frac{i}{\hbar}\mu_{01}\mathscr{E}(2\rho_{11} - 1) \\ \dot{\rho}_{11} &= -\Gamma_1\rho_{11} - \frac{i}{\hbar}\mu_{01}\mathscr{E}(\rho_{01} - \rho_{10}). \end{aligned} \tag{A.7}$$

Rotating-wave approximation: Equations (A.7) are sufficient to describe the time-evolution of density matrix elements. However, it is often convenient to go to the rotating-wave approximation, in which the fast oscillating coherence term is described by the product of a slowly varying term with an oscillatory term.

$$\rho_{01} = \widetilde{\rho}_{01}\mathrm{e}^{i\omega_{01}t} \qquad\qquad \rho_{10} = \widetilde{\rho}_{10}\mathrm{e}^{-i\omega_{10}t} \tag{A.8}$$

where $\widetilde{\rho}_{01}$ and $\widetilde{\rho}_{10}$ are the slowly-varying terms. Also, we can redefine the optical electric field $\mathscr{E}$ in a more useful form as

$$\mathscr{E} = \frac{1}{2}(\mathcal{E}\mathrm{e}^{-i\omega t} + \mathcal{E}^{*}\mathrm{e}^{i\omega t}) \tag{A.9}$$

where $\mathcal{E} = |E|\mathrm{e}^{i\mathbf{k}\cdot\mathbf{r}}$.

By substituting Eqs. (A.8) and (A.9) in Eqs. (A.7) and ignoring terms that oscillate with frequency 2ω, we obtain

$$\begin{aligned} \dot{\widetilde{\rho}}_{01} &= (-\gamma_{01} + i\Delta_{01})\widetilde{\rho}_{01} - \frac{i}{2\hbar}\mu_{01}\mathrm{E}^{*}(2\rho_{11} - 1) \\ \dot{\rho}_{11} &= -\Gamma_{1}\rho_{11} - \frac{i}{\hbar}\mu_{01}(\mathcal{E}\widetilde{\rho}_{01} - \mathcal{E}^{*}\widetilde{\rho}_{10}). \end{aligned} \tag{A.10}$$

Equations (A.10) are the same as Eq. (3.6) in Section 3.1.2.

Appendix B

Numerical simulations

Many-body effects, such as EIS, EID, and local field effects can be added phenomenologically to the OBEs. The perturbative solution does not work for these modified OBEs, which need to be solved numerically [143]. The signature of the many-body effects, such as EIS and EID, on 2D spectrum have been observed previously, although without considering inhomogeneous broadening [13]. However, the impact of local field effects on 2DCS experiments have not been studied. In order to explore this phenomenon, we have developed a numerical method to solve the OBEs, which will be discussed next.

We will only consider a two-level system, although the procedure is general and can be extended to more complicated systems easily. We start by ignoring the many-body effects, to keep things simple. The OBEs for such a system was derived in Appendix A, and is given by Eq. (A.7). For a given time-dependent electric field, these coupled differential equations can be easily solved on a computer. The time-dependent electric field can be modified depending on the time delays. For a rephasing one-quantum spectrum, we change the delay τ and solve the OBEs for each value of τ. This procedure evaluates the total coherence, up to **all** orders, including the linear response and all possible TFWM signals. In order to isolate a particular TFWM signal we need to implement a signal-selection procedure that is analogous to the experimental phase-matching condition.

B.1 Phase-matching

The basic idea for phase-matching in the simulation is basically the same as that in a non-collinear experiment. We tag the individual pulses by distinct "wavevectors". The OBEs are solved for a series of "spatial" positions. We take a Fourier transform of the signal along this spatial dimension and isolate the signal in the "k-space". We consider only a single spatial axis to reduce the computational complexity. We define the electric field due to a single pulse as

$$\mathscr{E}_j(t') = \frac{1}{2}|E|\, \mathrm{e}^{-\frac{(t'-t_j)^2}{2t_p{}^2}} \left[\mathrm{e}^{-i\{\omega(t'-t_j)-k_j z\}} + \mathrm{e}^{i\{\omega(t'-t_j)-k_j z\}}\right] \tag{B.1}$$

where t_j is the time of incidence of pulse j with wavevector k_j, t_p is the pulse duration, ω is the center frequency of the light field, and z is the spatial dimension. We denote time by t' to distinguish it from the time delay t in a 2DCS experiment. The total electric field is the sum of the electric fields from all the incident pulses. The oscillating part of the electric field in Eq. (B.1) slows down the computational process significantly. Thus, we set $\omega = 0$; the transition energy is defined as the detuning from ω. This simplification is equivalent to the rotating-wave approximation discussed in Appendix A.

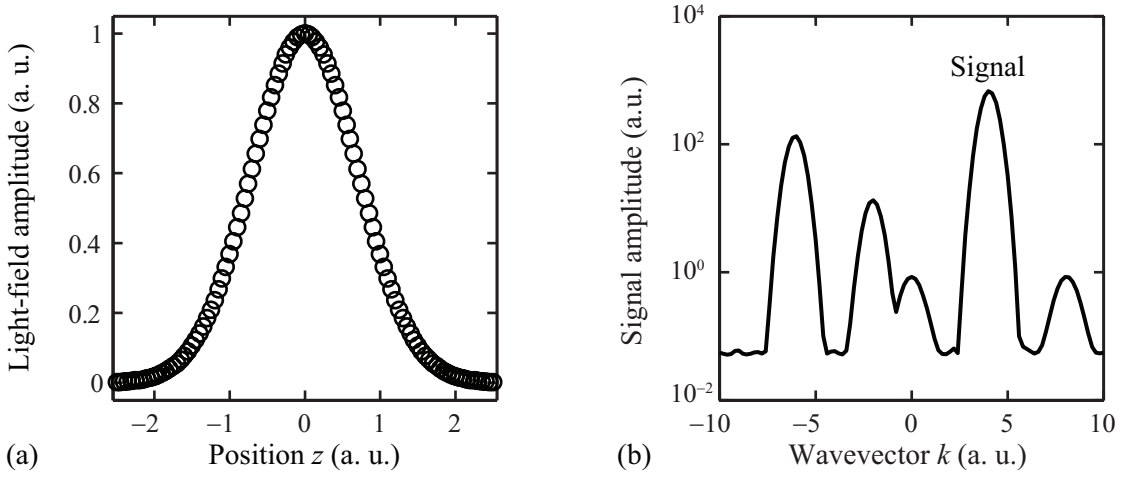

Figure B.1: (a) The longitudinal "spatial" amplitude profile of the incident electric field. (b) The transient four-wave mixing signal amplitude as a function of the wavevector.

The spatial positions considered in the simulation are shown in Fig. B.1(a); we use 101 spatial points. We have used a Gaussian spatial profile so that the electric field amplitude peaks at $z = 0$ and decays smoothly to zero. Using such an amplitude profile ensures that the Fourier transform is well-behaved. The OBEs are solved as a function of two time delays τ and t for each of these spatial points to obtain the radiated signal $S(\tau, t, z)$ from the macroscopic polarization, which in turn is related to the coherence ρ_{01} as indicated in Eq. (2.14). This procedure is repeated four times with different phases of the incident pulses to implement a phase-cycling routine similar to the one described in Section 3.3.2. The individual spectra are processed to obtain the third-order polarization $S^{(3)}(\tau, t, z)$. We take a Fourier transform of this signal along the position axis to obtain $\mathcal{S}^{(3)}(\tau, t, k)$. An example of the integrated third-order signal is shown in Fig. B.1(b) as a function of wavevector k. There are several peaks in this plot. Each peak corresponds to a different phase-matching direction. We use $k_A = -4$, $k_B = 1$, and $k_C = -1$, which gives $k_S = 4$ when pulse A is conjugated, as labeled in the plot. We select the region $k = 4 \pm 1$ in $\mathcal{S}^{(3)}(\tau, t, k)$ and set the signal at all other k values to zero. This signal is Fourier transformed back to the spatial domain to obtain $S_{cut}(\tau, t, z)$. Finally, we obtain the TFWM signal $S_{S_I}(\tau, t) = S_{cut}(\tau, t, 0)$. The corresponding 2D spectrum is obtained by taking a two-dimensional Fourier transform of $S_{S_I}(\tau, t)$.

B.2 Inhomogeneous broadening

The procedure mentioned in the previous section is for a single oscillator. In case of inhomogeneous broadening, the same procedure has to be repeated for oscillators with different resonance energies as indicated in Fig. B.2 and different amplitudes α_i indicating different number of oscillators at each frequency position. The amplitude terms α_i are normalized such that the sum $\Sigma\, \alpha_i = 1$. This normalization ensures that, for a given inhomogeneous linewidth, the total signal is independent of the number of oscillators chosen in the simulations. The total signal for the inhomogeneous distribution is obtained by taking the sum

of the signal from all the frequency components after weighting the signal from a particular frequency component i by the amplitude α_i.

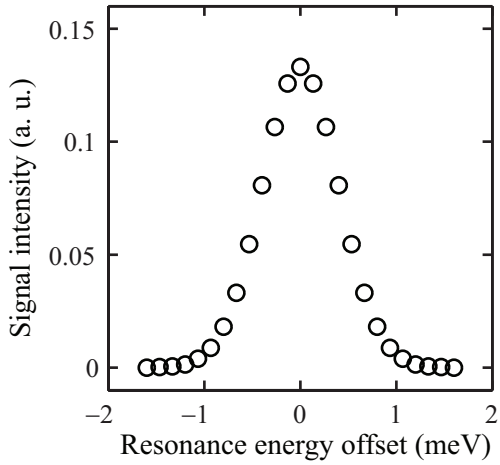

Figure B.2: The inhomogeneous distribution used for the simulations.

The 2D spectra obtained for the inhomogeneous broadening indicated in Fig. B.2 are shown in Fig. B.3. As expected the peak is elongated along the diagonal line. The signal phase is similar to that obtained for the homogeneous case through the analytical procedure, as shown in Fig. 3.3.

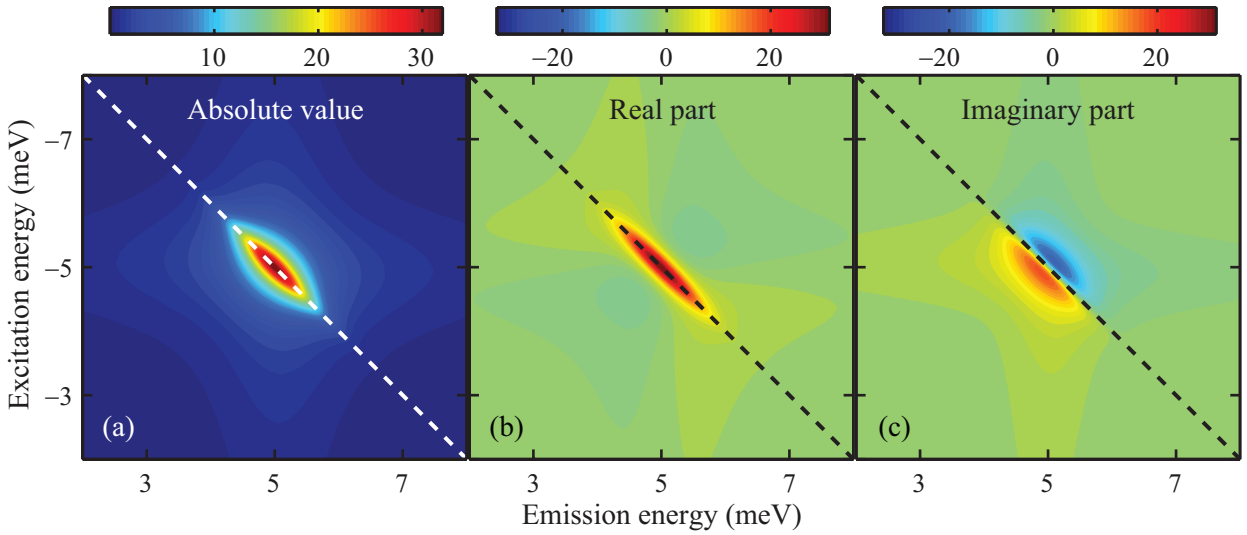

Figure B.3: The (a) absolute value, (b) real part, and (c) imaginary part of the rephasing one-quantum 2D spectrum for a two-level system.

B.3 Phenomenological many-body effects

The motivation for developing the numerical procedure to solve the OBEs was to include the phenomenological many-body effects, which we will discuss next. The transition energy, dephasing rate and the effective electric field are modified by these interaction terms terms [143].

$$\begin{aligned} \gamma_{01} &= \gamma_0 + N\gamma'\rho_{11} \\ \omega_{01} &= \omega_0 + N\omega'\rho_{11} \\ \mathscr{E} &= \mathscr{E}_0 + \mathscr{L}P \end{aligned} \tag{B.2}$$

where γ_0 and ω_0 are the dephasing rate and resonance frequency, respectively, for an unexcited sample, N is the total number of oscillators, γ' and ω' are the EID and EIS parameters, respectively, $\mathscr{E}_0$ is the electric field of the incident light, $\mathscr{L}$ is the local-field parameter, and P is the macroscopic polarization given by Eq. (2.14). In case of inhomogeneous broadening, the local-field term is, generally, neglected because the macroscopic polarization decays quickly.

The modified OBEs are solved according to the procedure mentioned above to calculate the TFWM signal. An example of such a situation is shown in Fig. B.4 where we have only included the EIS term, i.e. $\gamma' = \mathscr{L} = 0$. We obtain a dispersive peak in the real part spectrum shown in Fig. B.4(b). This feature is similar to the experimentally measured signal phase [13].

Including the many-body terms in the absence of inhomogeneous broadening is straightforward. In the presence of inhomogeneous broadening, however, there are several ways to include the many-body terms. The complication arises because separate density matrices are defined for each frequency element. By testing the different methods, we concluded that EID and EIS are correctly incorporated as

$$\begin{aligned} \gamma_{01,i} &= \gamma_0 + A_i N\gamma'\rho_{11,i} \\ \omega_{01,i} &= \omega_0 + A_i N\omega'\rho_{11,i} \end{aligned} \tag{B.3}$$

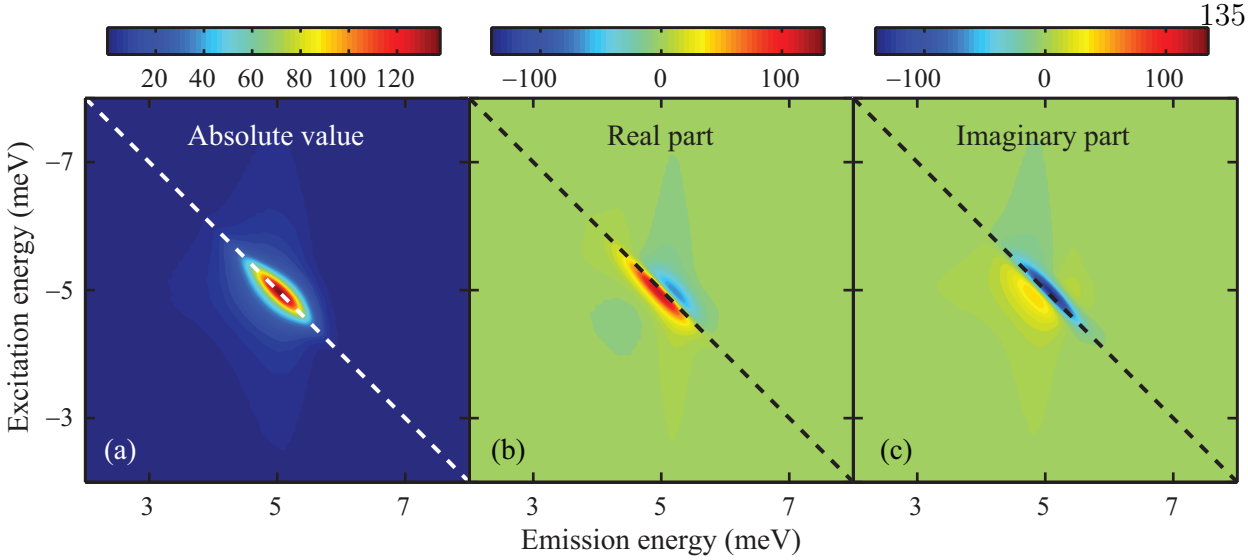

Figure B.4: The (a) absolute value, (b) real part, and (c) imaginary part of the rephasing one-quantum 2D spectrum for an inhomogenoeusly-broadened two-level system. Phenomenological excitation-induced shift is included. Notice the increase in amplitude compared to the spectra in Fig. B.3 and the dispersive peak in (b).

where index i is used to indicate a frequency element. Consequently, the effect of the many-body terms is different for the different frequency groups. If we extend this treatment to the local-field effect, the effective electric field experienced by each frequency group is different, and is given by

$$\mathscr{E}_i = \mathscr{E}_0 + \mathscr{L} P_i \ . \tag{B.4}$$

This treatment of the local-field implies that it cannot be ignored even for inhomogeneously broadened systems. We are still working on correctly including the local-field correction and, thus, do not show any results for the same.

Appendix C

Nominally Disallowed Transitions in (110)-oriented GaAs Quantum Well

We have mentioned a few effects of the reduced symmetry of the (110)-oriented GaAs QWs in Section 2.6. Also, we discussed the resulting anisotropic exciton-dephasing rates in Chapter 4. Another consequence of the reduced symmetry is the mixing of the HH and LH valence bands, which results in the HH band having some LH characteristics, and vice-versa. As a result, the polarization selection rules discussed in Section 2.2.3, are not strictly valid. The effect of this band mixing on photocurrents generated in these QWs has been studied both experimentally [144] and theoretically [45]. We find that another consequence of this band mixing is that an excitonic transition that should be disallowed, is optically active.

Figure C.1 shows a 2D spectrum spanning both the HH and LH exciton resonances; the excitation-laser spectrum (blue) and the absorption spectrum (red) are shown in the top panel. This spectrum was obtained with the sample at a temperature of 10 K and the collinear polarization scheme with Y polarization. The spectrum comprises five distinct peaks, which are labeled A – E. The HH and LH peaks, which are labeled A and B, respectively, appear on the diagonal line. The peaks labeled C and D indicate coupling between the HH and LH excitons. Similar to the cross peaks in the simulated spectrum shown in Fig. 3.7, these peaks are titled with respect to the diagonal line due to different inhomogeneous linewidths of the HH and LH exciton resonances. The origin of these coupling peaks is similar to those observed in the (001)-oriented GaAs QWs [99]. The presence of the peak labeled E, however, is unexpected; a similar peak does not show up for the (001)-oriented

GaAs QW.

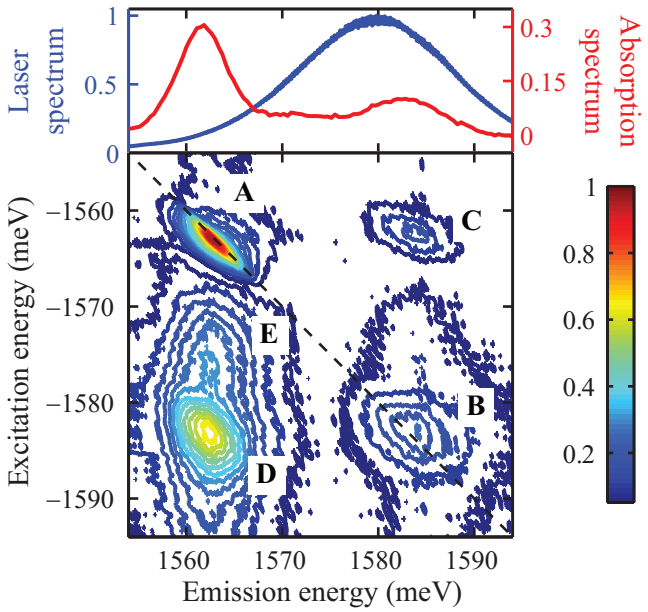

Figure C.1: Rephasing one-quantum spectrum spanning both the heavy and light hole excitons in (110)-oriented quantum well is shown in the bottom panel. Sample temperature was 10 K and co-linear polarization scheme with Y polarized pulses was used. The heavy hole and light hole exciton peaks on the diagonal are labeled A and C, respectively. The coupling peaks between these exciton states are labeled C and D. Note the tilt of these peaks similar to those shown in Fig. 3.7. Another peak E appears which should be nominally disallowed. The top panel shows the laser spectrum in blue and the absorption spectrum in red.

We hypothesize that the presence of this peak indicates the presence of excitons formed with the second HH band and the first electron state. This exciton transition should not be allowed through the dipole selection rules, but results from the HH and LH band-mixing. A diagonal peak due to this exciton resonance should be present, but is too weak due to the small dipole moment of this transition. The resonance energy of this peak is in qualitative agreement with numerical calculations [45]. Although this exciton resonance is weak, it can have significant effect on the optically generated currents in these samples. A more detailed study into the origin and effects of this resonance is needed, which is beyond the scope of the current work.

Appendix D

Population Evolution

In Section 5.3.2, we presented interesting evolution of signal strength as a function of the waiting time T, as shown in Fig. 5.9. The amplitude term in Eq. (5.3) gives the TFWM signal strength. We measured this amplitude term through the fitting procedure discussed in Section 5.3.1. To ensure that the signal evolution is not an artifact of the fitting procedure or an incorrect model, we performed rephasing zero-quantum scan to directly measure the evolution of signal strength with the waiting time. These experiments were performed for several sample temperatures. The time-integrated TFWM signal as a function of the waiting

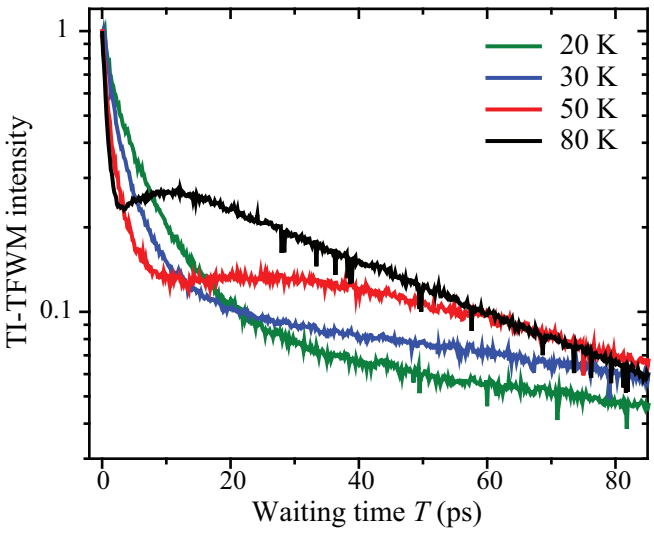

Figure D.1: Evolution of time-integrated transient four wave mixing signal with the waiting time for different sample temperatures. Note the similarities between these plots and those shown in Fig. 5.9.

time are shown in Fig. D.1 for several sample temperatures. Although 2DCS experiments were performed, we plot the time-integrated signal intensity to compare with the plots shown in Fig. 5.9. The measurements were taken for much longer values of delay T. We only show a section of it to highlight the behavior for short waiting times.

The similarity between the plots in Figs. 5.9 and D.1 is apparent; the non-exponential evolution along with the non-monotonic signal evolution for temperatures > 50 K are seen in both figures. We estimate an exciton population decay time in the range of $\sim 100 - 300$ ps over the temperature range studied. This population decay time is measured from the slow, exponential decay of the signal for $T > 50$ ps.

While these results confirm the results obtained from the spectral diffusion experiment, they do not shed any light on the possible reason for the non-monotonic behavior for high sample temperatures.